2011-11-28

Influence of Supraglottal Geometry and Modeling Choices on the Flow-Induced Vibration of a Computational Vocal Fold Model

Timothy E. Shurtz
Brigham Young University - Provo

Influence of Supraglottal Geometry and Modeling Choices on the

Flow-Induced Vibration of a Computational

Vocal Fold Model

Timothy E. Shurtz

A thesis submitted to the faculty of
Brigham Young University
in partial fulfillment of the requirements for the degree of

Master of Science

Scott L. Thomson, Chair
Daniel Maynes
Steven E. Gorrell

Department of Mechanical Engineering

Brigham Young University

December 2011

ABSTRACT

Influence of Supraglottal Geometry and Modeling Choices on the
Flow-Induced Vibration of a Computational
Vocal Fold Model

Timothy E Shurtz
Department of Mechanical Engineering, BYU
Master of Science

Computational models of the flow-induced vibrations of the vocal folds are powerful tools that can be used in conjunction with physical experiments to better understand voice production. This thesis research has been performed to contribute to the understanding of vocal fold dynamics as well as several aspects of computational modeling of the vocal folds. In particular, the effects of supraglottal geometry have been analyzed using a computational model of the vocal folds and laryngeal airway. In addition, three important computational modeling parameters (contact line location, Poisson's ratio, and symmetry assumptions) have been systematically varied to determine their influence on model output. Variations in model response were quantified by comparing glottal width, frequency, flow rate, open quotient, pressures, and wave velocity measures. In addition, the glottal jet was qualitatively analyzed. It was found that for various supraglottal geometries (either symmetrically or asymmetrically positioned), there was little asymmetry of the vocal fold motion despite significant asymmetry in the glottal jet. In addition, the vocal fold motion was most symmetric when consistent jet deflection was present (even if asymmetric). Inconsistent deflection of the glottal jet led to slightly larger asymmetries in vocal fold motion. The contact line location was found to have minimal impact on glottal width, frequency, and flow rate. The largest influence of the contact line location was seen in predicted velocity fields during the closed phase and in the pressure profiles along the vocal fold surfaces. Variations in Poisson's ratio strongly affected vocal fold motion, with lower Poisson's ratios resulting in larger amplitudes. The model did not vibrate when a Poisson's ratio of 0.49999 was used. The response of a full model (with two vocal folds) was shown to vary slightly from that of a half model (one vocal fold and a symmetry boundary condition), the greatest difference being in the deflection and dissipation of the glottal jet. It was concluded that for many scenarios the half model will be sufficient for modeling vocal fold motion; however, a full model is suggested for studies of material asymmetry or glottal jet dynamics. Application of these results to computational models of the vocal folds will lead to improved modeling and understanding of vocal fold dynamics.

Keywords: vocal folds, computational fluid dynamics, flow-induced vibrations, supraglottal geometry, contact line, Poisson's ratio, symmetry, Timothy E. Shurtz

ACKNOWLEDGMENTS

I would first of all like to thank my Heavenly Father for his blessings, direction, and support. He has guided me in choosing to get a master's degree in mechanical engineering at Brigham Young University. He has also blessed me with the intellect needed to succeed in obtaining that degree, and supported me throughout the process.

Next, I would like to thank my wife Alora and dedicate this work to her. Her love and support through the past three years have made my education and thesis writing/defense process endurable and given it purpose. She has been a great blessing in my life, and I love her dearly.

Additionally, I would like to thank my advisor, Dr. Scott Thomson for all of his help and sacrifice. Without his guidance and many editorial remarks, this work would never have been of sufficient quality to defend. Additionally his willingness to make a trip back to BYU campus from his sabbatical in Germany made my defense possible. It was well above and beyond the call of duty. I thank him and his family for the related sacrifice.

I would also like to thank the other members of my thesis committee, Dr. Maynes and Dr. Gorrell and members of the voice research group at BYU, whose suggestions helped to advance quality of my thesis and research in general.

Finally, I would like to thank the National Institute on Deafness and Other Communication Disorders for funding, and the Department of Mechanical Engineering at Brigham Young University for the facilities and resources that made my research possible.

TABLE OF CONTENTS

LIST OF TABLES

x

LIST OF FIGURES

1 INTRODUCTION

1.1 Background

1.1.1 Motivation

Most people depend on their voice for daily communication, and many rely on it for their careers (e.g., singers, sports announcers, educators, and radio personalities). In addition, many individuals suffer from poor voice quality due to voice pathologies. According to the National Institute on Deafness and Other Communication Disorders, "approximately 7.5 million people in the United States have trouble using their voices" (NIDCD, 2010). One of the goals of voice research is to better understand the complex mechanisms of speech production. Even with a large body of research already performed, there are still many aspects of voice production that are not fully understood. An improved understanding of the physics of voice production will lead to better diagnosis and treatment of patients with voice pathologies.

There are several methods for performing voice research, and there are also many complex issues that must be considered when choosing a suitable approach. In vivo experiments are difficult to perform, can affect speech production during the experiment, and are very restricted in their scope. Excised larynx experiments are difficult to perform, have limited potential for parameterization, and must be used in experiments with conditioned air to prevent the tissue from degradation. Even with treated air, the tissue in excised larynges rapidly degrades. Synthetic vocal fold models can be used to avoid some of the above difficulties;

however, they often do not precisely reproduce vocal fold material properties, geometries, or motion. In addition, it is often difficult in experiments to characterize details of vocal fold motion, airway pressures, and fluid velocities within the glottis (the space between the vocal folds). Computational modeling of the vocal folds has been used to simulate vocal fold motion and to obtain details of the fluid-structure interaction. By using computational models as a complementary tool, some of the above limitations are overcome. In this thesis, research aimed towards exploring several aspects of these computational models is presented.

1.1.2 Voice Production and Anatomy

Sound for most voiced speech initiates within the larynx (often referred to as the voice box). The larynx is located in the front central portion of the neck (see Fig. 1.1). Within the larynx, a pair of vocal folds is oriented primarily along an axis from the posterior (rear) to the anterior (front) of the body. These folds are comprised of a muscle layer, a ligament, layers of soft tissue (lamina propria) which become progressively more flexible towards the vocal fold surface, and finally, a thin epithelial layer with higher Young's modulus. During phonation (vocal fold vibration for voice production), the vocal folds are adducted towards the medial plane of the body. Air is forced from the lungs, through the trachea, over the vocal folds, and out of the mouth and/or nose. A complex coupling of the vocal fold tissue dynamics with the respiratory aerodynamics leads to vibrations of the vocal folds. This vibration causes the vocal folds to open and close repeatedly, which leads to pulsatile pressure fluctuations in the supraglottal region (airway directly above the glottis). This fluctuating pressure is the primary source of sound in voice production. The glottal tone is modified as it passes through the vocal tract to produce various sounds.
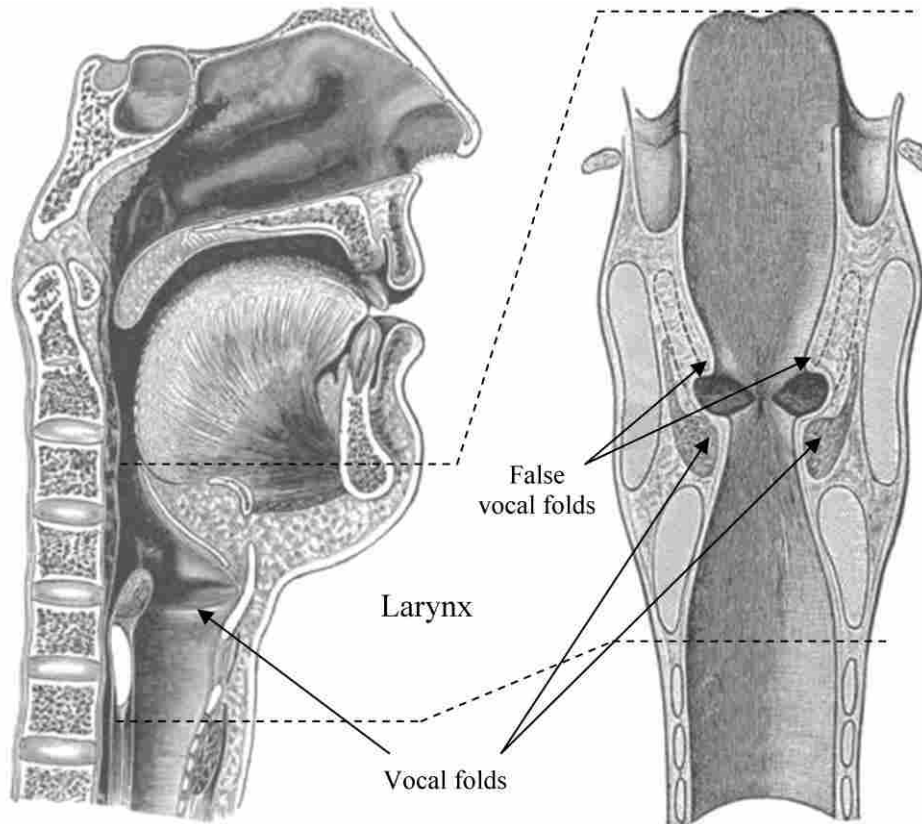
Figure 1.1: Sagittal (left) and coronal (right) views of the larynx (adapted from *Gray's Anatomy of the Human Larynx*, images public domain, www.bartleby.com).

The false vocal folds (see Fig. 1.1) are located above, and are somewhat similar in shape to, the true vocal folds; however, they do not typically adduct or vibrate during normal voice production. Thus, for most cases, their effect on phonation is thought to be passive rather than active.

1.2   Computational Modeling

Computational vocal fold modeling has the advantage of ease of parameterization and availability of data (e.g., pressure and velocity fields) throughout the simulated domain. Researchers have used a wide variety of computational models of voice production that vary in

complexity, scope, and accuracy. All generally are centered on a mathematical coupling between a model of the vocal folds and some form of airflow simulation. One of the earliest simulations used a simple two mass vocal fold model coupled with a Bernoulli flow solver (e.g., Ishizaka and Flanagan, 1972). This model concept was expanded upon to include more tissue and solid characteristics (e.g., Titze, 1973, 1974; Story and Titze, 1995). Later, continuum models of the vocal folds were developed which could more accurately represent tissue shape and material properties (e.g., Alipour et al., 2000). Models which incorporate more advanced computational fluid dynamics (CFD) approaches have been used (e.g., Alipour and Scherer, 2004; Thomson et al., 2005). These have usually been based on finite volume or finite element methods, although recently, models using the immersed boundary method have been developed (e.g., Zheng et al., 2010). These CFD solvers provide reasonably accurate predictions of the airflow and can include aspects of fluid dynamics which are not accounted for in more simplistic fluid models.

1.3   Focus of Research

As mentioned above, the focus of this research is on computational modeling of the vocal folds. The work is concentrated on the effects of (1) supraglottal airway geometry and (2) various modeling choices on laryngeal airflow and vocal fold flow-induced vibration. These are introduced below, along with a brief overview of relevant research. More in-depth literature reviews for each topic are given in each respective chapter.

1.3.1   Supraglottal Geometry

The motion of the vocal folds is coupled to the aerodynamics of laryngeal flow. Therefore, variations in the supraglottal geometry have the potential to alter vocal fold motion. Many researchers have used computational self-oscillating vocal fold models to study various

aspects of voice production (e.g., Tao et al., 2007; Luo et al., 2009; Zheng et al., 2010). Several of these studies have focused on asymmetry of supraglottal flow and vocal fold motion, as well as the effects of including false vocal folds (e.g., Zheng et al., 2009; Zheng et al., 2011a). Drechsel and Thomson (2008) used particle image velocimetry (PIV) and synthetic self-oscillating vocal folds with various supraglottal geometries to study the effect of supraglottal airway configuration on jet characteristics. Most of these model vibration patterns lacked a significant "mucosal wave," a key feature of human vocal fold vibration. In addition, the physical model could not ensure perfect symmetry of the vocal fold properties or geometry. In Chapter 2 a computational model with symmetric vocal folds, a mucosal wave, and various supraglottal geometric configurations is explored.

1.3.2   Computational Modeling Choices

Prior computational vocal fold models have incorporated a variety of modeling assumptions and choices. Three in particular – contact line location, Poisson's ratio, and symmetry – were studied in this research, as summarized below and discussed in detail in Chapter 3.

First, during normal phonation, the vocal folds usually collide. However, in a CFD approach the mesh cells or elements between the vocal folds must maintain non-zero volume. In order to prevent complete collapse of the mesh, researchers have often implemented a contact line or plane which prevents the glottis from closing completely (e.g., Luo et al., 2008; Pickup and Thomson, 2011). While this contact line is often used, quantification of its effects on model response has yet to be evaluated.

Second, computational vocal fold models can include various material models. In particular, a range of Poisson's ratios has been used. Vocal fold tissue is often considered to be

incompressible, which would suggest that a Poisson's ratio of 0.5 should be used (at least in an isotropic material); however, very few models have incorporated a Poisson's ratio corresponding to an incompressible material. Furthermore, it has been observed that the vibration amplitude of vocal fold models is significantly diminished as the Poisson's ratio approaches 0.5. The precise effects of Poisson's ratio on model response have not been systematically studied.

In order to reduce computational costs, several previous two-dimensional vocal fold simulations have directly modeled only half of the larynx (i.e., one vocal fold) by imposing a symmetry boundary condition (e.g., Thomson et al., 2005; Zhang, 2009). However, physical and computational models have shown significant asymmetry in the glottal jet (e.g., Triep et al., 2005; Drechsel and Thomson, 2008; Zheng et al., 2010). Researchers who have studied this asymmetry using computational models have quantified the asymmetry in the jet and vocal fold motion using a full 2D larynx; however, the differences between a full model and a half model have yet to be quantified.

1.4   Thesis Outline

The thesis is divided into two main chapters. In Chapter 2, the effect of supraglottal geometry on the flow-induced response of a computational vocal fold model is discussed. In Chapter 3, the effect of modeling choices on the flow-induced response of a computational vocal fold model is considered.

1.4.1   Effect of Supraglottal Geometry on the Flow-Induced Response of a Computational Vocal Fold Model (Chapter 2)

Two supraglottal geometry types, one with false vocal folds and one without, were used to study the effect of supraglottal geometry on the flow-induced vibration of a two-dimensional,

self-oscillating vocal fold model. The supraglottal geometries were positioned both symmetrically and asymmetrically above the vocal folds. In addition, the width of the parallel supraglottal geometry (that which did not include false folds) was systematically varied to study the effect of this parameter on the model response. Variations in model output were quantified by comparing glottal width, frequency, flow rate, pressures, and wave velocity measures. In addition, the glottal jet was qualitatively analyzed.

1.4.2 Effect of Modeling Choices on the Flow-Induced Response of a Computational Vocal Fold Model (Chapter 3)

The effects of various modeling choices were analyzed by systematically varying contact line location and Poisson's ratio. In addition, two models that were geometrically and parametrically identical were used to analyze the effect of assuming symmetry; in one model only half of the larynx (one vocal fold) with a symmetry assumption was included, and in the other, the full larynx with two vocal folds was modeled. Comparison of these two models allowed for evaluation of the symmetry assumption. As in the studies of Chapter 2, variations in model output were quantified by comparing measures of glottal width, frequency, flow rate, pressures, and wave velocity, as well as qualitative comparisons of the glottal jet.

2 EFFECT OF SUPRAGLOTTAL GEOMETRY ON THE FLOW-INDUCED RESPONSE OF A COMPUTATIONAL VOCAL FOLD MODEL

2.1 Introduction

Phonation is the result of a complex coupling between vocal fold tissue dynamics and respiratory aerodynamics. Air pressure from the lungs causes the folds to spread apart. As air is accelerated the intraglottal pressure lowers. The elasticity of the vocal fold, as well as the low pressure in the glottis, causes the folds to come back together. The process then repeats in a nominally periodic fashion.

As the flow leaves the glottis, it separates from the vocal fold surface and forms a jet in the supraglottal region. The glottal jet is an important part of voice production. Simulations and experiments have shown that the glottal jet may vary significantly from one cycle to the next (e.g., Triep et al., 2005; Erath and Plesniak, 2006a, 2006b, 2010; Tao et al., 2007; Luo et al., 2009; Zheng et al., 2011a). Several studies have suggested that these variations could have a significant impact on speech production (Triep et al., 2005; Drechsel and Thomson, 2008; Zheng et al., 2009; 2011a). Because of the highly coupled interaction of the air flow and vocal folds, it is important to understand whether these inter-cycle glottal jet variations influence the motion of the vocal folds themselves. It is therefore of interest to study factors that influence glottal jet dynamics and to quantify their associated impacts on vocal fold vibration.

9

One factor that contributes to the characteristics of the glottal jet is the downstream (supraglottal) geometry (Triep et al., 2005; Drechsel and Thomson, 2008; Finnegan and Alipour, 2009; Zheng et al., 2009). Using PIV data from the supraglottal region of a pair of synthetic self-oscillating vocal folds, several researchers (Neubauer et al., 2007; Drechsel and Thomson, 2008; Becker et al., 2009) have studied the asymmetry in the flow downstream of the glottis. Neubauer et al. (2007) focused on the flow structures present and identified vortex generation, vortex shedding, and jet flapping. Drechsel and Thomson (2008) showed that asymmetric placement of the supraglottal vocal tract with and without false vocal folds (FVF) caused variations in the glottal jet and discussed possible explanations for these variations.

Synthetic vocal fold model-based experiments can lead to many insights, but they have some limitations. In their study, Drechsel and Thomson (2008) mentioned that asymmetry inherent in the physical model of the vocal folds likely caused some degree of asymmetry in the flow; therefore, not all of the features that they observed could be confidently attributed to the supraglottal geometry. This was due to general inability to create perfectly symmetric material properties, geometries, and positioning using synthetic models. Additionally, while the motion of the synthetic vocal folds used in some studies (Neubauer et al., 2007; Drechsel and Thomson, 2008; Becker et al., 2009) was, in general, similar to that of actual human vocal folds, it lacked a significant mucosal wave. Furthermore, as in any physical model, obtaining a great deal of detail about the flow within the glottis as well as details of the vocal fold motion is very difficult.

These limitations can be remedied using a computational model in which a perfectly symmetric model (within the numerical limitations of the computer) can be analyzed. Such a computational model allows for a detailed view of the vocal fold motion as well as the flow within the glottis, and for precise control over geometry and material properties.

Some studies have relied on computational models to simulate flow through the glottis; however, due to computational costs, many have assumed a symmetrical solution (e.g., Zhang, 2009; Pickup and Thomson, 2011). By modeling only half of the larynx, these models reduce computational cost. They provide insight into vocal fold motion and aerodynamics, but do not capture asymmetry in the supraglottal jet or vocal fold vibration.

Several recent studies have included both vocal folds (e.g., Tao et al., 2007; Luo et al., 2009; Zheng et al., 2010). This allowed for modeling of the asymmetry in the supraglottal flow that has been observed experimentally. Zheng et al. (2009) used a 2D immersed boundary method to model fluid structure interaction between vocal folds modeled with a finite element approach and an airway modeled with a 2D Navier-Stokes solver. With this model, they studied the influence of the presence of FVFs on vocal fold vibration and translaryngeal flow impedance. Tao et al. (2007) used a computational two-mass model of the vocal folds with a CFD model of the airway to investigate the asymmetry of the glottal jet through symmetric vocal folds as well as the pressure profiles through the glottis. Xue et al. (2010) used a similar two-mass model to study the effects of asymmetric vocal fold properties on phonation. Zheng et al. (2011a) studied the cause of glottal jet asymmetries using an immersed boundary method with prescribed vocal fold motion and concluded that glottal jet deflection was mainly initiated by asymmetric downstream vortices.

While these previous computational models have been useful in helping to advance the understanding of glottal jet aerodynamics, additional knowledge can be gained from further studies. Each of the above-mentioned computational models has utilized a symmetrically-positioned supraglottal region; therefore, a computational model with off-axis placement of the supraglottal geometry is useful to further understand its effect on the glottal jet and vocal fold

motion. Additionally, the motion of the computational models previously performed exhibited a limited or non-existent mucosal wave. This mucosal wave is an important geometric characteristic of vocal fold motion. Therefore, to more fully understand the complex interaction of the vocal folds and the glottal jet, it is useful to study a model which exhibits a more pronounced self-oscillating mucosal wave.

In this chapter a computational flow-structure interaction model of the vocal folds and airway was used to study the effects of changing supraglottal geometric parameters on the motion of the vocal folds, the glottal jet dynamics, separation point locations, and intraglottal pressure profiles. A model was created in which both the properties and geometries of the vocal folds and subglottal and glottal regions were perfectly symmetric. The model was adjusted to incorporate several supraglottal geometric features that were positioned either symmetrically or asymmetrically. Importantly, the model exhibited a pronounced mucosal wave. In the following sections, the numerical methods are described. The model and cases studies are presented, and the results and implications thereof are discussed.

2.2   Numerical Methods

The commercially-available finite element program ADINA was used to simulate the flow-induced vibration of a two-dimensional vocal fold model. This package has been used in previous studies of vocal fold vibration and of other biological flow-structure interaction problems (e.g., Thomson et al., 2005; Bertram, 2009; Valencia and Baeza, 2009). As illustrated in Fig. 2.1, two basic types of supraglottal duct were modeled to examine the effects of various geometries: a parallel walled duct and a duct with FVFs present. Supraglottal ducts were both positioned symmetrically above the true vocal folds, as well as offset to one side by a prescribed amount. In addition, the width of the symmetrically placed parallel duct was varied.
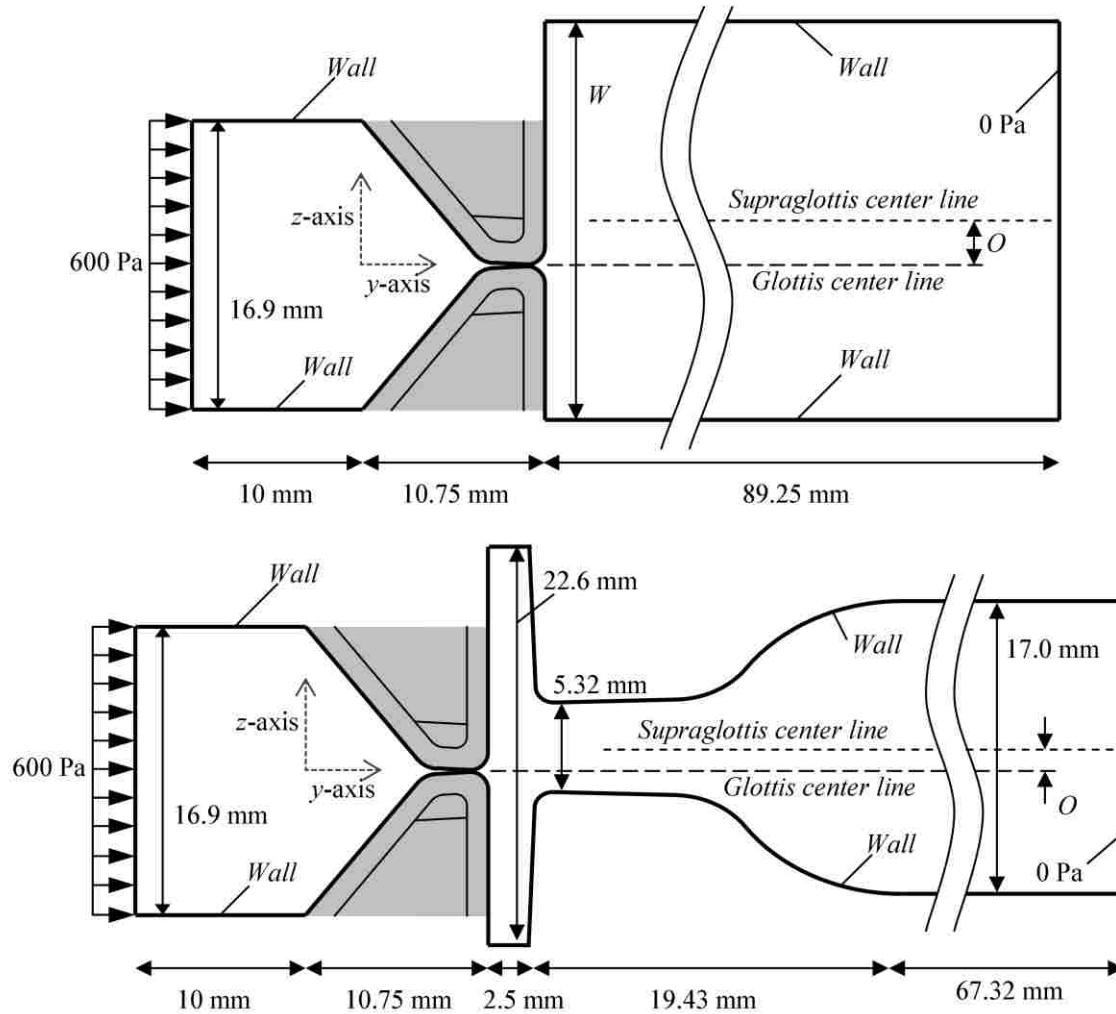
Figure 2.1: Airway geometry and boundary conditions for parallel supraglottal duct cases I-VIII (top) and for false vocal fold cases IX-XII (bottom). Note parameters of width (*W*) and offset (*O*).

2.2.1 Fluid Domain

Two basic parametric fluid domains, as can be seen in Fig. 2.1, were used to better understand the effects of supraglottal geometry. Each of the fluid domains utilized an identical inlet 1 cm long and 1.69 cm wide, an identical glottis, and was coupled to an identical vocal fold pair; in each case the supraglottal duct was 8.925 cm long. For cases without FVFs, the

13
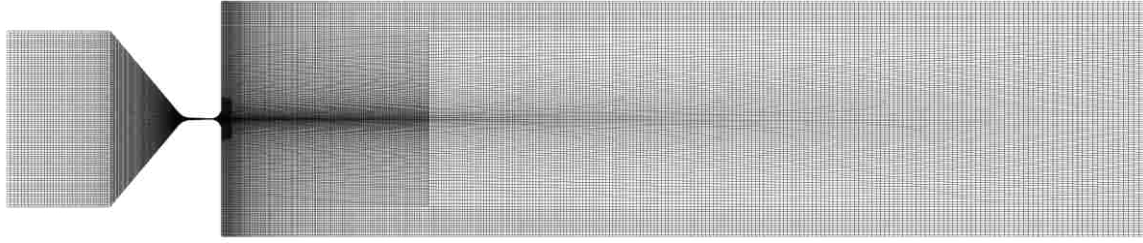
Figure 2.2: Airway mesh from case V.

downstream duct was modeled with parallel walls at various widths (*W*) and offsets (*O*) from the centerline. The FVFs included were similar to those reported by Lou et al. (2009), and were scaled to adjust for the smaller vocal folds used in this study. In order to maintain identical FVF geometry while allowing for an offset in the lateral position of the supraglottal duct, the ventricles were extended slightly in the lateral direction and were 2.26 cm wide. The gap between the FVFs was maintained at 5.32 mm. The geometry was oriented in the *yz*-plane such that flow was primarily in the *y*-direction (see Fig. 2.1).

The fluid domain for case V (see Sec. 2.2.4 for discussion of cases) was modeled with 76,640 quadrilateral elements and 77,443 nodes. The mesh was more refined in the region of the vocal folds (see Fig. 2.2). The air density and viscosity values were 1.2 kg/m^3 and 1.8×10^{-5} Pa·s, respectively. As shown in Fig. 2.1, the lateral edges of the inlet and outlet ducts, including the FVFs when present, were treated as walls (i.e., no displacement and no slip). The interface between the true vocal folds and the airway was treated with the FSI boundary condition that enforced consistent stress and displacement of the fluid and solid domains along the wetted interface. The inlet was driven with a constant normal traction of 600 Pa, and the outlet maintained at 0.0 Pa. The flow was treated as unsteady, laminar, and incompressible.

2.2.2 Solid Domain

The vocal fold model was a symmetric pair of vocal folds, each the same as the model which was developed by Smith (2011) and included four separate layers: body (muscle), ligament, superficial lamina propria, and epithelium layers. To summarize, the model outer geometry was based on the "M5" geometry of Scherer et al. (2001) with a convergent included angle of 2° between the medial surface of one fold and the medial plane (see Fig. 2.3), for a total included angle of 4° in the glottis. The epithelium layer was a 0.05 mm-thick, linearly elastic material. The other layers were modeled as hyperelastic Ogden solids with nonlinear stress-strain relations. Dimensions and mechanical property values are given in Fig. 2.3 and were in line with physiological ranges for humans (for further details, see Smith, 2011). Each layer had a Poisson's ratio and density of 0.49 and 1070 kg/m^3, respectively. The high stiffness of the epithelium allowed for an extremely soft cover layer that produced a pronounced mucosal wave. Rayleigh damping with coefficients of $\alpha = 56.549$ and $\beta = 3.979 \times 10^{-5}$ was used, resulting in a damping ratio of approximately 0.05 between the frequency range of 100 and 300 Hz.
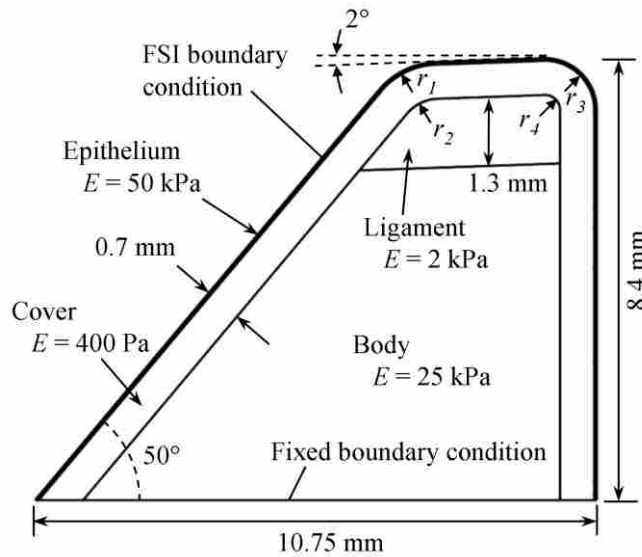
Figure 2.3: Vocal fold model geometry, boundary conditions, and material properties. Radii r_1, r_2, r_3, and r_4 are 1.5, 0.8, 1.0, and 0.3 mm respectively.
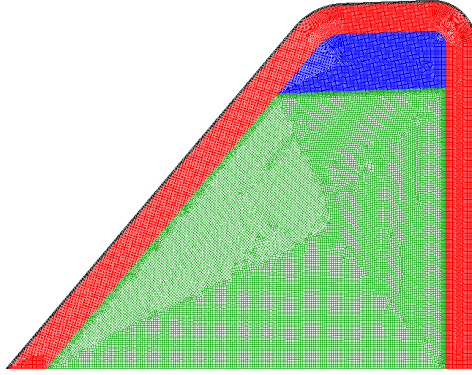
Figure 2.4: Vocal fold mesh consisting of body (green), ligament (blue), superficial lamina propria (red), and epithelium (black).

The solid domain consisted of two vocal folds with a total of 100,072 quadrilateral elements (50,036 per vocal fold) and 101,412 nodes (50,706 per vocal fold). An image of this mesh for one of the folds can be seen in Fig. 2.4. The lateral edges of the vocal folds were fixed and the inferior, medial, and superior edges were treated with the FSI boundary condition (see Fig. 2.3). To prevent complete collapse of the fluid domain, a pair of contact lines was utilized to keep the modeled vocal folds from contacting one another. These lines were located at ± 0.025 mm from the centerline of the glottis, maintaining a minimum glottal gap of 0.05 mm.

2.2.3   Verification and Validation

Numerical verification was performed using grid and time step independence studies. To ensure time step independence, the model was solved using time step sizes of 1.25×10^{-5} s and 2.5×10^{-5} s. The glottal width waveforms over the first 0.05 seconds were compared and found to be nearly graphically indistinguishable (see Fig. 2.5). Cases with 68480 and 259440 elements in the fluid domain (double the grid density in each dimension) were run to verify grid independence. The plot of glottal width waveform for the refined mesh was indistinguishable from that of the original grid spacing (Fig. 2.5). In addition several other output parameters (F_0,

16
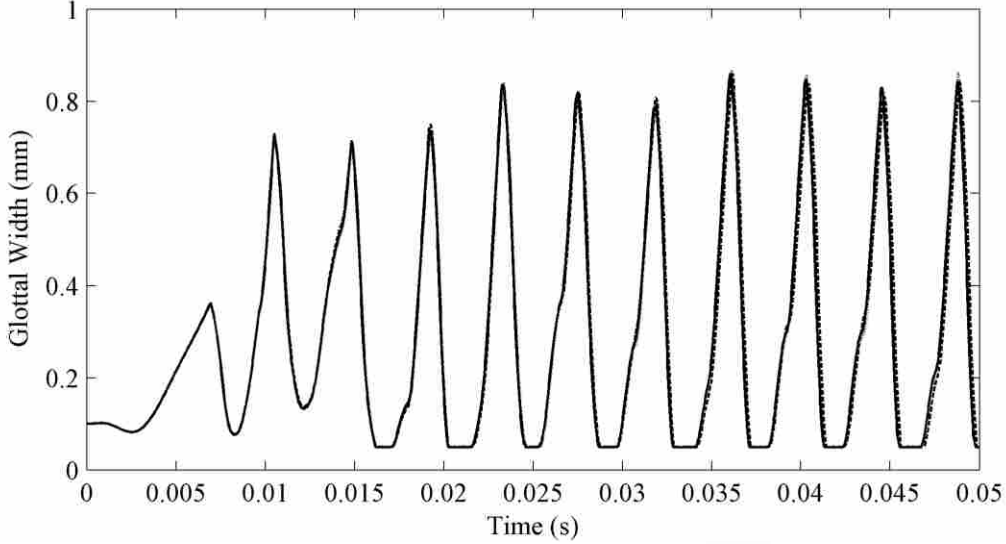
Figure 2.5: Grid and time step independence study results. (— = Original grid and time step, --- = finer grid, ···· = smaller time step). Note that all three curves are nearly directly on top of one another.

G_{max}, G_{avg}, O_q, Q_{max}, and Q_{avg} which are defined in Sec. 2.2.5) of the three simulations were numerically compared (see Table 2.1). Variations between cases were about 1% for all variables except Q_{max} which decreased by 8.4% with the smaller time step. These results confirmed that the coarser grid size and the larger time step of 2.5×10^{-5} s were adequate.

Each simulation ran for 10,000 time steps of 2.5×10^{-5} s each for a simulation time of 0.25 s. This required approximately 380 processor hours per simulation on the Brigham Young University Fulton Supercomputing hardware (Dell PowerEdge M610 equipped with dual, quad-core, 2.8 GHz Intel Nehalem processors and 24 GB of memory; simulations each ran on four cores of a single processor).

Table 2.1: Measured values of frequency (F_0), maximum glottal width (G_{max}), average glottal width (G_{avg}), open quotient (O_q), maximum flow rate (Q_{max}), and average flow rate (Q_{avg}) in the grid and time step independence studies.

Case	F_0 (Hz)	G_{max} (mm)	G_{avg} (mm)	O_q	Q_{max} (ml/s)	Q_{avg} (ml/s)
Original	234.7	0.829	0.298	0.744	368.1	136.6
Finer grid	234.2	0.827	0.300	0.746	367.0	138.9
Smaller time step	235.0	0.832	0.298	0.740	337.2	136.8

17

Validation was done by comparing model results (e.g., flow rate, frequency, general motion etc.) with those of other computational simulations, synthetic models, excised larynges, and measurements from actual human subjects. These comparisons are presented throughout the results and discussion section and show that the model yielded a reasonable approximation of actual phonation.

2.2.4 Case Studies

As was mentioned above, various cases with different airway geometries were utilized to compare the effects of supraglottal duct width, FVFs, and lateral offset of the supraglottal duct on vocal fold vibration and airway fluid dynamics. In all, twelve cases (I-XII) were studied. The general geometries are represented in Fig. 2.1 and parameter values are given in Table 2.2. To study the effect of supraglottal duct width, an airway consisting of symmetrically placed parallel walls in the supraglottal region with a variable width, W, was used. To study the effects of including the FVFs, an airway with FVFs (case IX) was included. By comparing cases I and IX

Table 2.2: Geometric parameters for cases I through XII.

Case #	Supraglottal geometry type	Supraglottal duct width (W) (mm)	Offset of supraglottal duct (O) (mm)
I	Parallel duct	17.0	0.0
II	Parallel duct	18.4	0.0
III	Parallel duct	19.8	0.0
IV	Parallel duct	21.2	0.0
V	Parallel duct	22.6	0.0
VI	Parallel duct	22.6	0.1
VII	Parallel duct	22.6	1.4
VIII	Parallel duct	22.6	2.8
IX	False Vocal Folds	17.0	0.0
X	False Vocal Folds	17.0	0.1
XI	False Vocal Folds	17.0	1.4
XII	False Vocal Folds	17.0	2.6

the effects of including FVFs could be explored. To examine the effects of lateral offset, the supraglottal geometries of cases V and IX were offset in the lateral direction by a distance O, comprising cases VI-VIII and cases X-XII for the parallel and FVF cases respectively.

2.2.5   Variable Definitions

In the following sections, several output quantities are used to compare results. These are here briefly defined:

- *Left glottal half width, G_L.* The minimum distance from the left vocal fold to the medial plane (see Fig. 2.6).

- *Right glottal half width, G_R.* The minimum distance from the right vocal fold to the medial plane (see Fig. 2.6).

- *Glottal width, G.* The minimum distance between opposing vocal folds. It is equal to G_L+G_R (see Fig. 2.6).
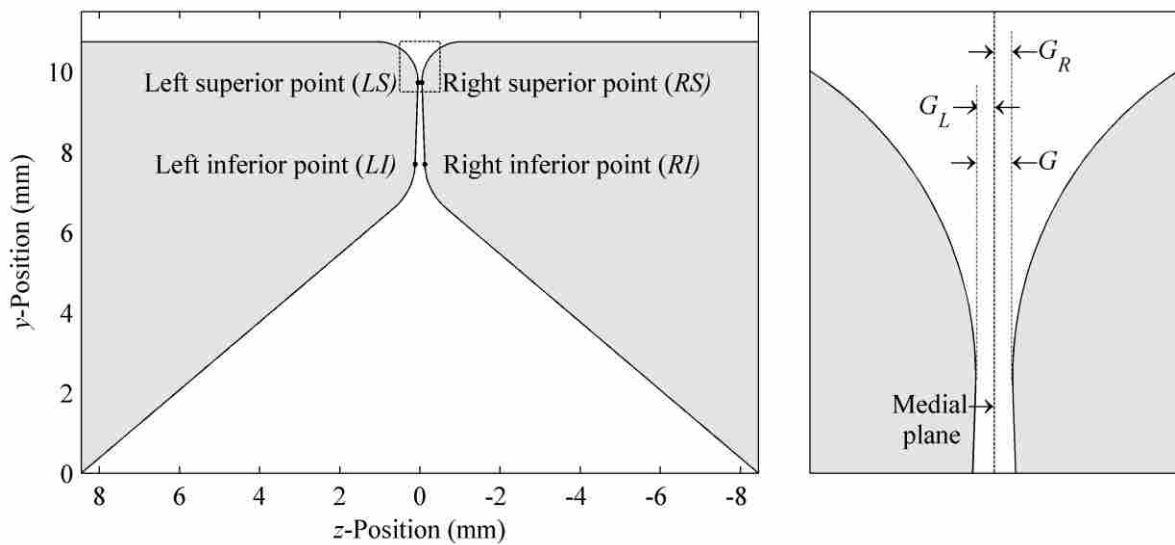
Figure 2.6: Location of the points used to compare symmetry of motion (left plot) (dashed box denotes outline of left plot), and close up view with definitions for glottal width (G) and left and right glottal half-widths (G_L and G_R) (right plot).

19

- *Maximum glottal width, G_{max}.* The maximum glottal width, G, over one cycle. This was averaged over 10 periods.

- *Average glottal width, G_{avg}.* The average of the glottal width, G, over one cycle.

- *Open quotient, O_q.* The fraction of a cycle in which the glottal width was not "closed" (i.e., when $G > 0.05$ mm). This was averaged over 10 periods.

- *Fundamental frequency, F_0.* The frequency calculated from the inverse of the period of the glottal width data. This was averaged over 10 periods.

- *Volume flow, Q.* Calculated as $Q = 0.015\text{m}*\int vdz$ where v is the fluid velocity in the superior (y) direction. It was calculated at $y = 1.3$ cm which was just downstream of the maximum position of the superior surface of the vocal fold and upstream of the inferior surface of the FVF when present (see Fig. 2.6). A distance of 0.015 m was used to scale the flow rate measurement in the 3rd (anterior-posterior) dimension.

- *Maximum flow rate, Q_{max}.* The maximum flow rate, Q, over one cycle. This was averaged over 10 periods.

- *Average flow rate, Q_{avg}.* The average of the flow rate, Q, over one cycle.

- *Wave velocity, V_W.* The speed at which the mucosal wave propagates. Calculated as the slope of a linear fit through the y-position of minimum glottal width over time from phases *F-C* of each cycle averaged over ten cycles (described further in Sec. 2.3.1; see Fig. 2.9).

- *Inferior point on the right vocal fold RI.* See (Fig. 2.6).

- *Inferior point on the left vocal fold LI.* See (Fig. 2.6).

- *Superior point on the right vocal fold RS.* See (Fig. 2.6).

- *Superior point on the left vocal fold LS.* See (Fig. 2.6).

- *Correlation coefficient in the y-direction (inferior-superior) of the inferior points, R_{YI}.* This is calculated as

$$R_{YI} = \frac{\sum y'_{LI} y'_{RI}}{\sqrt{\sum y'_{RI} y'_{RI} \times \sum y'_{LI} y'_{LI}}} \, ,$$

(2.1)

where y'_{LI} and y'_{RI} are the fluctuations in the y-position *LI* and *RI* points about their mean values. The summations are over time steps for 10 cycles of vibration.

- *Correlation coefficient in the z-direction (medial-lateral) of the inferior points, R_{ZI}.* Similar to R_{YI} but in the z-direction.

- *Correlation coefficient in the y-direction (inferior-superior) of the superior points, R_{YS}.* Similar to R_{YI} but using the superior points.

- *Correlation coefficient in the z-direction (medial-lateral) of the superior points, R_{ZS}.* Similar to R_{ZI} but using the superior points.

- *Reynolds number, Re.* Calculated based on flow rate (Q) as

$$\mathrm{Re} = \frac{QD_H}{\nu A} = \frac{4Q}{\nu P} = \frac{4\rho Q}{\mu P} \, ,$$

(2.2)

where D_H, ν, μ, ρ, A, and P are the hydraulic diameter, kinematic viscosity, dynamic viscosity, density, area, and wetted perimeter respectively.

- *Wetted perimeter, P.* The perimeter in contact with the fluid at the location Re is calculated. In this case it is $2{\times}W + 2{\times}0.015$ m, where the distance 0.015 m is the dimension used to scale the flow in the third dimension.

- *Separation point.* As shown in Fig. 2.23 (further described in Sec. 2.3.6), the separation point was manually located by determining the point at which the edge of the jet (blue or

21

red band in the vorticity plot) detached from the vocal fold surface. This was done for 10 cycles at eight phases per cycle.

2.3   Results and Discussion

2.3.1   Glottal Motion

As can be seen from the outline of the vocal folds at various phases of a single cycle for case I (Fig. 2.7), this model yielded a significant mucosal wave. The mucosal wave in this model was much more pronounced than that seen in several other simulations (Tao et al., 2007; Luo et al., 2009; Zheng et al., 2009; 2010; Pickup and Thomson, 2011). As the cover layer deformed on the model, a small bulge formed near the exit radius of the glottis. Initially this bulge was the location of *G* (Fig. 2.7, phase *C*). Soon after, the inferior edge of the medial surface moved medially, resulting in an upstream shift in location of minimum glottal width (Fig. 2.7, phase *E*). The glottal gap continued to decrease until the medial surface reached the contact line. The location of minimum glottal width moved superiorly until it separated from the contact plane near the superior end of the medial surface (Fig. 2.7, phases *G-B*). This motion, which was representative of the motion of each of the twelve cases, caused a pronounced alternating
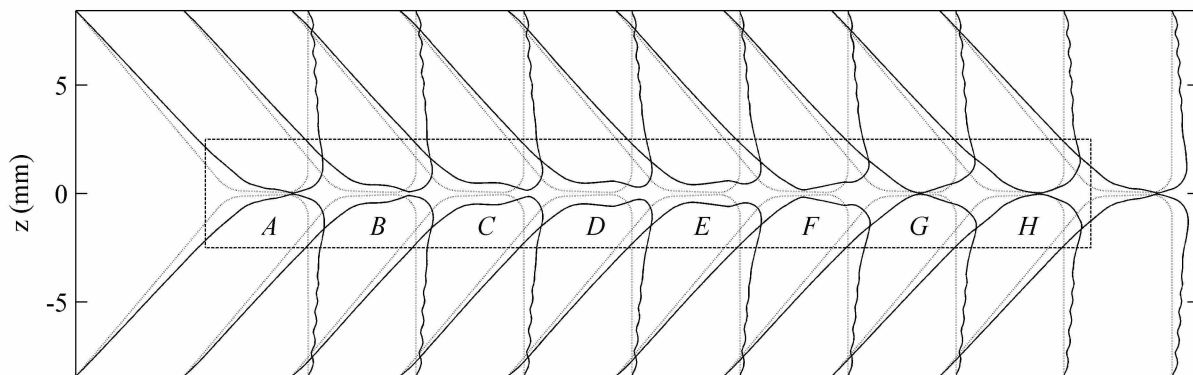
Figure 2.7: Vocal fold profiles at various phases of one cycle (profile of each phase shifted by 5 mm in *y*-direction). Undeformed profiles are shown with dotted lines. Dashed lines denote outline of Fig. 2.14. Phases *A* through *H* are marked for reference.

22
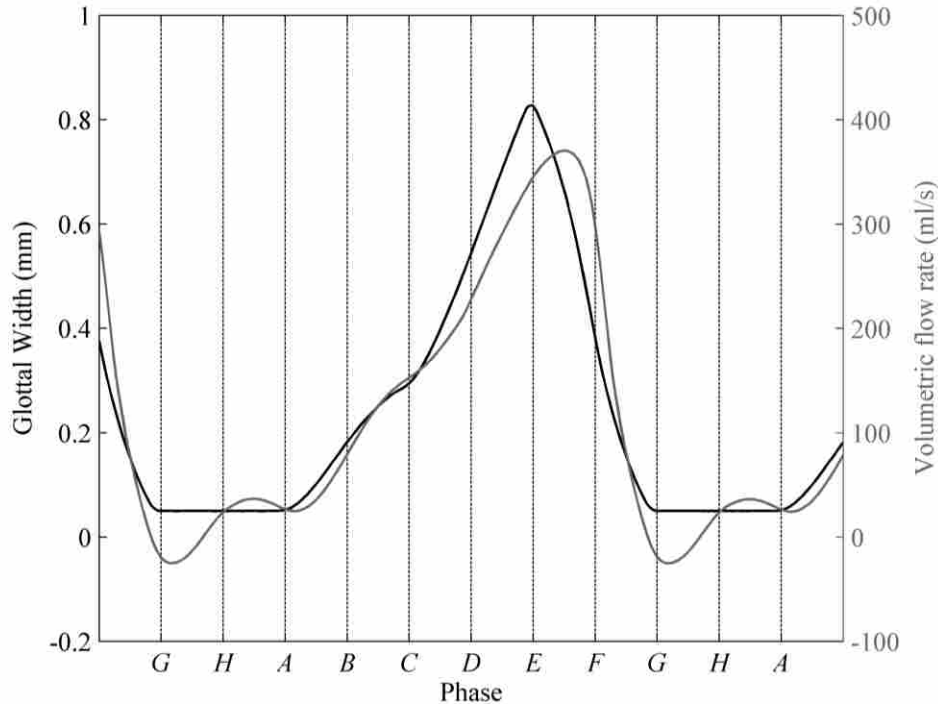
Figure 2.8: Glottal width (black, left axis) and flow rate (gray, right axis) from a typical case. Vertical dashed lines represent phases *A*-*H*.

convergent/divergent intraglottal profile during each cycle. These two geometric vibratory features – mucosal wave and alternating convergent/divergent motion – are well-known characteristics of human vocal fold motion.

Figure 2.8 shows waveforms of *G* and *Q*. The *G* waveform had several notable characteristics. First, there was a fairly sharp peak at the phases at which G_{max} occurred (phase *E*). As can be seen in Figs. 2.7 and 2.8, this peak coincided with the transition from a convergent opening profile to a divergent closing profile. Occurring near this phase were two locations of equal minimum glottal width (near the inlet and outlet radiuses of the glottis) that temporarily caused a nearly parallel glottis. This transition was marked by a peak in the *y*-position of the minimum glottal width (Fig. 2.9, discussed further below), which coincided with phase *E* of each cycle where the location of minimum glottal width jumped from the superior to inferior portion
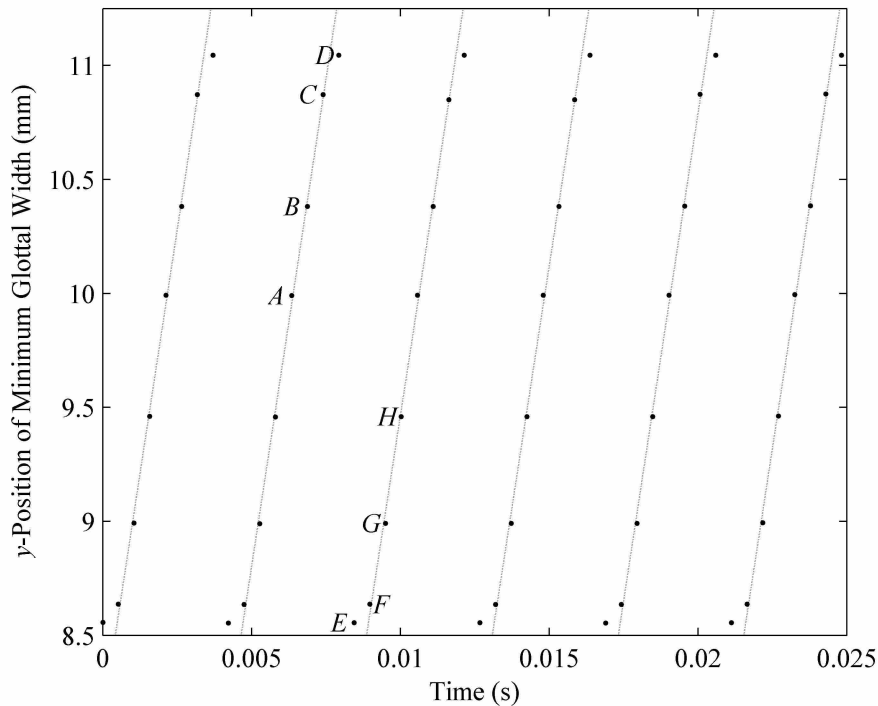
Figure 2.9: The *y*-position of the minimum glottal width vs. time for six cycles of a typical case is shown. Black dots are *y*-positions of minimum glottal width at each phase. Dotted lines are linear fits used to calculate wave velocity. Phases *A* through *H* are marked on one series for reference.

of the medial surface. This was a consequence of the presence of the mucosal wave. The "closed" portion of the cycle (phases *G-A*), where the minimum glottal width was at a constant value of 0.05 mm, lasted for approximately one-quarter of the cycle, corresponding to an O_q ratio close to 0.75.

As can be seen in Table 2.3, G_{max} values ranged from 0.831 to 0.854 mm. These are similar to typical values in humans of approximately 1 mm (Schuberth et al., 2002). The frequency ranged from 236.4 to 244.2 Hz, while O_q values ranged from 0.691 to 0.755. These values of are consistent with measurements of human phonation; e.g., Baken and Orlikoff (2000) reported a mean O_q value of 0.71 with a range of 0.51 to 1.0 for normal speakers with a fundamental frequency of 225 Hz. Values for individual cases are listed in Table 2.3.

24

Table 2.3: Measured values of frequency (F_0), maximum glottal width (G_{max}), average glottal width (G_{avg}), open quotient (O_q), wave velocity (V_W), correlation coefficients (R_{YI}, R_{ZI}, R_{YS}, and R_{ZS}), maximum flow rate (Q_{max}), and average flow rate (Q_{avg}).

Case	F_0 (Hz)	G_{max} (mm)	G_{avg} (mm)	O_q	V_W (m/s)	R_{YI}	R_{ZI}	R_{YS}	R_{ZS}	Q_{max} (ml/s)	Q_{avg} (ml/s)
I	237.0	0.845	0.296	0.735	0.829	0.904	0.998	0.962	0.993	369.5	136.6
II	237.4	0.837	0.297	0.741	0.850	0.933	0.998	0.972	0.993	367.8	137.2
III	237.0	0.840	0.296	0.743	0.850	0.900	0.997	0.955	0.993	366.9	136.5
IV	237.1	0.836	0.296	0.748	0.852	0.824	0.996	0.917	0.993	367.5	137.6
V	237.0	0.832	0.295	0.754	0.851	0.887	0.996	0.947	0.994	367.8	137.9
VI	236.5	0.831	0.295	0.753	0.850	0.914	0.996	0.968	0.994	367.2	137.9
VII	236.4	0.834	0.293	0.747	0.848	0.899	0.997	0.953	0.993	365.7	136.5
VIII	237.1	0.831	0.296	0.755	0.835	0.890	0.995	0.963	0.993	367.3	137.5
IX	243.9	0.844	0.302	0.734	0.854	0.106	0.995	0.355	0.960	399.8	146.7
X	244.2	0.840	0.301	0.697	0.850	0.361	0.996	0.594	0.975	398.8	146.0
XI	244.2	0.849	0.302	0.708	0.863	0.883	0.999	0.925	0.994	402.8	145.8
XII	242.4	0.854	0.301	0.691	0.857	0.896	0.995	0.930	0.992	389.2	142.5

From the data of *y*-location of minimum glottal width vs. time, it was possible to calculate the velocity of the mucosal wave (V_W) (Titze et al. 1993). The average V_W of the various cases was 0.849 m/s with individual values found in Table 2.3; these values are in the range of 0.5 to 2.0 m/s reported by Titze et al. (1993) for excised canine larynges.

There was no appreciable change in the glottal width waveform between any of the cases. In cases with a parallel supraglottal duct (cases I-VIII), there was a maximum variation in F_0 of less than 0.5% and maximum variations in G_{max} and G_{avg} of 1.62% and 1.14%, respectively. Additionally there was a maximum variation in V_W of only 2.71%. These values are on the order of the cycle-to-cycle variations for a given case. In the cases including FVFs (cases IX-XII) these variations were similar with the maximum variation in F_0, G_{max}, G_{avg}, and V_W being 0.73%, 1.66%, 0.41%, and 1.56%, respectively. In addition, including FVFs (comparing case IX to case I) had little effect. It decreased G_{max} by 0.08% and increased F_0, G_{avg}, and V_W by 2.92%, 1.79%, and 3.07% respectively.

2.3.2 Glottal Asymmetry

Because of the asymmetry of the glottal jet, the symmetric vocal folds exhibited some degree of asymmetric motion. As was done by Zheng et al. (2009), the asymmetry of the vocal fold motion was visualized with the aid of phase plane plots and quantified by calculating the correlation coefficient between paired points on the two vocal folds. Points at the downstream edge of the entrance radius (inferior point) to the glottis as well as the upstream edge of the exit radius (superior point) of each vocal fold were used to generate these data (Fig. 2.6). Cycle-to-cycle variation in the motion of a single vocal fold was evidenced by the fact that a given point did not trace out the same path in space through each cycle (see Fig. 2.10). A degree of asymmetry in the motion of the paired vocal folds was seen in the y-direction (inferior-superior) of both inferior and superior points and was evidenced by the divergence of the data from an ideal 45° line on the phase plane plots (Figs. 2.11 and 2.12).
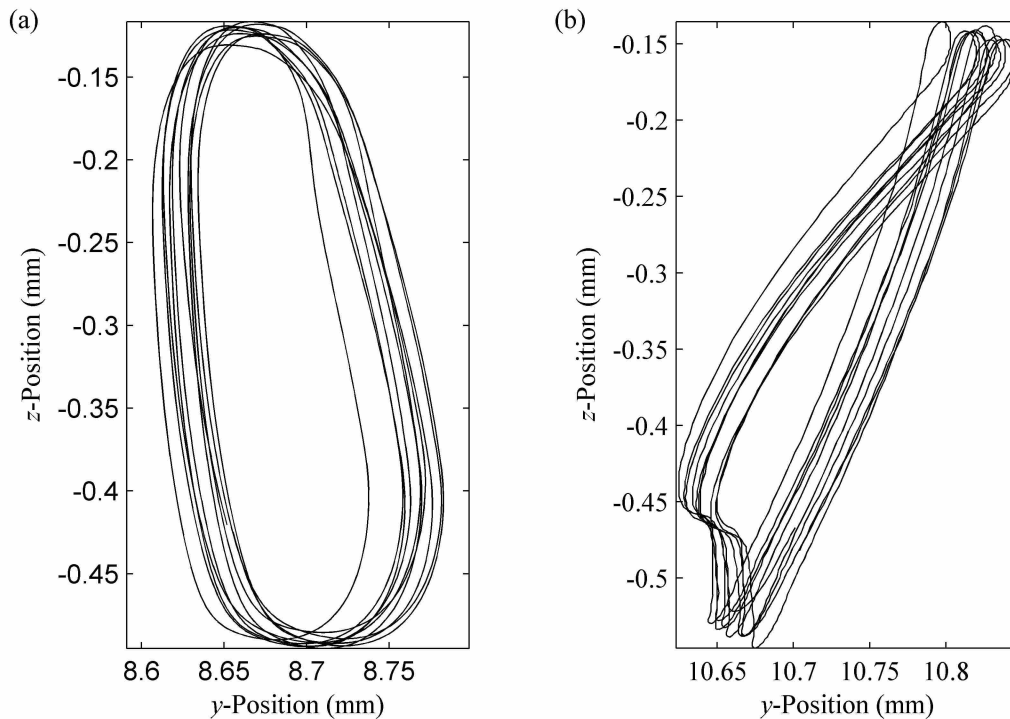
Figure 2.10: Motion of *RI* (a) and *RS* (b) points of case VIII for ten cycles.
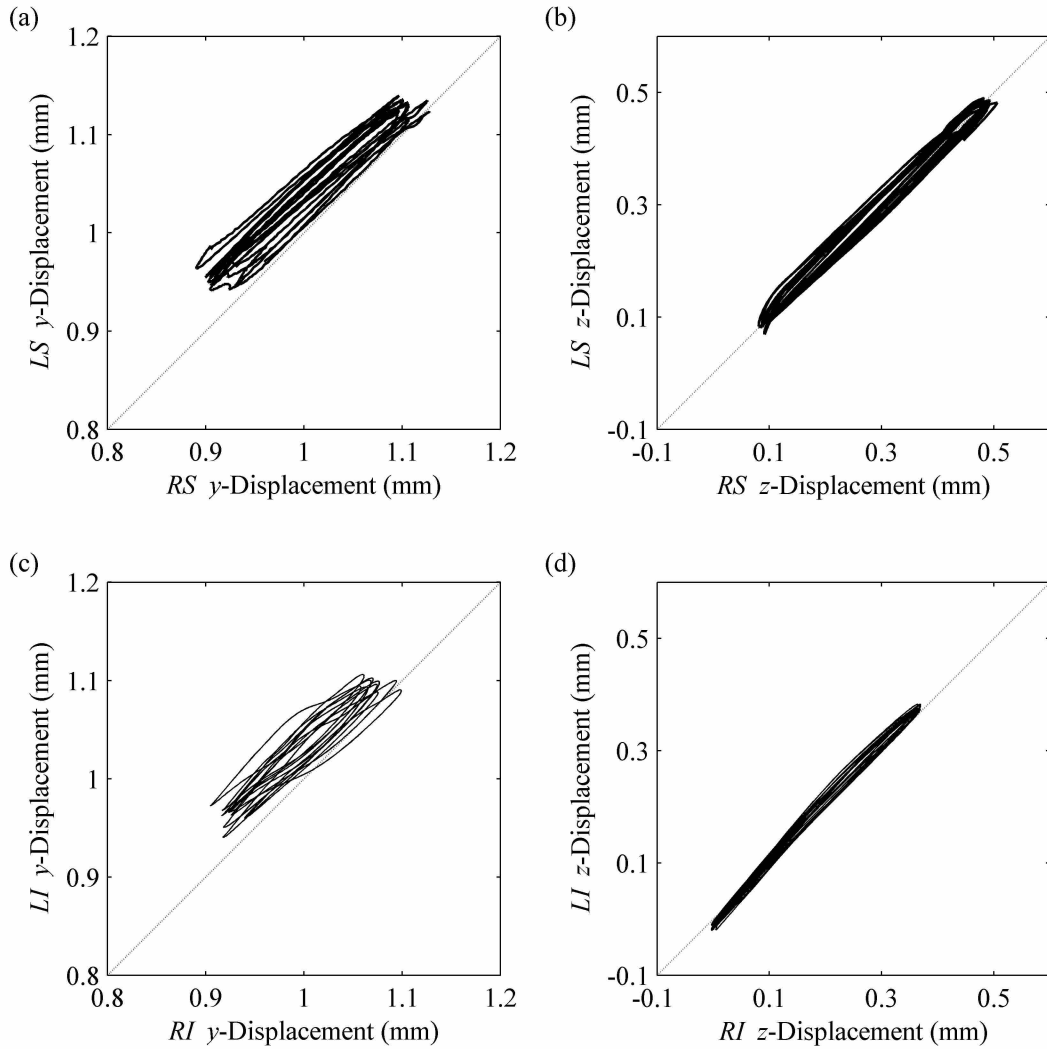
Figure 2.11: Phase plane plots for case I. Plot for the superior points in the *y*-direction (a) and *z*-direction (b) as well the inferior points in the *y*-direction (c) and *z*-direction (d). Note that the negative *z*-displacement was used for the right points to maintain positive slope. The dotted lines represent the path of perfectly symmetric motion.

The correlation coefficients (R_{YI}, R_{ZI}, R_{YS}, and R_{ZS}) of a model with perfectly symmetric motion would each be 1.0. However, much lower values were seen in several of the cases, denoting a degree of asymmetry (see Table 2.3). In all cases there was the highest degree of symmetry in R_{ZI} and the least symmetry in R_{YI}. Also the centered FVF case (IX) had the highest degree of asymmetry for all four correlation coefficients with exceptionally low values of R_{YI} and

27
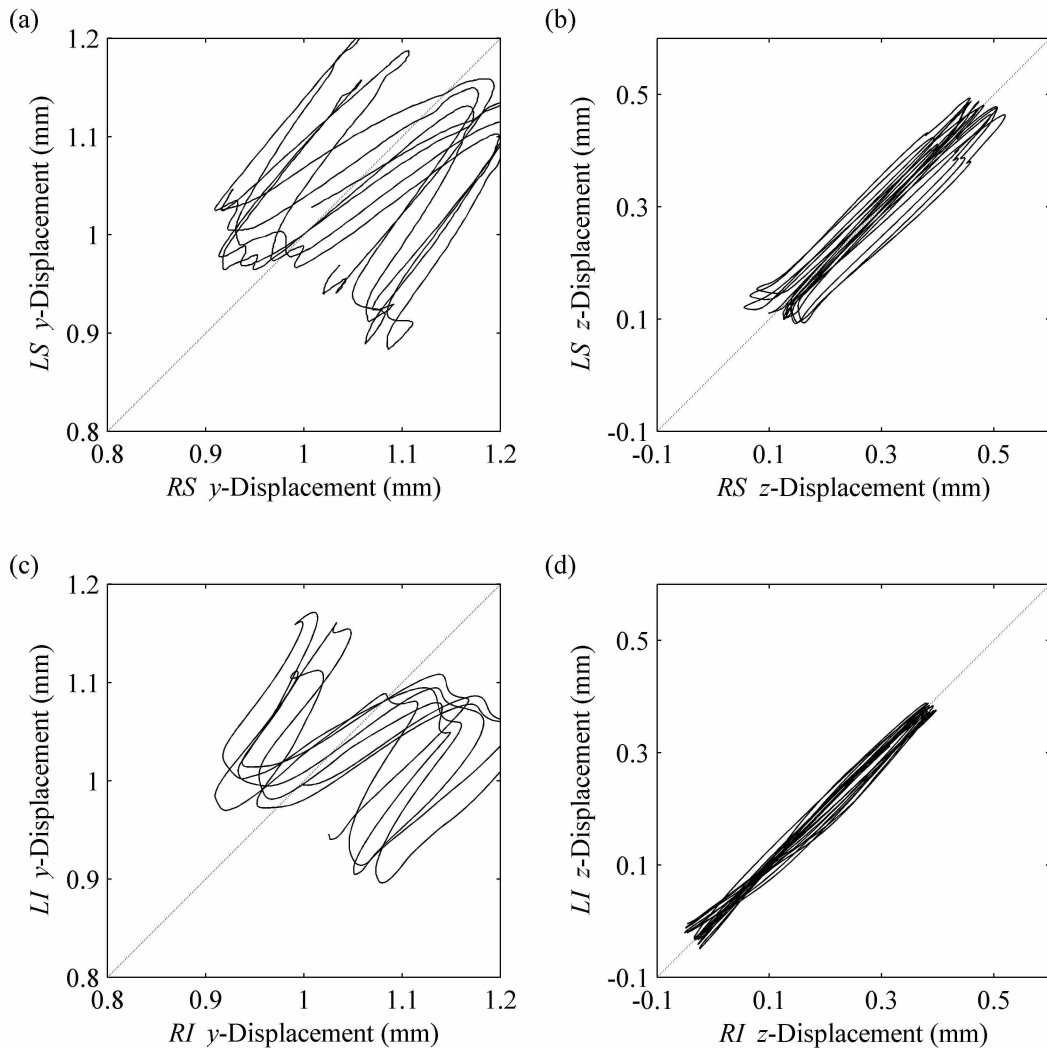
Figure 2.12: Phase plane plots for case IX. Plot for the superior points in the *y*-direction (a) and *z*-direction (b) as well the inferior points in the *y*-direction (c) and *z*-direction (d). Note that the negative *z*-displacement was used for the right points to maintain positive slope. The dotted lines represent the path of perfectly symmetric motion.

R_{YS} (0.106 and 0.355 respectively). As will be shown later, this case exhibited the largest variability in glottal jet motion, which may be the cause of vocal fold asymmetry.

The magnitudes of the correlation coefficients measured in this study are somewhat different from those reported by Zheng et al. (2009). Both research studies found a greater degree of symmetry in the medial-lateral (ML) direction than in the inferior-superior (IS)

direction (for example Zheng et al., 2009 reported R values for the superior points of 0.954 and 0.653 in the ML and IS-directions respectively). However, Zheng et al. (2009) showed that the addition of FVFs increased the symmetry in the IS-direction but decreased the symmetry in the ML-direction. The present research showed a decrease in all symmetry with the addition of centered FVFs. This was again attributed in the present study to the less consistent nature of the glottal jet when FVFs are included than when they are not.

It is also interesting to note the effect of the M-L alignment of the supraglottal duct on the symmetry of motion. With no FVFs present, there were only minor inconsistent changes (max variation of 3.0% in R_{YI}) in the symmetry of vocal fold motion as the supraglottal duct was offset. However, with FVFs in place, increased offset of the supraglottal geometry led to an increase in motion symmetry. R_{YI} increased from 0.106 to 0.882 as offset increased from 0.0 to 1.4 mm. As offset increased from 1.4 to 2.6 mm, changes in symmetry were insignificant. These results were again caused by the degree to which the glottal jet was consistent from one cycle to the next. More consistent jets, even when highly asymmetric, led to more symmetric motion. Section 3.4 contains a more detailed discussion of the glottal jet

The effects of the supraglottal width on symmetry of vocal fold motion were inconclusive. While increasing the width between 18.4 and 21.2 mm steadily decreased the symmetry in the y-direction (from $R_{YI} = 0.933$ to 0.824) the opposite of this trend was seen for the thinnest and widest ducts used. Additionally it had little effect, if any, on the symmetry of motion in the z-direction. It is believed that the consistent nature of the jet dominated the influence on the vocal fold motion and that models with less consistent jet behavior may exhibit more significant trends.

These phase plots (Figs. 2.11 and 2.12) and correlation coefficients help to compare asymmetry between cases, but they do not lend themselves to quantifying the magnitude of the asymmetric motion. One way to visualize and better quantify the degree of asymmetry was by comparing G_L and G_R over time (see Fig. 2.13). As can be seen there was a slight phase shift between G_L and G_R, but its magnitude was only approximately 0.05 ms and was fairly consistent through all of the cases. Larger variations were seen in the relative magnitudes of G_L and G_R at their peaks. For example in case I there was roughly 0.005 mm difference in magnitude and the same half width was consistently larger than the other; however, in case IX there was a 0.022 mm difference in magnitude which inconsistently switched as to which half width was greater. Another observed difference was shortly after the opening phase (see Fig. 2.13). In the parallel cases (I-VIII), one half width opened approximately 0.05 ms before the other, both then climbed at nearly the same rate in a nearly linear fashion for approximately one quarter of a cycle. At this
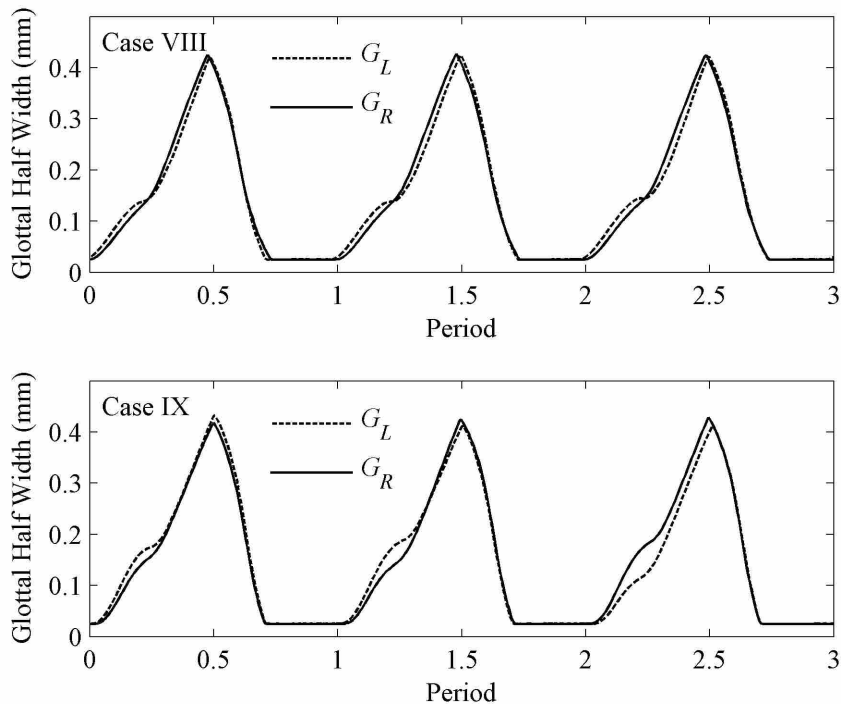
Figure 2.13: Glottal half widths for cases VIII (top) and IX (bottom)

30

point the leading half width leveled out for approximately 0.2 ms while the other maintained its slope. This caused the trailing half width to become the leading half width. This phenomenon was manifested in each of the parallel duct cases. However; in the FVF cases both folds would decrease in slope but at different times causing a larger disparity between the two half widths (see Fig. 2.13, bottom). These observed variations helped to quantify the size of asymmetry, but only in the z-direction.

The asymmetry could also be seen in the outlines of the vocal folds at various phases (Figs. 2.14 and 2.15). This asymmetry was most prevalent for cases where FVFs were present; however, it is difficult to see in full-scale plots. Figure 2.15 shows a close up view of the medial surface outlines for the left and right vocal folds plotted on top of one another. In this manner any asymmetry in both the y and z-direction can be seen. It is quite interesting to note that while there was obvious difference (of approximately 0.075 mm) in the z-position of the superior and inferior surfaces of the vocal folds, the medial surfaces were nearly identical. The same phenomenon was observed for all phases and cases, with some cases and phases having smaller
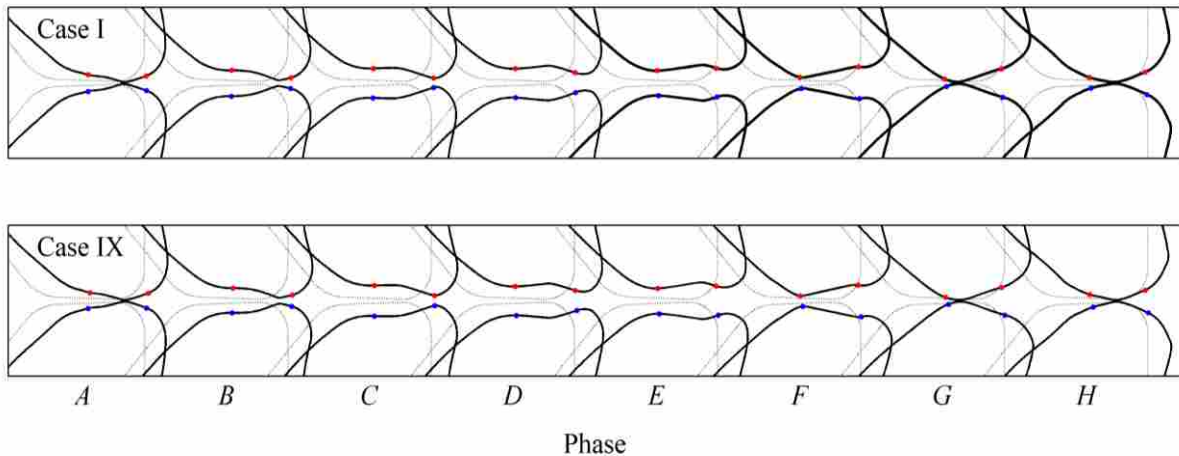
Figure 2.14: Visualization of asymmetry of vocal fold motion for case I (upper plot) and case IX (lower plot). Dotted lines represent undeformed vocal fold geometry, blue points represent points *RS* and *RI*, and red points represent *LS* and *LI*. There was a greater degree of asymmetry in case IX, but the magnitude of the asymmetry was small.

31
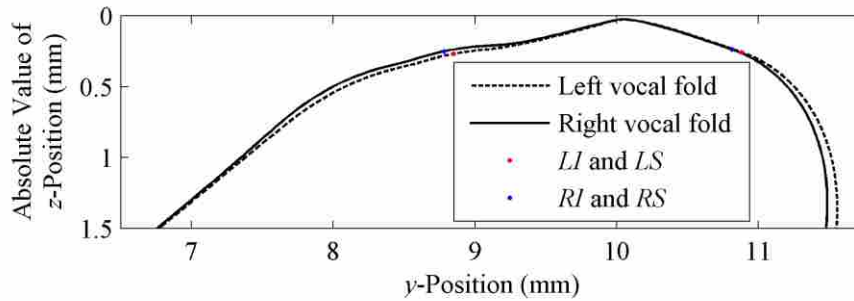
Figure 2.15: Close up view of vocal fold profile of phase *A* of case IX showing the asymmetry in the *y*-position of the vocal folds and the symmetric medial surfaces.

discrepancies in the superior and inferior surface. Even though one vocal fold was further downstream than the other and different portions of the cover were aligned, the area between the medial surfaces remained symmetric.

Even in the presence of very asymmetric downstream flow, the vocal folds remained fairly symmetric in their motion. There was maximum of about 0.075 mm of difference in the *y*-position of the vocal folds and 0.022 mm difference in the *z*-position in the most extreme case. This was less than 1% of the vocal fold height. In addition, the vocal fold surfaces responded in such a way that the medial surfaces of the vocal folds formed an extremely symmetric passage despite the small asymmetries in the mean vocal fold position.

2.3.3   Flow Rate

Volume flow rate is another important measurement in phonation. Case V was typical of the cases with Q_{max} and Q_{avg} values of 367.8 and 137.9 ml/s respectively. Values for the remaining cases can be found in Table 2.3 and are in line with measured mean flow rates of 72 to 223 ml/s in humans (Baken and Orlikoff, 2000) and slightly lower than that which has been reported in studies using other computational models (e.g., Luo et al., 2009, reported 405 to 755

cm^2/s peak flow rate and 180 to 314 cm^2/s mean flow rate, while Zheng et al., 2009, reported 587

ml/s to 865 ml/s peak flow rate and 266 ml/s to 322 ml/s mean flow rate). This discrepancy is

possibly due to the smaller vocal fold size used in this simulation (8.45 mm in the medial-lateral

direction vs. 9.9 mm used by Lou et al., 2009, and Zheng et al., 2009) as well as the lower

driving pressure (0.6 kPa in the present study vs. 0.8 to 1.2 kPa used by Lou et al., 2009, and 1.0

kPa used by Zheng et al., 2009). The trends seen in flow rate and driving pressure data from Luo

et al. (2009) as well as the size scales used, suggest that the lower flow rate observed was to be

expected.

For case V with a Q_{max} of 367.8 ml/s, and P = 0.0752 m, the peak Re was 1304. The

range of peak Re for all cases was 1297 in case VII to 1539 in case I which were below transition

for internal flows. This justified the choice of a laminar solver for the fluid domain.

As can be seen in Fig. 2.8, the flow rate waveform closely followed that of the glottal

width. However, there were a few notable distinctions. First, there was a definite phase shift with

the flow rate lagging the glottal width by approximately 0.25 ms. Additionally the flow rate

waveform was much smoother than that of the glottal width, with a much less pronounced peak

and no obvious discontinuity in slope at the beginning and end of the closed portion of the cycle.

Furthermore, the flow rate was briefly negative from just prior to glottal closure until

approximately halfway through the closed portion of the cycle. This was mainly due to the

diminishing glottal jet (due to glottis closure) and the large recirculation regions present (see Fig.

2.16 discussed in Sec. 2.3.4). The final feature of interest was the small local maxima of flow

rate during the latter half of the closed portion of the cycle.

The flow rate was largely unaffected by changes in both lateral placement and width of

the supraglottal duct in the parallel duct case. There was a maximum variation of only 1.02% in
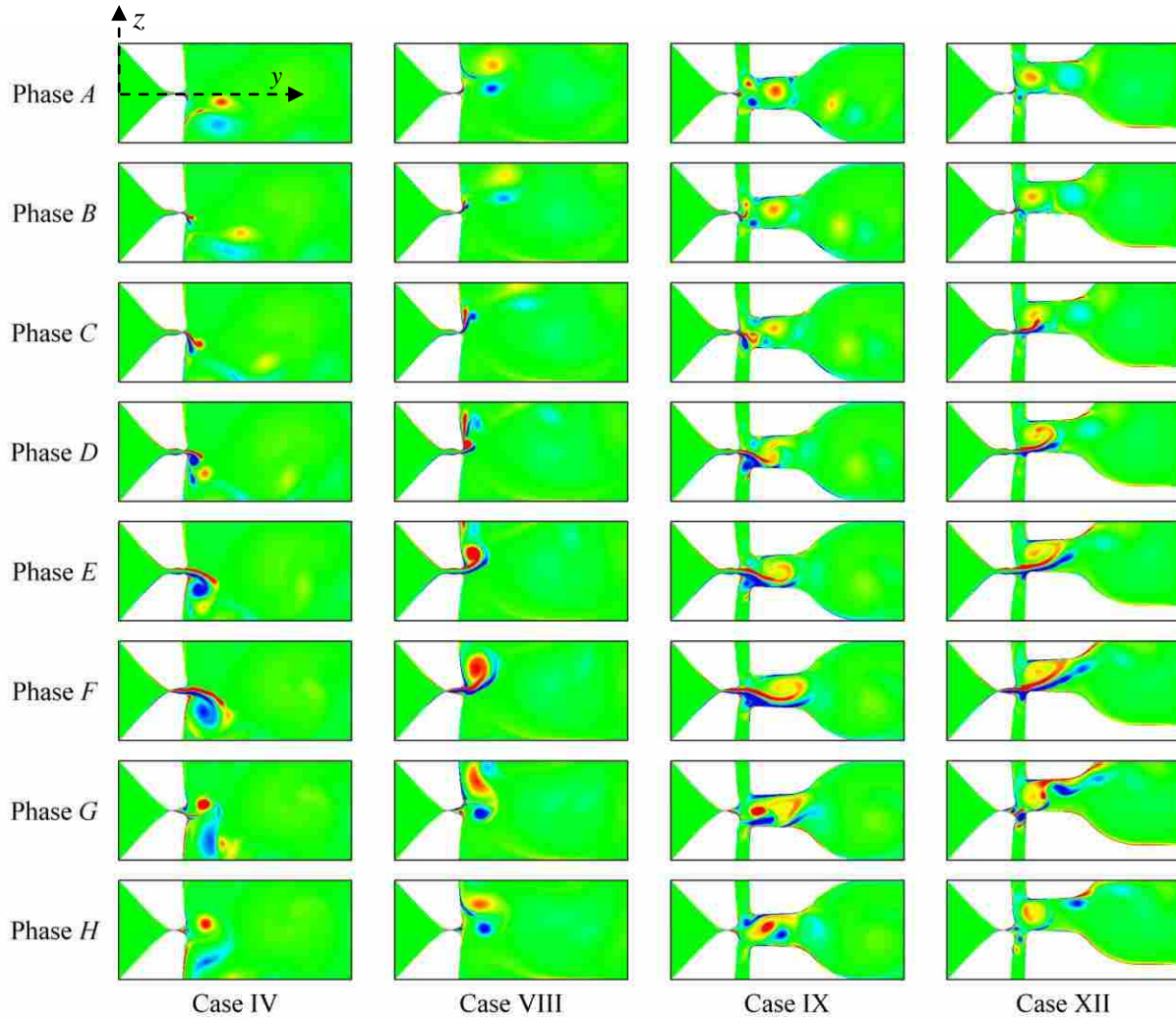
Figure 2.16: *x*-vorticity of the glottal jet at each phase for cases IV, VIII, IX, and XII.

Q_{max} and 1.03% in Q_{avg} for cases I-VIII. Additionally, the offset of the supraglottal duct with FVFs present had a small effect on flow rate where the largest offset of 2.6 mm (case XII) produced a decrease in Q_{max} and Q_{avg} from the symmetrically placed model of 2.65% and 2.86%, respectively.

Including FVFs did create an appreciable change in flow rate, with an 8.20% increase in Q_{max} and 7.44% increase in Q_{avg}. This trend was similar to that reported by Zheng et al. (2009) who reported 47.4% and 21% increases in Q_{max} and Q_{avg} respectively when FVFs were included.

The difference in magnitude of increased flow rate was likely due in part to the higher driving pressure used by Zheng et al. (2009), which amplifies the flow rate and possibly the resulting effect of the FVFs. Also the distinct vocal fold motion exhibited by this model could alter the effects of the FVFs. It is also possible that the effect of adding FVFs was diminished by the transition from a consistent asymmetric jet to an inconsistent jet.

2.3.4 Glottal Jet

The glottal jet was characterized by examining vorticity contours. The x-vorticity highlights the jet edges, making the jet trajectory clear. As can be seen in Fig. 2.16, which depicts the x-vorticity for each of eight phases of a typical cycle from several cases (IV, VIII, IX, and XII), the glottal jet was generally not symmetric. The jet trajectory varied from case to case. The general pattern seen in case IV was typical for most of the parallel supraglottal cases; however, in some cases the jet deflected to the other direction (for example in Fig. 2.16 case VIII is nearly identical to case IV but the trajectory is mirrored about the y-axis). When FVFs were included the jet trajectory changed significantly with the FVF surfaces limiting the extent to which the jet could deflect (see Fig. 2.16 cases IX and XII). As reported by Zheng et al. (2011a), the deflection of the jet was likely initiated by recirculation regions just downstream of the glottis; in this case the jet then became attached to one vocal fold surface and remained attached. Because of the lower flow rates at which this model operated, the flow possibly did not separate as readily as it would in cases with higher flow rates.

The degree to which the jet was diverted in the cases without FVFs (at times to the extent that it was attached to the superior surface of one vocal fold) was larger than that reported by several researchers (e.g., Tao et al., 2007; Zheng et al., 2009). However a similar phenomenon

35

was reported by Erath and Plesniak (2010) in a driven model and by Becker et al. (2009) in a synthetic self-oscillating model.

It was also interesting to note that while each case exhibited highly asymmetric jets, the cycle-to-cycle variation in cases without FVFs was very minimal, with the jet seeming to have chosen one side early in the simulation and repeatedly diverting in the same direction (see Fig. 2.17). This is likely a function of several factors, such as a laminar flow solver having been used and the lower flow rates (and consequently lower Re) studied in this paper than in other simulations. Finally the large deflection and lower flow rates of this model led to strong vortices that slowly connected downstream. Due to the specifics of this model, these vortices happened to affect each subsequent jet in the same way, causing consistent cyclic jets. This final reason was consistent with observations of the FVF cases. The two FVF cases with the large offset of the downstream geometry in the lateral direction (cases XI and XII) showed a similar consistent flow
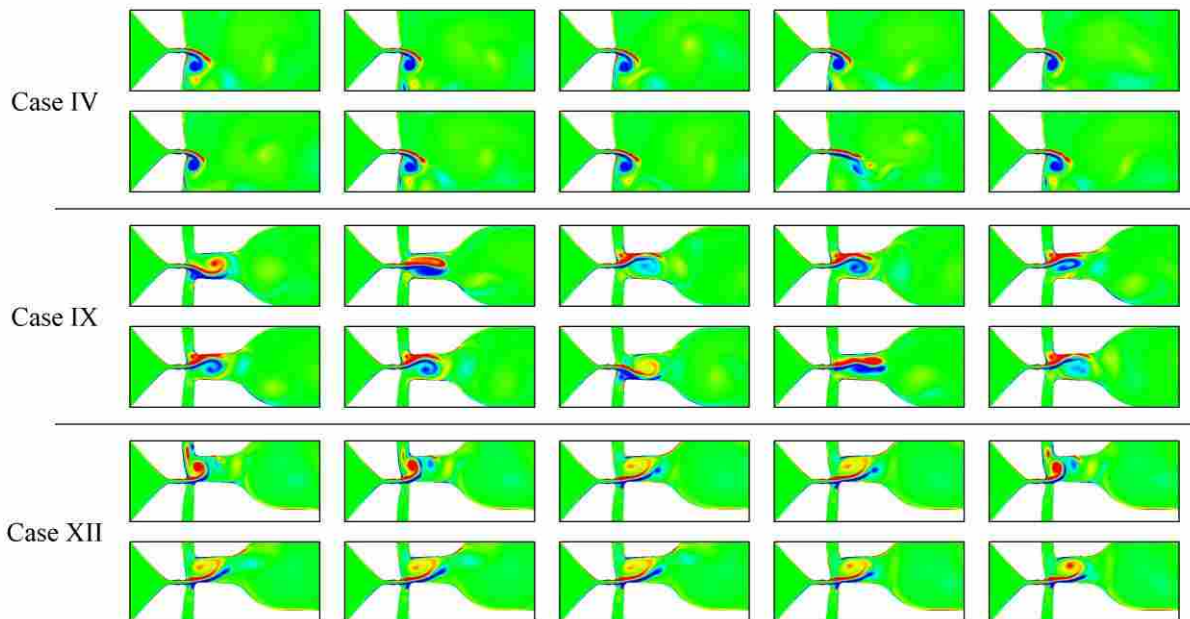
Figure 2.17: *x*-**vorticity for phase *E* of ten cycles for cases IV, IX and XII. Note the nearly consistent jet from one cycle to the next in cases IV and XII and the inconsistent nature of the jet in case IX.**

36

with little cycle-to-cycle variation. In both cases the glottal jet deflected when it encountered the inferior corner of the closer FVF. This large deflection led to a consistent vortex generation that in turn led to repetitive jet deflection (see Fig. 2.17 case IV and XII).

In the other two FVF cases (IX and X), the jets were not consistent from one cycle to the next. In these cases the jet inconsistently attached to one FVF or the other, and at other times would persist nearly symmetric through the FVF gap (see Fig 2.17) just as reported by other researchers (Zheng et al,. 2009). In these cases the jet did not deflect to the extremes as in other cases. Even though the jet was visibly attached to the medial surface of one vocal fold, it exited the glottis with very little deflection. The jet did deflect slightly farther down stream as it entered the FVF gap. It therefore appears that large jet deflections led to a more stable repetitive flow structure that was self preserving, while jets with little deflection were unstable and exhibited inconsistent cycle-to-cycle variation in flow structures.

The jets of these computational studies were similar to those observed in a self-oscillating synthetic model used by Drechsel and Thomson (2008). First, little cycle-to-cycle variation was seen in most of those cases. Secondly, in both studies, for most of the cases with an offset parallel supraglottal duct, the jet initially skewed toward the closer wall, and later in the cycle somewhat straightened out. One exception to this in the present study was in the extreme offset case (VIII) where the jet was instead deflected towards the farther wall. Drechsel and Thomson (2008) saw a similar phenomenon at one pressure (1.25 kPa). Furthermore, in cases with FVFs in both studies, the jet was initially skewed away from the closer FVF; it later straitened out to a degree and was then deflected again away from the near FVF (see Fig. 2.16, case XII). This was the observed jet behavior in cases XI and XII of the present study where there was substantial offset in the lateral position of the downstream duct. In cases IX and X of the present study

37

where the supraglottal geometry was nearly (case X) or perfectly (case IX) symmetric, the jet exited the glottis in a straight manner and then deflected towards and attached to one FVF or the other near the center of the FVFs in the superior inferior direction. Farther downstream it again separated from the FVF and deflected back towards the centerline (see Fig. 2.16, case IX).

One significant difference between this study and that of Drechsel and Thomson (2008) is that the jet in the present study deflected drastically. It remained attached to one vocal fold until the superior surface during the very initial parts of the cycle. This again was attributed to the presence of a strong mucosal wave in this model that was not present in that of Drechsel and Thomson (2008), as well as lower driving pressure of this model (Drechsel and Thomson ,2008, used 1.25 to 1.9 kPa). Additionally, the jet in the present study is two-dimensional; the jet in the study of Drechsel and Thomson (2008) was three-dimensional. Because the two-dimensional model did not include any dissipation related to flow motion in the third dimension, it likely allowed the more deflected jet to persist, while in a three-dimensional model the jet may not deflect to such extremes.

2.3.5   Intraglottal Pressure Distributions

Thomson et al. (2005) showed that the time varying pressure along the vocal fold surface in conjunction with the vocal fold motion is critical in determining the rate at which energy is transferred to the vocal fold. In the present study, two vocal folds were present and, due to asymmetries in the flow, had distinct pressure profiles. Therefore knowing what the pressure profiles were along each vocal fold can lead to insights in possible asymmetric energy transfer.

Pressure data were extracted from along both vocal fold surfaces at the eight phases A-H per cycle for ten cycles. The pressure profiles for several cases and phases can be seen in Figs. 2.18 through 2.21. Note that Figs. 2.18 and 2.19 show data for phases from a single cycle, while Fig. 2.20 shows the pressures at one phase for ten cycles. In Fig. 2.21 the data are ensemble-averaged and left and right vocal fold data were averaged together. Each figure is discussed in more detail below. In each case the pressure profile had a minimum at the location of minimum glottal width which corresponded to the highest velocity at that location. Different phases had a different magnitude of minimum pressure, with phase *F* exhibiting the largest negative pressure which was as the glottis was closing. As the cross sectional area decreased, the velocity increased and pressure decreased. At subsequent phases the glottis was closed and therefore
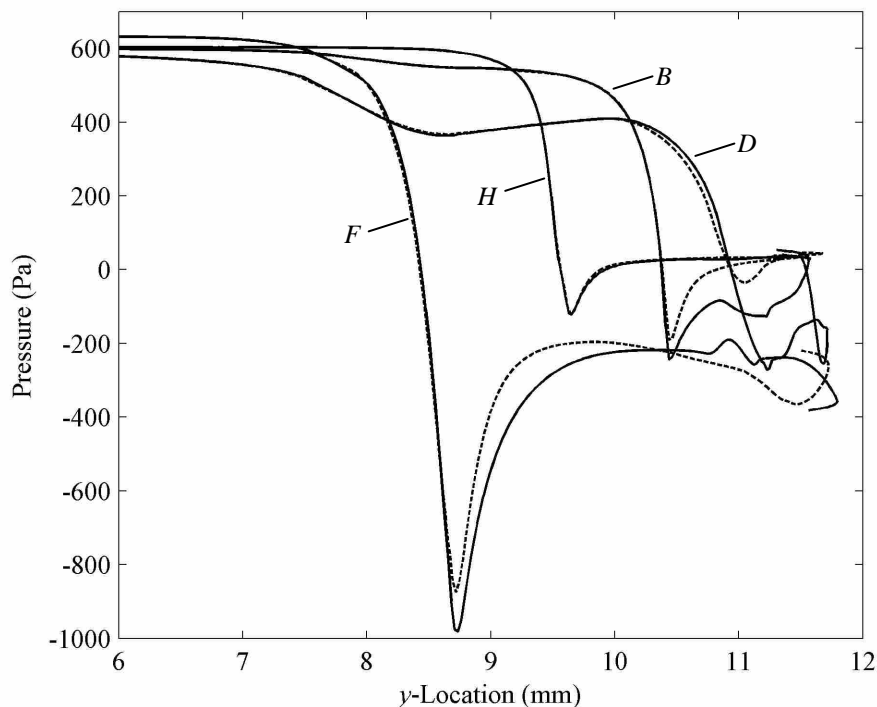
Figure 2.18: Typical pressure profiles for every other phase (*B*, *D*, *F*, and *H*) of case V. Note that in this case the jet separates first from the left vocal fold surface (dashed line) and therefore recovers to a higher pressure before the right vocal fold (solid line). Also, the minimum pressure is seen in phase *F* where the vocal folds are in the process of closing.

blocked the flow, which led to lower velocities and higher pressure; therefore, the peak minimum pressure in phases *G* and *H* was higher (less negative) than that of phase *F*. As the glottis opened once again (phase *A*) the flow was allowed to accelerate and the pressure again dropped, thus phase *A* had a lower peak pressure than that of *H*. In phases *B-D* the glottis widened, the velocity dropped, and the pressure rose. At phase *E* the glottis was parallel and there was a local minimum at the first narrowing of the glottis and another at the second narrowing, with relatively the same pressure. Between these two local minima the pressures were higher (see Figs. 2.18 and 2.19). This trait is expected as the air slowed when as it flowed into the wider portion of the glottis and then sped back up as it entered the second constriction.
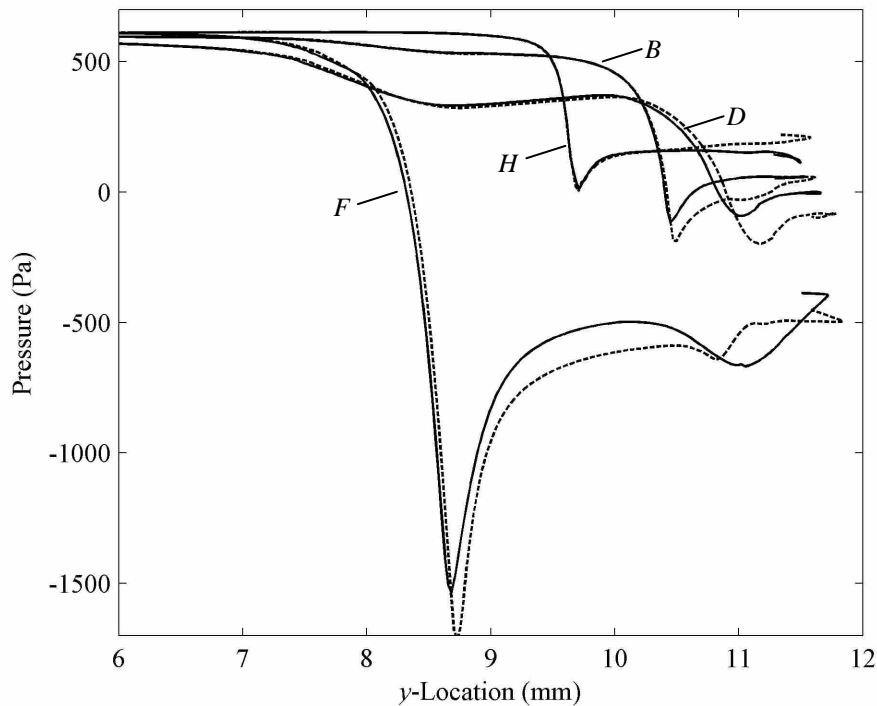
Figure 2.19: Typical pressure profiles for every other phase (*B*, *D*, *F*, and *H*) of case IX. Note that for this cycle the jet separates first from the right vocal fold surface (solid line) and therefore recovers to a higher pressure before the left vocal fold (dashed line). Also, the minimum pressure is seen in phase *F* where the vocal folds are in the process of closing.

40
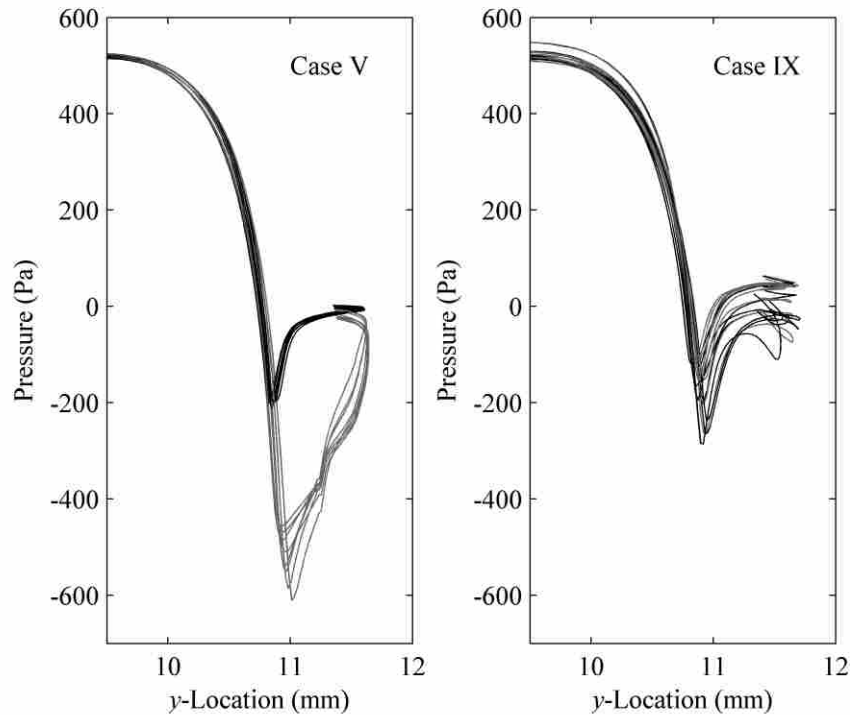
Figure 2.20: Pressure profiles for phase *C* of ten cycles of cases V and IX including the left (black) and right (gray) vocal fold pressure profiles. Note the consistent asymmetric behavior in case V and the inconsistent more symmetric behavior in case IX.

In the cases where consistent jet deflection was more prevalent (cases I-VII, XI, and XII), the pressure was distinct from one vocal fold surface to the other, yet the pressure was nearly identical from one cycle to the next (see Fig. 2.20). Both vocal folds had nearly identical pressure profiles from the inferior edge until the location of the minimum glottal width, where the pressure was a minimum. The pressure profiles remained relatively similar until the jet separated from one vocal fold surface; here the fold to which the jet remained attached maintained a lower pressure until its separation point (see Figs. 2.18 and 2.19). The largest pressure differences were seen near the superior surfaces, but both pressures eventually recovered to the same downstream pressure of 0.0 Pa. In cases IX and X, where the jet inconsistently varied from one cycle to the next, the pressures along opposing vocal folds were

41

less distinguishable, with more closely symmetric pressure profiles in a single cycle and the left and right profiles switching when the jet deflected in the opposite direction.

The pressure profiles for the various cases were altered in the presence of various supraglottal geometries. For cases I through V with various supraglottal widths, there was little variation between the pressure profiles with a slightly lower peak pressure for the case with the smallest supraglottal width (case I) and increased minimum pressure with wider ducts. Besides this small difference, cases I through V were essentially identical in their pressure profiles. Also, when comparing the medial-lateral placement of the downstream duct (cases V-VIII) there was essentially no significant difference.

The most obvious difference among cases I-VIII was found in cases I and VIII where the jet deflected toward the left vocal fold instead of the right as it did in cases II-VII. Here the left pressure profile matched the right pressure profile of the other cases and the opposite was true
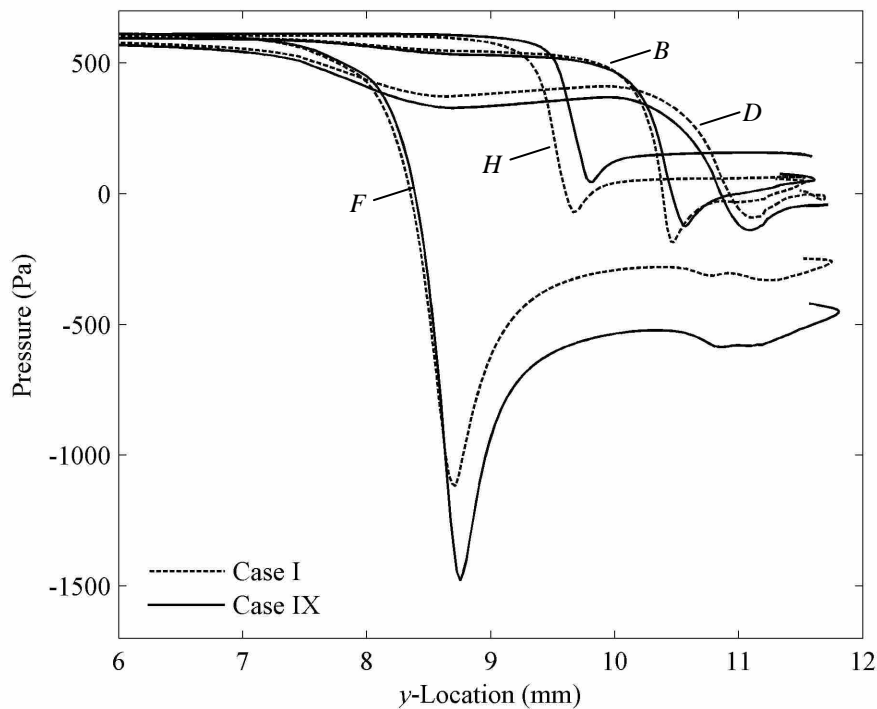
Figure 2.21: Average pressure profiles for phases *B*, *D*, *F*, and *H* of cases I and IX. Data were ensemble-averaged and left and right vocal fold data were averaged together.

42

for the right pressure profile. This led to the conclusion that for a parallel supraglottal duct in the range of widths and offsets studied, and the given driving pressure, the main contributor to the pressure profile of a given vocal fold was the direction in which the jet deflected. This however, was likely only the case because a consistent supraglottal jet was present. An inconsistent jet may have revealed additional effects of supraglottal position or width not presently seen.

The addition of FVFs however, did have a significant impact on the pressure profiles. In comparing case IX to case I, there was a pronounced difference (see Fig. 2.21). The pressures in phase F were essentially 300 Pa lower with FVFs than without (20% of the local minimum for the FVF case). Similar trends were seen in phases G, A, D, and E with an opposite effect in phases H and C with pressure profiles being nearly identical in phase B. These trends were seen in the recovery pressure as well. It was therefore likely that the recovery pressure was equal to the pressure between the FVFs and the true vocal folds and it drove the pressure magnitudes within the glottis. Additionally the higher flow rates (see Table 2.3) in case IX than in case I led to the lower glottal pressures.

Comparing the offset cases with FVFs present (cases IX-XII) was more difficult; the variations in the jet for these cases caused significant scatter in the pressure data. However there was a recognizable increase in the pressure within the glottis as the supraglottal geometry was increasingly offset. This was likely due to the fact that the FVFs essentially blocked the glottal jet and therefore reduced its velocity and increased the pressure within the ventricles and glottis.

The characteristics of the pressure profiles led to some interesting observations. First, in all cases the pressure profiles were nearly symmetric except for along the superior surfaces. Because the pressure on the superior surface acts mainly in the inferior direction, it may contribute to the asymmetries between vocal folds in the y-direction. Also, the cases with the

most (albeit small) asymmetric motion (cases IX and X) had inconsistent yet more symmetric pressure profiles than the cases where the motion was highly symmetric (cases I-VII, XI, and XII) but that had pressure profiles that were consistent and asymmetric. This led to the conclusion mentioned previously that asymmetric motion of the vocal folds was not due solely to asymmetric loading but rather to asymmetric loading with cycle-to-cycle variations. Obviously some asymmetry in the loading was necessary for asymmetric motion to develop. It is possible that the asymmetry of the vocal fold motion developed first and led to an inconsistent jet and pressure profiles, which in turn amplified the asymmetry in the vocal fold motion; however, Zheng et al. (2011a), using a symmetric driven computational model, found that downstream vortices were primarily responsible for jet deflection. A similar result was observed from the first two cycles of motion in the current study. Therefore the jet deflection may have been initiated downstream of the glottis and led to inconsistent loading on the vocal fold surfaces, which in turn caused the small observed asymmetries in motion.
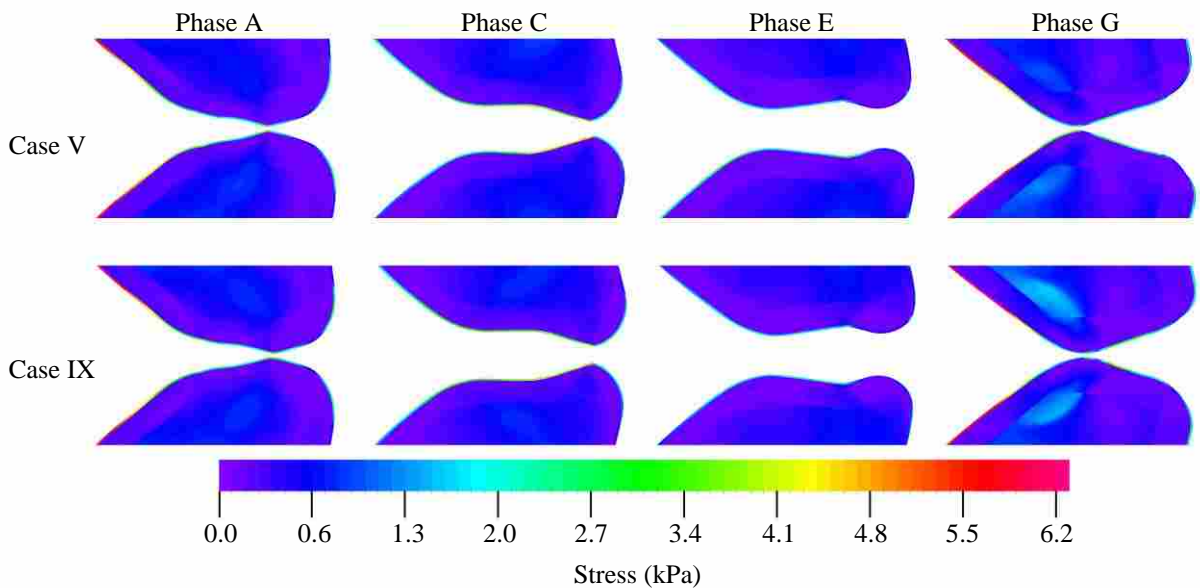
Figure 2.22: Effective stress in the vocal fold models at several phases of cases V and IX.

44

In an attempt to further understand why the asymmetric pressure profiles did not lead to significant asymmetry in the vocal fold motion, the stresses within the vocal folds for several phases were analyzed (see Fig. 2.22). As can be seen, there was a significantly higher stress in the epithelium layer than in the other layers. This stress was mainly due to the large deformation of this layer coupled with its high stiffness. The cover layer had a very low stress (approximately zero kPa) at every phase. It is possible that the large stresses present in the epithelium layers tended to dominate and the relatively small asymmetric loading on the vocal fold surfaces did not yield significant stress variations. While the stress contours in Fig. 2.22 lead to some new insights in the vocal fold behavior, they are only preliminary and future investigation in this area is needed.

2.3.6   Separation Point Location

Using vorticity plots, the separation points along the upper and lower vocal fold were estimated (see Fig. 2.23). In each case, one side of the jet separated just downstream of the
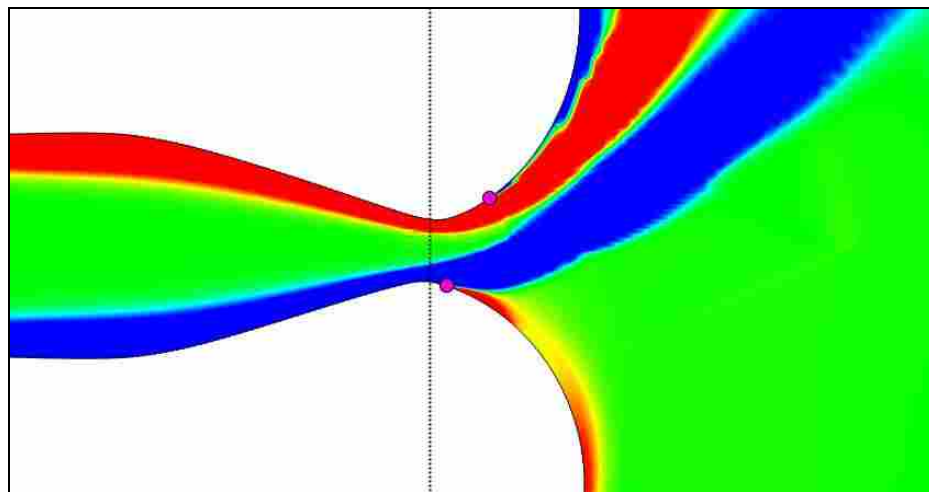
Figure 2.23: Sample of separation points taken by visually inspecting the edge of the jet from vorticity plots. The pink dots represent the chosen separation points from the given vorticity plot. The dotted line represents the *y*-location of G_{min}

minimum glottal area, as has been reported by other authors (Alipor and Scherer, 2004; Decker and Thomson, 2005). However, in most cases the other side of the jet remained attached to the other vocal fold and separated much further downstream. On the vocal fold from which the jet separated further upstream, the *y*-location of the separation point followed a consistent and well behaved curve throughout the cycle just downstream of the location of minimum glottal width (see Fig. 2.24). The other separation point was much less stable, with its location jumping upstream and downstream inconsistently. This is in part due to some instabilities in the jet arising from adverse pressure gradients. The side to which the jet remained attached was linked to the jet deflection direction and was therefore consistent in all cases except cases IX-XI.
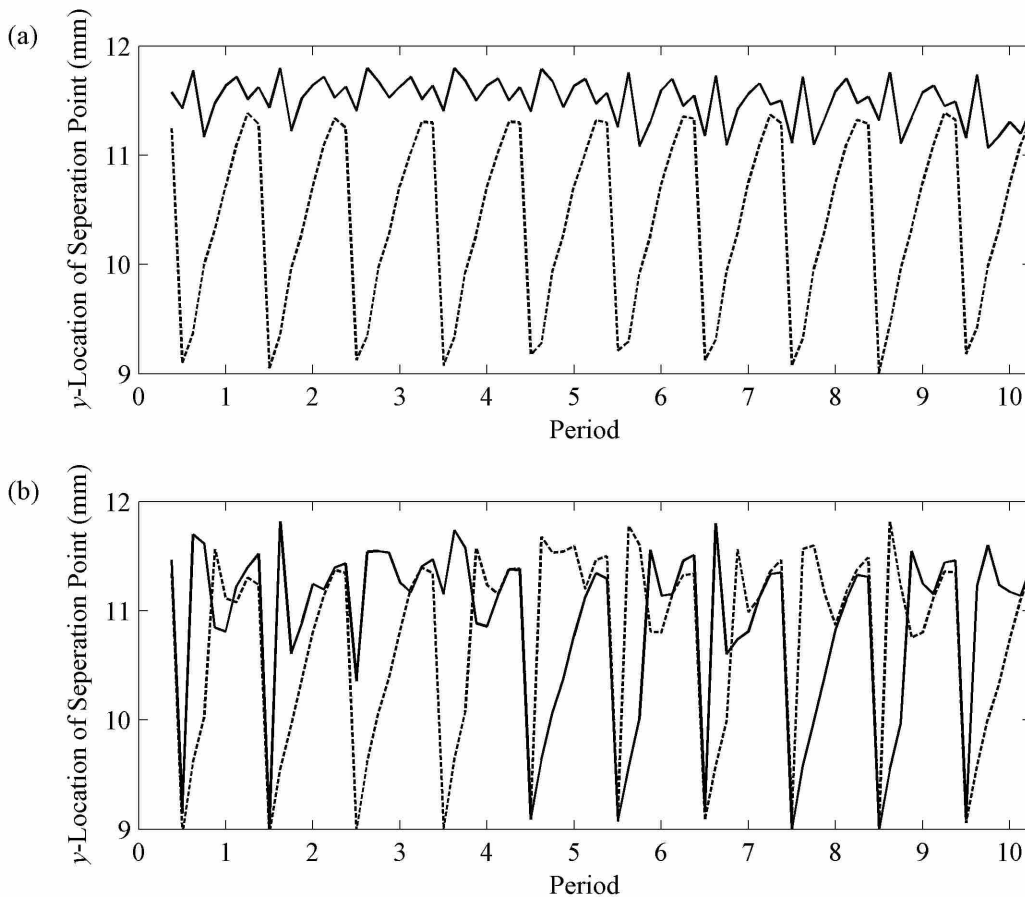
Figure 2.24: Separation point location for case IV (a) and case X (b). The solid and dashed lines are for the right and left vocal folds respectively. The discrete nature of the plots is due to the fact that data are only taken at eight phases per cycle.

46

In most cases the side of the jet that remained attached did not separate until near the superior surface of the vocal fold. In a few cases, the flow separated from both vocal folds at nearly the same y-location for some phases and then became reattached further downstream, with a second separation point near the glottis exit. In these cases the furthest downstream separation point was used in determining the y-location of separation. When both sides separated at the same y-location and remained separated, the jet remained nearly symmetric throughout the glottis; however, this was only observed in cases I, VII, and IX-XII, and then only for a few of the phases. The increased jet symmetry in cases IX-XII can be attributed to the FVFs which helped to maintain the jet along the centerline. In case I, the narrower supraglottal duct may have been responsible for this added symmetry. It is unclear why case VII had increased symmetry.

2.4   Conclusions

In this study a two-dimensional computational model of the vocal folds coupled with a laminar, incompressible, unsteady Navier-Stokes solver was used to study the flow-induced vibrations of phonation. The vocal fold had four layers, including an epithelium and very soft lamina propria. The airway was loaded with a constant 600 Pa pressure difference from inlet to outlet and resulted in frequency, flow rate, amplitude, and motion qualities comparable to those of human phonation. The model was verified through grid and time step independence studies. The peak flow rate in the smaller time step size case was 8.4% lower than in the case with the normal time step size; however, this was deemed acceptable when compared with the added computational costs.

Various supraglottal geometric configurations were modeled in order to better understand their influence on vocal fold vibrations and glottal jet characteristics. Many of the cases resulted in highly asymmetric glottal jets with relatively consistent cycle-to-cycle trajectories. It is

believed that the low driving pressure and pronounced mucosal wave of the model caused the more consistent jet deflection than has been reported in some other computational (Lou et al., 2009; Zheng et al., 2009, 2011a) and experimental (Becker et al., 2009; Erath and Plesniak, 2010) models.

The centered FVF cases exhibited the highest degree of variation from one cycle to the next and the highest degree of asymmetry in vocal fold motion, despite the fact that the magnitude of asymmetry in the glottal jet was significantly lower than the cases where the jet was more consistent from one cycle to the next. It was hypothesized that the asymmetry of motion in the vocal folds was influenced more by the inconsistency of the glottal jet than by its asymmetry.

No significant changes in the vocal fold motion, glottal jet, or pressure profiles were seen in the parallel supraglottal cases (V-VIII) by offsetting the supraglottal geometry. The flow tended to be relatively consistent. A more unstable flow may have been more heavily influenced by asymmetries in supraglottal geometry. This was observed in the cases with FVFs (IX-XII), where the flow had significant cycle-to-cycle variations in the symmetrically placed supraglottal duct. However, with large offsets in this duct's positioning, the flow was forced to deflect in a way that made it consistent from one cycle to the next, even with FVFs present. While the jet in the most extreme offset FVF case (XII) was more asymmetric than that of the symmetrically placed case (IX), it was also consistent and therefore led to reduced inter-cycle variation in other measured parameters.

Widening the supraglottal airway in the range studied (cases I-V) also had little, if any, effect on flow rates, jet trajectory, and vocal fold motion. It did however slightly increase the pressure throughout the glottis. The addition of FVFs decreased the pressure throughout the

glottis for the majority of the phases but had the opposite effect in two phases and no change for another phase.

The greatest effect of the supraglottal geometry was to influence jet stability, with more stable jets leading to more consistent and symmetric motion in the vocal folds. Jet stability can be affected in several ways. First, by changing glottal width, which was essentially the case with the addition of FVFs, an otherwise stable flow (in case I) was caused to become unstable (case IX). Also extreme lateral placement of supraglottal geometry (case XII) caused an unstable flow (case IX) to become stable.

To summarize, while changing the supraglottal geometry in the manner described here had a significant effect on the supraglottal jet characteristics, doing so had relatively little effect on vocal fold vibration. This suggests that the supraglottal jet may not play a significant, direct role in governing vocal fold vibration; however, further computational and experimental studies should be performed to verify this.

3   EFFECT OF MODELING CHOICES ON THE FLOW-INDUCED RESPONSE OF A COMPUTATIONAL VOCAL FOLD MODEL

In the previous chapter a computational model of the larynx was used to study the influence of supraglottal geometry. The focus of this chapter is on the effects of various computational assumptions and modeling choices on model response. While many of these assumptions and choices have been used previously, no systematic study of these factors has been performed. The goal of this study is to seek to clarify the importance and influence of these factors on predicted model response.

3.1   Introduction

Computational modeling requires many decisions and assumptions to be made. Computational modeling of the human vocal folds is no exception. Many of the decisions can potentially alter the simulation output, and consequently, its usefulness and validity.

3.1.1   Contact Lines

One motivation behind many vocal fold modeling choices is the need for well-behaved mesh movement throughout the simulation. Typically the vocal folds collide during the adduction phase of the cycle (e.g., Gunter et al., 2005). This collision temporarily closes the glottis, which in turn temporarily stops airflow. This collision is easy to simulate in a physical model, but much more difficult in a computational model. Computational models use finite elements or control volumes to model the air within the glottis. These control volumes must

maintain a non-zero volume in order for the solution to progress. In standard control volume computational fluid dynamics (CFD) with movable boundaries, the control volumes are distorted as the walls move. Within the glottis, the control volumes must compress in the medial-lateral direction as the folds adduct. Complete glottal closure would reduce these volumes to zero and cause the solver to fail. Even as the elements are increasingly compressed in this dimension, mesh distortion can result in numerical instability, solver failure, and/or solution inaccuracy.

Complete glottal closure can also cause difficulties in non-conforming mesh approaches, such as the immersed boundary method. In this method the boundary of the solid model is overlaid onto a non-deforming Cartesian grid representing the fluid domain. The fluid velocities in elements which are within the boundary of the solid domain are forced to be zero while those outside of the solid domain remain as variables. A given element is affected depending on its position relative to the boundary during the current time step. As the vocal folds come together, an increasing number of elements are covered by the solid domain and "turned off," resulting in increasingly fewer active elements within the glottis. This becomes problematic when the glottal gap is at or below the size of a single cell in this location because no flow will be present even when there is a small glottal gap.

In both conventional control volume and immersed boundary method simulations, issues arising from complete glottal closure have been avoided in the past with the use of a contact line (2D) or plane (3D) (e.g., Luo et al., 2008; Pickup and Thomson, 2011). The contact line acts as a barrier through which the solid domain cannot pass. This restricts the movement of the edge of the vocal fold such that it is not permitted to close beyond a specified point. The collapsing fluid mesh is allowed to occupy a small space that never completely collapses in the control volume method. In the immersed boundary method model, this space is reserved for elements which will

never be "turned off." In this approach the collision between folds is no longer represented directly but instead is represented by collisions between the folds and the contact lines.

Provided that the gap maintained by the contact lines is sufficiently large, the model will continue to function; however new difficulties are introduced. With contact lines in place, the minimum glottal gap is forced to maintain a value greater than zero and some flow leakage past the vocal folds is present. In order to reduce the minimum glottal width and minimize flow leakage, the contact line is placed for as small of a glottal gap as practically possible. Another potential problem arises with the use of contact lines in a model containing both vocal folds. Because the collision between vocal folds is approximated with two distinct collisions between the folds and their respective contact lines, folds which are out of phase with one another could artificially collide at different times. This would indeed be a significant shortcoming; however, it is often not an issue as healthy vocal folds normally vibrate very closely in phase with one another, even under highly asymmetric flow conditions (see section 2.3.2).

While the practice of including contact lines is often used, specific attention has not been given to its effect on the model. Many researchers have not reported any method used to prevent collapse of the mesh (their models may not fully close due to the flow and geometry of the vocal folds alone, or they may neglect to report the method used) (e.g., Alipour and Scherer, 2000). Others mention using a contact line but give no specific emphasis (e.g., Thomson et al., 2005). Those who discuss its use give a short explanation as to its necessity, the contact line location, and possibly the methods used to implement the contact condition and collision model; however, they do not justify the distance chosen (e.g., Luo et al., 2008, 2009; Pickup and Thomson, 2011). There is therefore a need to better understand how the contact line location affects the model

response. In this chapter, the influences of contact line location on vocal fold motion, pressure along the vocal fold surface, flow rate, and glottal jet are explored.

3.1.2   Material Properties

Another consideration of importance in computational vocal fold modeling is the choice of material properties. Due to the large variability in measured tissue properties, researchers will often choose a value within a given range that produces reasonable results. This is useful in producing a general model that can be used for further studies, but there is still some question as to the validity of the choice. Computational models are often used in conjunction with synthetic or excised larynx models to better understand the larynx in general. The material properties and geometries of a synthetic vocal fold can be well known; however, those of actual larynges are much more difficult to obtain. In addition, the material properties of a synthetic model are limited by the materials available and cannot exactly match those of an actual larynx. One such case is in the use of silicone for synthetic models. The Young's modulus of the material can be altered over a wide range by the addition of thinner to the compound before it cures. This allows for models with Young's moduli that approach those measured in human tissue. However, the Poisson's ratio (ν) of silicone is not necessarily the same as that of human tissue, and cannot generally be controlled.

Poisson's ratio, which is related to the compressibility of a material, is a measure of the strain in one direction relative to an applied strain in an orthogonal direction. Human tissue is generally considered to be incompressible at phonation frequencies (Berry and Titze, 1996; Titze and Story, 2002). Depending on the material modeling assumptions, this corresponds to various Poisson's ratios. In an isotropic material (one in which properties have no directional

dependence), a Poisson's ratio of 0.5 would correspond to incompressibility. This is the upper limit of Poisson's ratio in an isotropic material due to thermodynamic laws (Lempriere, 1968). However, vocal fold tissue is anisotropic and may exhibit different Poisson's ratios depending on the orientation of the tissue. One way to model tissue anisotropy is to use a transversely isotropic material (one which has unique properties in the longitudinal, or anterior-posterior, direction, and no directional dependence in the transverse plane). If the longitudinal Poisson's ratio (ν') in this type of material is equal to zero, the transverse Poisson's ratio (ν) in the transverse direction can be greater than 0.5, with a limiting value of 1.0 in the incompressible case. The difference in Poisson's ratios corresponding to incompressibility for these two model types demonstrates that comparison of Poisson's ratio alone between the models is insufficient.

Despite the claim that vocal fold tissue is incompressible, computational vocal fold models have often been defined using Poisson's ratios that are lower than the corresponding incompressible value, and in different models, various Poisson's ratios have been used. For example Thomson et al. (2005), Luo et al. (2009), and Smith (2011), each using an isotropic material, used Poisson's ratios of 0.45, 0.3, and 0.49 respectively. Tao and Jiang (2006, 2007) and Zheng et al. (2011b) used a transversely isotropic material model. Both models had a longitudinal Poisson's ratio of zero, while the former used a transverse Poisson's ratio of 0.3 and the latter used 0.9. Luo et al. (2008) and Rosa et al. (2003) each used a transversely isotropic material that had $\nu' = \nu$. Luo et al. used $\nu = 0.3$, while Rosa et al. (2003) used various Poisson's ratios for the different layers ranging from 0.45 to 0.76. The various Poisson's ratios used led to a question of how model response is affected by the choice of ν. In this chapter, the influence of various Poisson's ratios on a given isotropic model is explored.

3.1.3 Symmetry

Another significant factor influencing computational modeling decisions is computational cost. Because the simulations generally take a considerable amount of time to process and post-process, the models are simplified as much as possible. Various parameters can be altered to reduce computational costs, such as grid density and time step size. Other factors also play a role in computational cost, including turbulent vs. laminar flow modeling, compressibility, two-dimensional vs. three-dimensional model definition, and small vs. large deflection.

In computational vocal fold modeling, one simplification that has been followed has been to assume symmetric vocal fold motion. Generally, the geometry of a real larynx is reasonably (although not perfectly) symmetric, and when creating models, be they synthetic, analytical, or computational, researchers often model it as symmetrically as possible (e.g., Jiang et al., 2001; Suh and Frankel, 2008; Zheng et al., 2010). In computational simulations researchers often employ symmetry assumptions for computational efficiency. This can be done by modeling only one half of the larynx and enforcing a symmetry boundary condition. This essentially cuts computational costs in half because only one half of the larynx is modeled. This approach to modeling has often been taken (e.g., Zhao et al., 2002; Thomson et al., 2005); however, it has been found that the jet exiting the glottis is often asymmetric, diverting to one side or the other in the supraglottal region (e.g., Triep et al., 2005; Tao et al., 2007; Erath and Plesniak, 2010; Zheng et al., 2010). It is therefore important to quantify what effects the symmetry choice has on the computational model. In the past, researchers have used both half-models with symmetry assumptions, as well as full geometrically-symmetric models where asymmetry of flow and motion is allowed to develop (Tao et al., 2007; Luo et al., 2009; Zheng et al., 2010); however, the effects of symmetry assumptions on overall model response have not been quantified. In this chapter, the symmetry assumption is explored.

To summarize, the choices and assumptions specific to a computational model can greatly influence the model's response and accuracy. This research explored the influence of multiple modeling choices including contact line location, Poisson's ratio, and geometrically symmetric vs. an enforced symmetry boundary. The effects of these modeling decisions on vocal fold vibration, glottal width, flow rate, pressure profiles, and glottal jet are discussed in the following sections. Suggestions regarding modeling choices that can be reasonably expected to give accurate results are given.

3.2 Numerical Methods

As in Chapter 2, ADINA was used to simulate the flow-induced vibration of a two-dimensional vocal fold model.

3.2.1 Fluid Domain

The fluid domain of this study was similar to that of the symmetric parallel case of Chapter 2 with several alterations. In all cases but one, only one half of the larynx was modeled and a symmetry condition was imposed on the medial line at $z = 0$ mm (see Fig. 3.1). This symmetry condition permitted a y-component (superior direction) of velocity but no z-component (lateral direction). The supraglottal width for these cases was 18.9 mm, thus the half models had a 9.45 mm wide duct. All cases were designed to be initially symmetric, i.e., no supraglottal offset was used. Within the glottis, several leader-follower points were used which constrained the y-displacement of the follower points along the symmetry line to match the y-displacement of the leader points on the vocal fold surface as it moved. This helped control mesh movement. Case S did not use a symmetry line or leader-follower points; instead, the airway was mirrored about the center line creating a full, initially-symmetric model. Leader-follower points
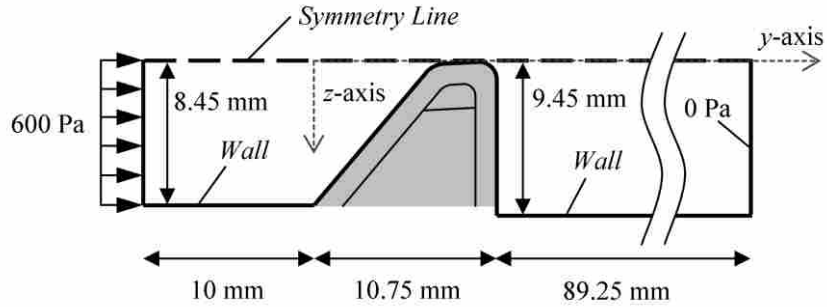
Figure 3.1: Airway geometry and boundary conditions.

were not necessary in this case because both folds moved in a similar manner, thereby maintaining a reasonably controlled mesh. The properties of the air used in this study were identical to those in Chapter 2 with a density and viscosity of 1.2 kg/m^3 and 1.8×10^{-5} Pa·s, respectively.

3.2.2 Solid Domain

The solid domain consisted of a single four layer vocal fold, identical to that described in Section 2.2.2 (see Fig. 2.3); although in several cases the contact line was not in the same location as it was in Chapter 2. A parameter was used that describes the minimum permitted glottal width (G_{min}). In each case the distance between the symmetry line and the contact line, G_C, was one half of G_{min} (see Fig. 3.2). For example, in a case with $G_{min} = 50$ µm, the contact line was located at $z = 25$ µm (see coordinate system in Fig 3.1). For reference, the medial surface of the vocal fold was initially at $z = 50$ µm. In all cases except those used to specifically study Poisson's ratio, the Poisson's ratio was 0.49 in each layer of the solid. In the Poisson's ratio study, the Poisson's ratio varied from case to case but was the same throughout each vocal fold model of a given case. Further details of the contact and Poisson's ratio cases can be found in
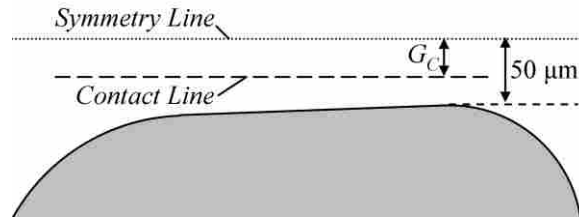
Figure 3.2: Contact line location (not to scale).

Section 3.2.4. The symmetric case was unique in that two identical mirrored vocal folds were used. In this case the contact lines were located at $z = \pm 25$ μm.

3.2.3 Verification and Validation

The same mesh density and time step size used in the models of Chapter 2 were used in the present studies. This led to a fluid domain with 33900 quadrilateral control volumes (for a half model) and solid domain with 50036 elements (for one vocal fold). Each case ran for a total simulated time of 0.25 s, at which point the vocal fold had been oscillating at a near steady-state condition for about 0.15 seconds. In one exception, the Poisson's ratio case with $\nu = 0.4$ failed to solve beyond $t = 0.05$ s, at which point it was close, but had not yet reached, steady-state vibrations. The last complete period of this case was used in the analysis. These simulations required approximately 120 processor hours per simulation on the Brigham Young University Fulton Supercomputing hardware (Dell PowerEdge M610 equipped with dual, quad-core, 2.8 GHz Intel Nehalem processors and 24 GB of memory; simulations each ran on four cores of a single processor).

3.2.4 Case Studies

In this chapter several different cases were used to study the various parameters of interest. They are listed in Table 3.1. There were eight cases focusing on the effect of contact line location and were labeled with the letter C with the value of G_{min} (in μm) as a subscript. For example, case C_{50} was the contact line case where $G_{min} = 50$ μm. Twelve cases with ν ranging from 0.4 to 0.49999 were used to study the effects of ν on vocal fold motion and flow characteristics. These cases were labeled with the letter P with a subscript of the value of ν for the given case. For example, case $P_{0.495}$ was the Poisson's ratio case where $\nu = 0.495$. Note that case C_{50} was identical to case $P_{0.49}$. One additional case was used to study the differences

Table 3.1: Geometric parameters for each case.

Case	Symmetry assumption	Contact line location, G_C (μm)	Poisson's ratio
C_1	Assumed symmetry	0.5	0.49
C_3	Assumed symmetry	1.5	0.49
C_5	Assumed symmetry	2.5	0.49
C_7	Assumed symmetry	3.5	0.49
C_{10}	Assumed symmetry	5	0.49
C_{20}	Assumed symmetry	10	0.49
C_{30}	Assumed symmetry	15	0.49
C_{50}	Assumed symmetry	25	0.49
$P_{0.4}$	Assumed symmetry	25	0.4
$P_{0.43}$	Assumed symmetry	25	0.43
$P_{0.46}$	Assumed symmetry	25	0.46
$P_{0.48}$	Assumed symmetry	25	0.48
$P_{0.485}$	Assumed symmetry	25	0.485
$P_{0.4875}$	Assumed symmetry	25	0.4875
$P_{0.49}$	Assumed symmetry	25	0.49
$P_{0.4925}$	Assumed symmetry	25	0.4925
$P_{0.495}$	Assumed symmetry	25	0.495
$P_{0.499}$	Assumed symmetry	25	0.499
$P_{0.4995}$	Assumed symmetry	25	0.4995
$P_{0.49999}$	Assumed symmetry	25	0.49999
S	Symmetric geometry	25	0.49

between a full model with initially symmetric geometry and a half model with a symmetry assumption. This case was labeled as case S and was defined using the same parameters for G_C and ν as case C_{50}. Throughout this chapter, the model in case C_{50} where the geometry was modeled for only half of the larynx and the other half was treated with the symmetry assumption is referred to as a "half model," while the model of case S where both halves of the larynx were modeled is referred to as a "full model."

3.3   Results and Discussion

3.3.1   Contact Line

The location of the contact line affected several aspects of the model. The contact line directly limited the vocal fold displacement as it approached the symmetry line; this directly altered the glottal waveform and vocal fold motion. These alterations in turn led to variations in other areas of the model. Some of the areas affected included the volumetric flow rate (Q) waveform, intraglottal pressures, and the characteristics of the glottal jet. These effects are discussed in this section.

The glottal waveform was used to calculate the average and maximum glottal widths (G_{avg} and G_{max}), as well as the open quotient (O_q), and the fundamental frequency (F_0) of the model (see Section 2.2.5 for definitions of these variables).

As can be seen in Figs. 3.3 and 3.4, there were minimal differences in the glottal waveforms predicted by the models with different contact line locations. The largest difference was in G_{min}. As mentioned above, G_{min} in each case was directly determined by G_C. As expected,
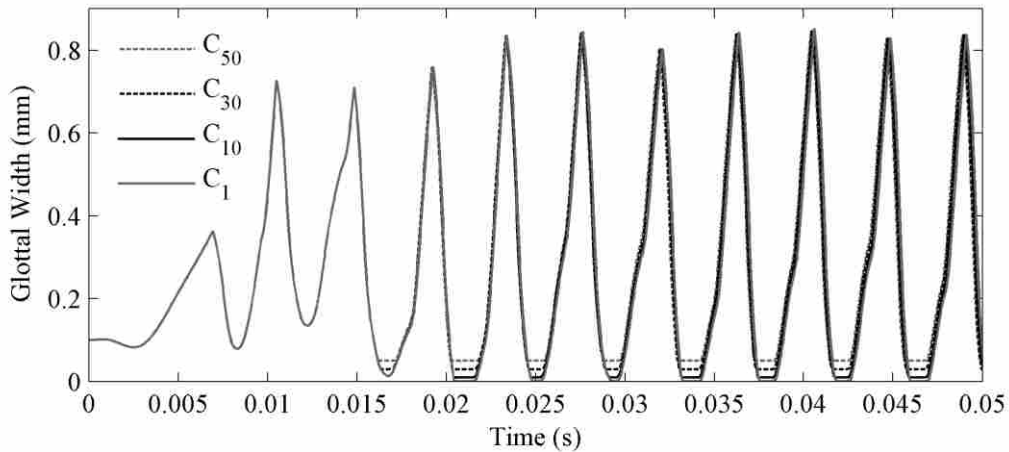
Figure 3.3: Glottal width over the first 0.05 seconds of simulated time for several contact line cases.
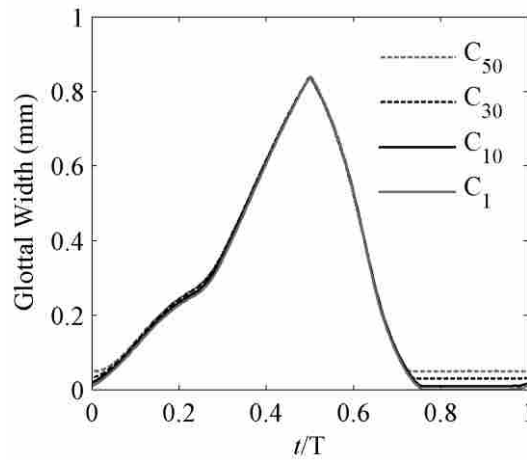
Figure 3.4: Glottal width vs. normalized time for one cycle of several contact line cases.

distinct values of G_{min} were observed for each contact line case. However, the glottal width for the remaining portions of the cycle was largely unaltered by variations in G_{min}. As seen in Table 3.2, the maximum change in G_{max} between the eight contact plane cases was only 3.1 μm, or about 0.36%. In addition, G_{avg} increased by 19.9 μm (6.8%) from case C_1 to case C_{50} with a nearly linear relationship between G_{min} and G_{avg}. F_0 of each model was relatively unaltered by contact line location, with only a 0.47% change in frequency over all of the cases.

The general shape of the vocal fold profile during vibration was also relatively unaffected by G_{min} (see Fig. 3.5). The only substantial difference in the profiles of various cases was seen during contact. The medial surfaces were slightly different because each case was permitted to extend toward the medial line to a different degree depending on the contact line location. However, the medial surface on either side of the region in contact was largely unaffected. The consistency across models was further evidenced by the path plots of points RI and RS (defined in Section 2.2.5) (see Fig 3.6). The paths of both points were very similar for all cases with a maximum deviation of approximately 0.01 mm.

Table 3.2: Measured values of frequency (F_0), maximum glottal width (G_{max}), average glottal width (G_{avg}), open quotient (O_q), wave velocity (V_W), maximum flow rate (Q_{max}), and average flow rate (Q_{avg}).

Case	F_0 (Hz)	G_{max} (mm)	G_{avg} (mm)	O_q	V_W (m/s)	Q_{max} (ml/s)	Q_{avg} (ml/s)
C_1	235.6	0.839	0.273	0.795	0.830	363.6	129.0
C_3	236.0	0.839	0.275	0.789	0.827	363.5	129.7
C_5	236.0	0.839	0.276	0.789	0.827	363.6	130.1
C_7	236.1	0.839	0.277	0.788	0.827	363.6	129.2
C_{10}	236.1	0.839	0.278	0.776	0.833	363.6	129.7
C_{20}	236.4	0.838	0.283	0.765	0.834	363.8	131.3
C_{30}	236.7	0.836	0.286	0.753	0.833	363.8	132.8
C_{50}	236.5	0.836	0.293	0.718	0.831	363.9	135.8
$P_{0.4}$	275.9	1.151	0.433	0.828	1.053	512.0	209.3
$P_{0.43}$	256.9	1.011	0.353	0.783	1.051	451.3	164.8
$P_{0.46}$	243.0	1.001	0.341	0.771	0.963	428.7	158.8
$P_{0.48}$	248.6	0.970	0.310	0.660	0.897	419.6	140.7
$P_{0.485}$	243.6	0.883	0.297	0.691	0.894	379.1	137.1
$P_{0.4875}$	240.7	0.858	0.295	0.689	0.876	373.1	136.8
$P_{0.49}$	236.5	0.836	0.293	0.718	0.831	363.9	135.8
$P_{0.4925}$	231.7	0.788	0.286	0.747	0.776	338.9	133.7
$P_{0.495}$	225.5	0.734	0.277	0.787	0.711	316.6	129.4
$P_{0.499}$	83.0	0.617	0.290	1.000	0.174	240.8	132.5
$P_{0.4995}$	83.7	0.460	0.298	1.000	0.093	158.0	137.0
$P_{0.49999}$	0	0.279	0.279	1.000	0.000	126.2	126.2
S	237.4	0.837	0.297	0.741	0.850	367.8	137.2
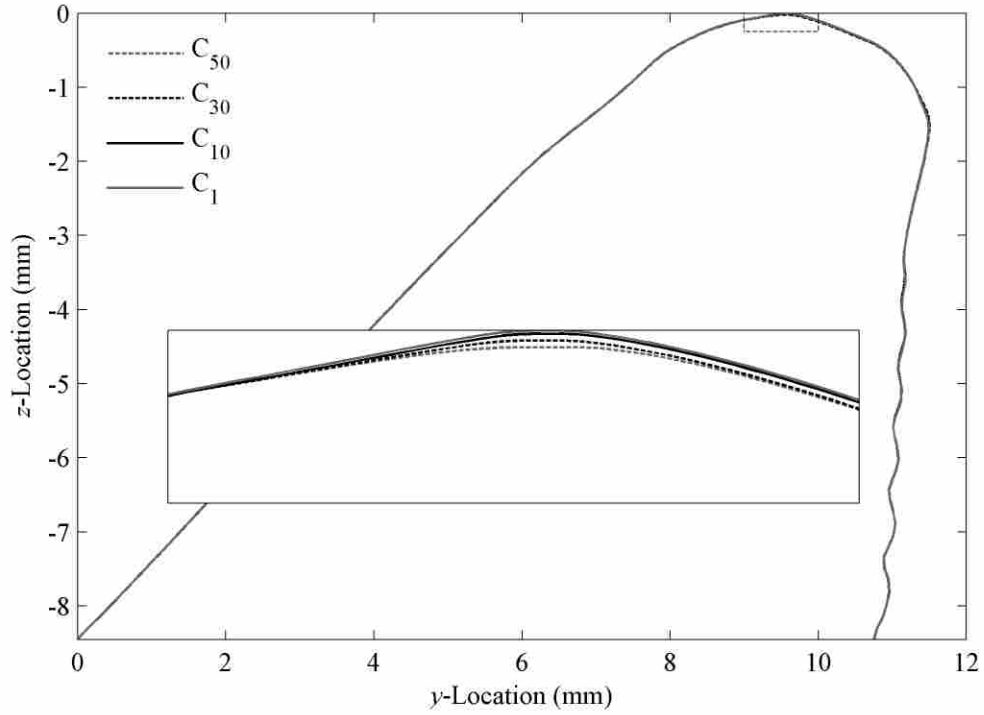
Figure 3.5: Outline of the vocal folds at one phase for several contact cases. The dashed box outlines the location of the inlaid close-up view.
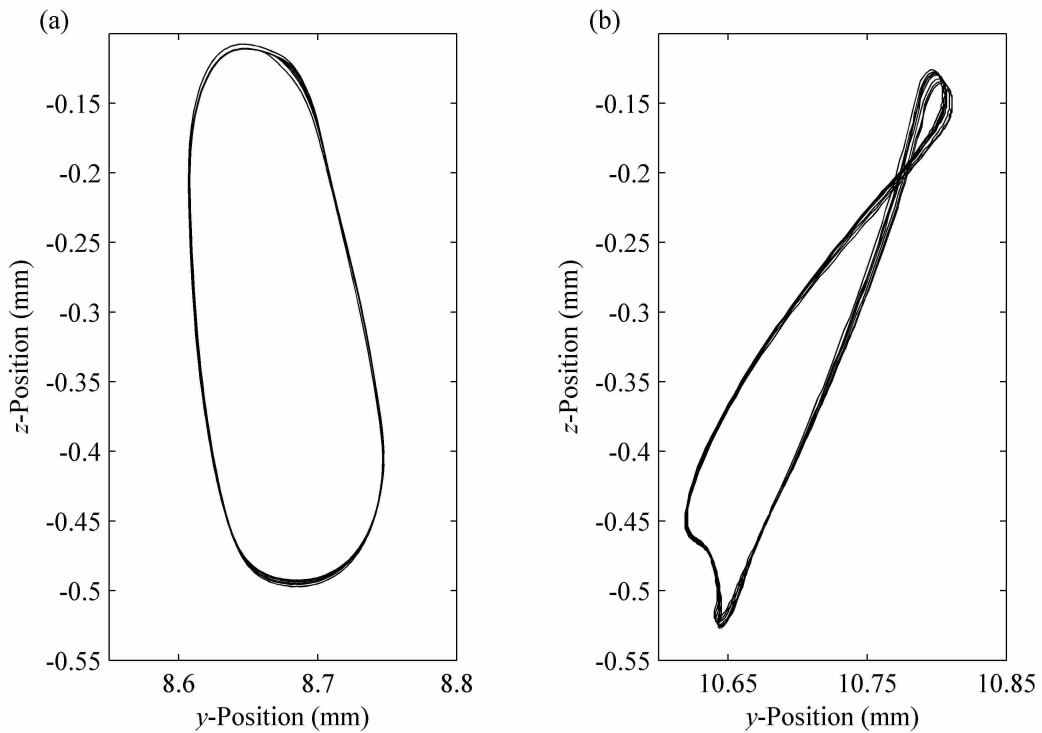
Figure 3.6: Superimposed motion of *RI* (a) and *RS* (b) points of cases C_1 through C_{50} over a single cycle.

The wave velocity (V_W) was also calculated for each of the cases in the same manner as in Chapter 2. There was very little variation in V_W with various contact line locations (a maximum of 0.0073 m/s or 0.88%).

The slight variations in glottal width for the contact line cases led to similar changes in the flow rate waveforms (see Fig. 3.7). The portions of the cycle and the degree to which the flow rate was affected were essentially the same as seen in the glottal width waveforms. There was a slightly higher flow rate during the closed portion of the cycle (about 15 ml/s) for case C_{50} than C_1. This was due to the less complete closure of the glottis in case C_{50}. Because the glottis could not fully close, a small amount of air was allowed to "leak" past. However, for smaller G_{min}, less flow was permitted to leak. The maximum variations in Q_{max} and Q_{avg} were only 0.43 ml/s (0.12%) and 6.74 ml/s (4.96%), respectively, and were fairly linear with G_{min} (see Table 3.2).
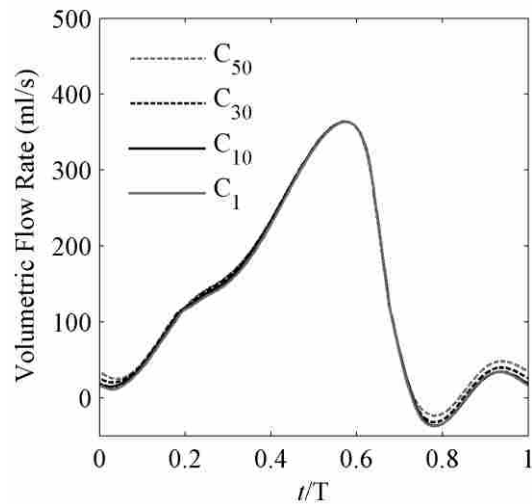
Figure 3.7: Volumetric flow rate vs. normalized time for several of the contact line cases.

An interesting phenomenon was observed in the pressure data for the various contact line cases. In theory, with a completely closed glottis, and an incompressible medium, the pressure on the upstream side of the contact location will be very close to that of the inlet pressure and the pressure on the downstream side of the contact will be at the exit pressure. However, because the glottis could not fully close in the present simulation, as air accelerated beyond the point of minimum glottal width, it caused a localized low pressure region. The more completely the glottis closed, the less air flowed past and the sharper the transition from the inlet to the outlet pressure. This is what was expected in the results from these models during the closed portion of the cycle; however, additional features were seen. In case C_{50} the minimum pressure peak was pronounced but also fairly smooth, as expected (see Fig. 3.8). As G_{min} was reduced, the general path of the curve became closer to the expected step discontinuity in upstream and downstream pressures (see Fig 3.8(c) and (d)). However, for cases with G_{min} smaller than 20 μm, the curve began to exhibit spurious pressure fluctuations, with the most severe case being C_1 (see Fig. 3.8(c) and (d)).

The observed pressure fluctuations were very ordered, with adjoining nodes alternating in pressure increase or decrease and the maximum fluctuations occurring at the location of contact. In one phase (not shown) of case C_1 this pressure fluctuation had a magnitude of approximately 700 Pa. It is assumed that these large pressure fluctuations arose from numerical instabilities occurring when the control volumes were significantly compressed and had high aspect ratios. It also appeared that filtering the pressure data could remove positional frequencies smaller than the size of a single control volume, thereby removing the noise while allowing a more realistic pressure profile to remain. However, the exact effect of the spurious pressures on the rest of the system is unclear. The pressure profiles more than 1 mm upstream or downstream of the
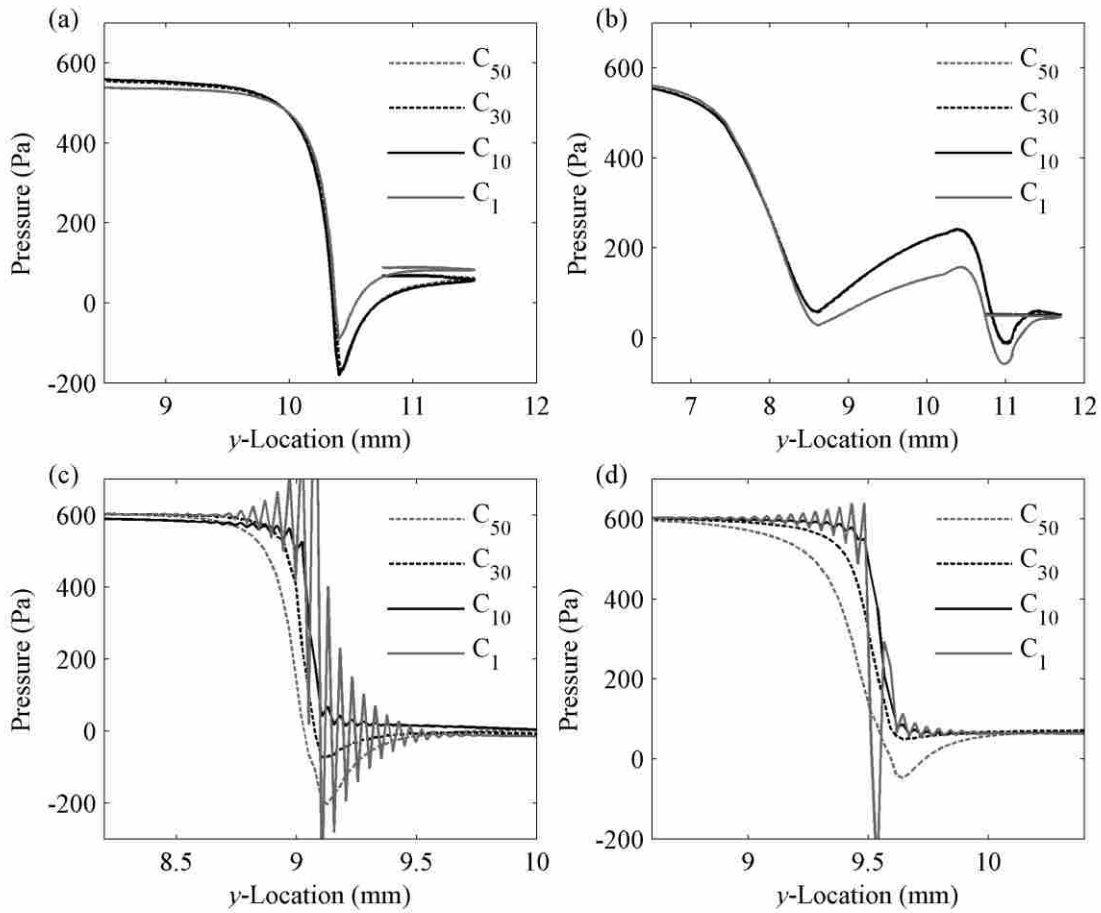
Figure 3.8: Pressure profiles for several contact line cases at phases *B* (a), *E* (b), *G* (c), and *H* (d) (see Fig. 2.7 for phase definitions). Phase *B* is just after the glottis has opened, phase *E* is when the glottis is at its maximum width, phase *G* is when the glottis first closes, and phase *H* is in the middle of the closed portion of the cycle. Note in plots (a) and (b) the pressure profiles for C_{50}, C_{30}, and C_{10} are directly over one another

constriction do not appear to contain significant spurious pressure fluctuations. This is consistent with the assumption that the fluctuations arose from the highly compressed control volumes, since the control volumes further than about 1 mm from the point of contact were not compressed past their initial width.

Another interesting phenomenon was seen in the pressure profiles for case C_1 in phases where the glottis was open. In all cases of the closed phases the pressure profiles seemed to converge to the same step waveform, with sharper corners the smaller the G_{min}. In addition, cases

67

C_3 through C_{50} had essentially the same pressure profiles for each open phase, suggesting that the contact plane location made no difference in the open phase pressure profiles. However, during the open phase, case C_1 had a different pressure profile, with variations in pressure from the other cases of up to 100 Pa (see Fig. 3.8(a) and (b)). It was assumed that the numerical instability during the closed portion of the cycle caused the distinct pressure profiles seen in case C_1, causing it to be less accurate. It is unclear how the different pressure profiles arose without significantly affecting the glottal width, flow rate, or vocal fold outlines.

As can be seen in Fig. 3.9, there was some change in the intraglottal flow as contact line location was altered. Plotting the maximum velocity within the glottis over time (Fig. 3.10) shows a steady decrease in the velocity with decreasing G_{min} during the closed portion of the cycle for cases C_7 through C_{50}. Case C_{50} had a minimum leakage velocity of 23.1 m/s while that of case C_7 was only 1.63 m/s. These were 43.7 and 3.1%, respectively, of the maximum velocity during the cycle. Plotting the minimum leakage velocity for each case vs. G_{min} (Fig. 3.11) shows
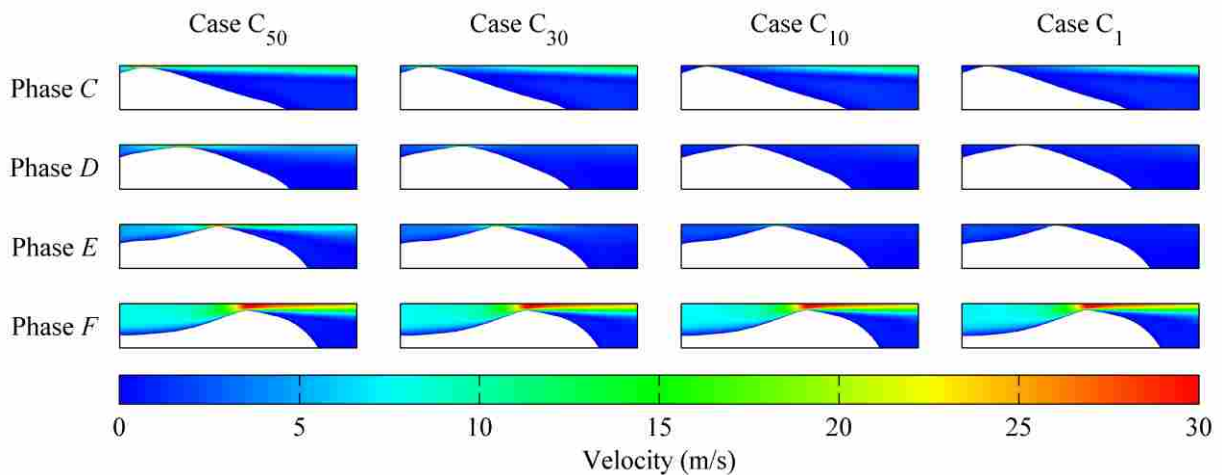
Figure 3.9: Velocity plots of four phases of several contact line cases. Phase *C* is when the glottis first closes and phase *F* is the first phase after the glottis opens.

68
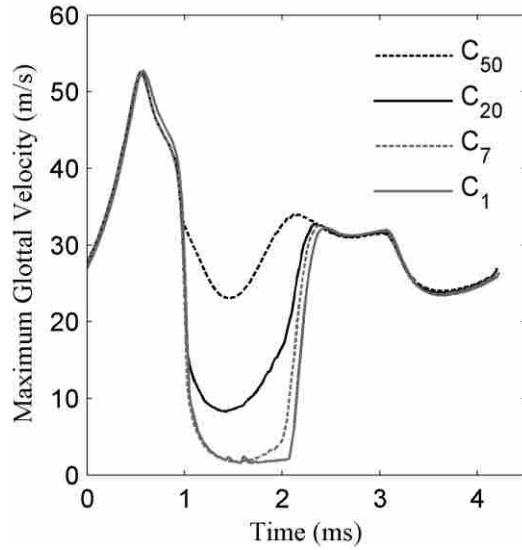
Figure 3.10: Maximum glottal velocity over time.
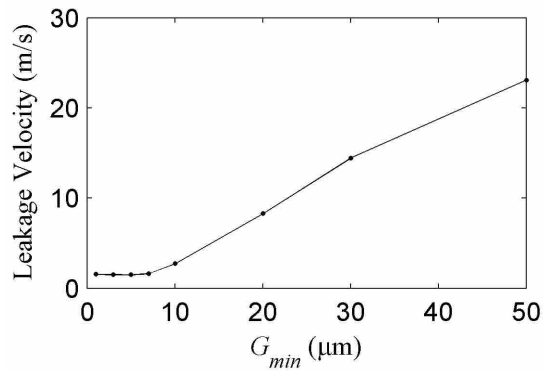
Figure 3.11: Leakage velocity vs. minimum glottal width.

a nearly linear relation between the two for $G_{min} > 7$ μm. Below $G_{min} = 7$ μm, the leakage velocity was essentially unchanged.

By analyzing the trends of important values as G_{min} approaches zero, one can now estimate the suitable value of G_{min}. For most studies (using this solid model and driving pressure) a contact line corresponding to a G_{min} of 50 μm was sufficient. The resulting G_{avg}, O_q, and Q_{avg} using this contact location were within 10%, and the F_0, G_{max}, V_W, and Q_{max} results were within 1%. The glottal width and flow rate waveforms were all very similar. In addition, for case C_{50} the

69

elements were able to collapse within the glottal gap without introducing the spurious pressure profiles seen for smaller G_{min}. The most significant deviation seen from case C_{50} was in the pressure profiles within the glottis during the closed portion of the cycle. Here, a decrease in minimum pressure was seen due to the flow leakage. However, these pressure discrepancies were only around 100 to 200 Pa and acted on a very small area for a brief period of time and the overall vocal fold motion appeared to be unaffected. If higher accuracy is desired in closed glottis pressure profile predictions, as well as in other reported values, a G_{min} of 10 μm can be used without introducing significant fluctuations in the pressure data. Using this G_{min} value increased the consistency of all measured values to within approximately 1% of the C_1 results. In addition, larger G_{min} values are preferred from a computational standpoint because they are less prone to solver failure due to mesh movement problems.

3.3.2   Isotropic vs. Transversely Isotropic Models

In this section, the governing equations for stress strain relationships in a continuum model of the vocal folds are presented. They are developed for isotropic and transversely isotropic materials: two types which are commonly used in vocal fold modeling. They are given here as a basis for equations that are developed in the following section.

In computational modeling of the vocal folds, two main material types have been used; isotropic and transversely isotropic. The material is oriented so that for both isotropic and transversely isotropic materials, the properties in the coronal plane are not directionally dependent. The axis with unique properties in the transversely isotropic model is in the anterior-posterior direction. Often the plane strain assumption is made for both model types (e.g., Alipour et al., 2000; Cook et al., 2008; Zhang, 2009), which forces the motion in the anterior-posterior

direction to be zero. Different models have accomplished this in different ways (e.g., Thomson et al., 2005; Cook and Mongeau, 2007) and are discussed in more detail in Cook et al. (2008).

One way to compare the isotropic and transversely isotropic models is through their compliance matrices. The compliance matrix $[C]$ is used in the three-dimensional form of Hooke's law to relate stresses and strains. In this case the strain tensor $\{\varepsilon\}$ is equal to the product of $[C]$ and the stress tensor $\{\sigma\}$. In its full form for a transversely isotropic material with the longitudinal axis in the 3-direction, it takes the form

$$
\begin{Bmatrix} \varepsilon_{11} \\ \varepsilon_{22} \\ \varepsilon_{33} \\ \varepsilon_{23} \\ \varepsilon_{31} \\ \varepsilon_{12} \end{Bmatrix} = \begin{bmatrix} \frac{1}{E} & -\frac{\nu}{E} & -\frac{\nu'}{E'} & 0 & 0 & 0 \\ -\frac{\nu}{E} & \frac{1}{E} & -\frac{\nu'}{E'} & 0 & 0 & 0 \\ -\frac{\nu'}{E'} & -\frac{\nu'}{E'} & \frac{1}{E'} & 0 & 0 & 0 \\ 0 & 0 & 0 & \frac{1}{2G'} & 0 & 0 \\ 0 & 0 & 0 & 0 & \frac{1}{2G'} & 0 \\ 0 & 0 & 0 & 0 & 0 & \frac{1+\nu}{E} \end{bmatrix} \begin{Bmatrix} \sigma_{11} \\ \sigma_{22} \\ \sigma_{33} \\ \sigma_{23} \\ \sigma_{31} \\ \sigma_{12} \end{Bmatrix},
\tag{3.1}
$$

where E and ν are the Young's modulus and Poisson's ratio in the transverse direction and E', ν', and G' are the Young's modulus, Poisson's ratio, and shear modulus in the longitudinal direction. This can be degenerated for an isotropic material by setting E' and ν' equal to E and ν respectively. One method for including the assumption of plane strain is to force ε_{13}, ε_{23}, and ε_{33}

to be equal to zero. For a finite G', σ_{13} and σ_{23} are required to be zero as well, and Eq. (3.1)

reduces to

$$
\begin{Bmatrix} \varepsilon_{11} \\ \varepsilon_{22} \\ 0 \\ 0 \\ 0 \\ \varepsilon_{12} \end{Bmatrix} = \begin{bmatrix} \dfrac{1}{E} & -\dfrac{v}{E} & -\dfrac{v'}{E'} & 0 & 0 & 0 \\ -\dfrac{v}{E} & \dfrac{1}{E} & -\dfrac{v'}{E'} & 0 & 0 & 0 \\ -\dfrac{v'}{E'} & -\dfrac{v'}{E'} & \dfrac{1}{E'} & 0 & 0 & 0 \\ 0 & 0 & 0 & \dfrac{1}{2G'} & 0 & 0 \\ 0 & 0 & 0 & 0 & \dfrac{1}{2G'} & 0 \\ 0 & 0 & 0 & 0 & 0 & \dfrac{1+v}{E} \end{bmatrix} \begin{Bmatrix} \sigma_{11} \\ \sigma_{22} \\ \sigma_{33} \\ 0 \\ 0 \\ \sigma_{12} \end{Bmatrix} ,
$$

(3.2)

for the transversely isotropic material, and

$$
\begin{Bmatrix} \varepsilon_{11} \\ \varepsilon_{22} \\ 0 \\ 0 \\ 0 \\ \varepsilon_{12} \end{Bmatrix} = \begin{bmatrix} \dfrac{1}{E} & -\dfrac{v}{E} & -\dfrac{v}{E} & 0 & 0 & 0 \\ -\dfrac{v}{E} & \dfrac{1}{E} & -\dfrac{v}{E} & 0 & 0 & 0 \\ -\dfrac{v}{E} & -\dfrac{v}{E} & \dfrac{1}{E} & 0 & 0 & 0 \\ 0 & 0 & 0 & \dfrac{1+v}{E} & 0 & 0 \\ 0 & 0 & 0 & 0 & \dfrac{1+v}{E} & 0 \\ 0 & 0 & 0 & 0 & 0 & \dfrac{1+v}{E} \end{bmatrix} \begin{Bmatrix} \sigma_{11} \\ \sigma_{22} \\ \sigma_{33} \\ 0 \\ 0 \\ \sigma_{12} \end{Bmatrix} ,
$$

(3.3)

for an isotropic material.

When using transversely isotropic materials several researchers (e.g., Zheng et al., 2010) have assigned $v' = 0$. This reduces Eq. (3.2) to

$$
\begin{Bmatrix} \varepsilon_{11} \\ \varepsilon_{22} \\ 0 \\ 0 \\ 0 \\ \varepsilon_{12} \end{Bmatrix} = \begin{bmatrix} \dfrac{1}{E} & -\dfrac{v}{E} & 0 & 0 & 0 & 0 \\ -\dfrac{v}{E} & \dfrac{1}{E} & 0 & 0 & 0 & 0 \\ 0 & 0 & \dfrac{1}{E'} & 0 & 0 & 0 \\ 0 & 0 & 0 & \dfrac{1}{2G'} & 0 & 0 \\ 0 & 0 & 0 & 0 & \dfrac{1}{2G'} & 0 \\ 0 & 0 & 0 & 0 & 0 & \dfrac{1+v}{E} \end{bmatrix} \begin{Bmatrix} \sigma_{11} \\ \sigma_{22} \\ 0 \\ 0 \\ 0 \\ \sigma_{12} \end{Bmatrix}.
\tag{3.4}
$$

There are several notable distinctions between Eqs. (3.3) and (3.4). Most notably, Eq. (3.4) is independent of σ_{33}. In fact, the plane strain assumption forces $\sigma_{33} = 0$ for a finite E'. In addition, because of the plane strain assumption, E' and G' are no longer significant. This makes the transversely isotropic model with plane strain and $v' = 0$ identical to an isotropic model with plane strain and plane stress assumptions for either a two or three-dimensional material.

It is instructive to note the similarities and differences between the isotropic model (Eq. 3.3) and the transversely isotropic model (Eq. 3.4). Both models assume linear isotropic properties in the plane of simulation. Both models are also constrained by the plane strain assumption which eliminates all motion and strain out of the plane. While neither model has any strain in the 3-direction, the isotropic model will have stress in the 3-direction and the transversely isotropic model will not. This added stress will give added stiffness to a system governed by the isotropic model that would not be present with the transversely isotropic model.

73

3.3.3 Poisson's Ratio

Altering the Poisson's ratio of the solid model in the current study had a significant effect on the vocal fold motion. The lower Poisson's ratios led to higher vibratory amplitudes while the higher Poisson's ratios caused a significant decrease in this amplitude (see Fig. 3.12). Plotting G_{max} and G_{avg} vs. Poisson's ratio (Fig. 3.13) revealed a nearly linear relationship in G_{avg} and v, and a more complex relation between G_{max} and v, where G_{max} was somewhat linear from 0.4 to 0.48 and then rapidly dropped off as v approached 0.5. As can be seen in Figs. 3.14 and 3.15, in
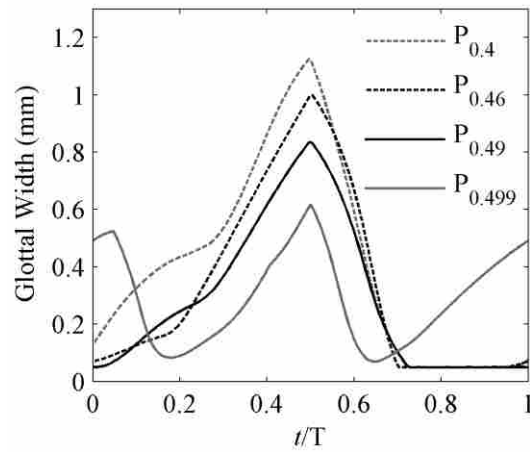
Figure 3.12: Glottal width over normalized time for several of the Poisson's ratio cases.
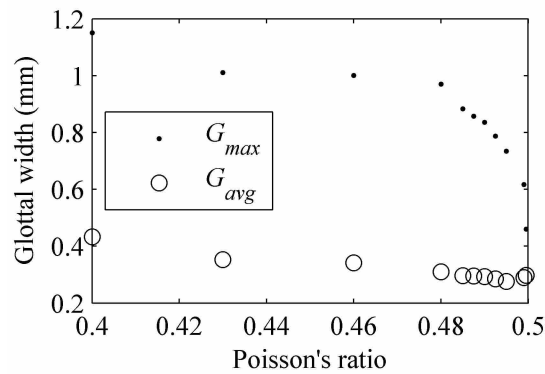
Figure 3.13: G_{avg} and G_{max} for various Poisson's ratios used.

74
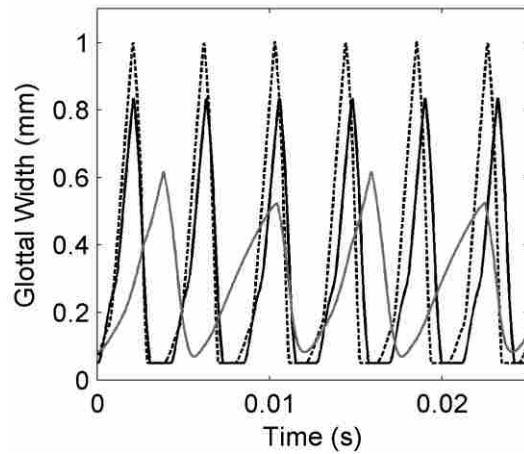
Figure 3.14: Glottal width for several periods of vibration for the Poisson's ratio cases $P_{0.46}$ (---), $P_{0.495}$ (—), and $P_{0.4995}$ (—).
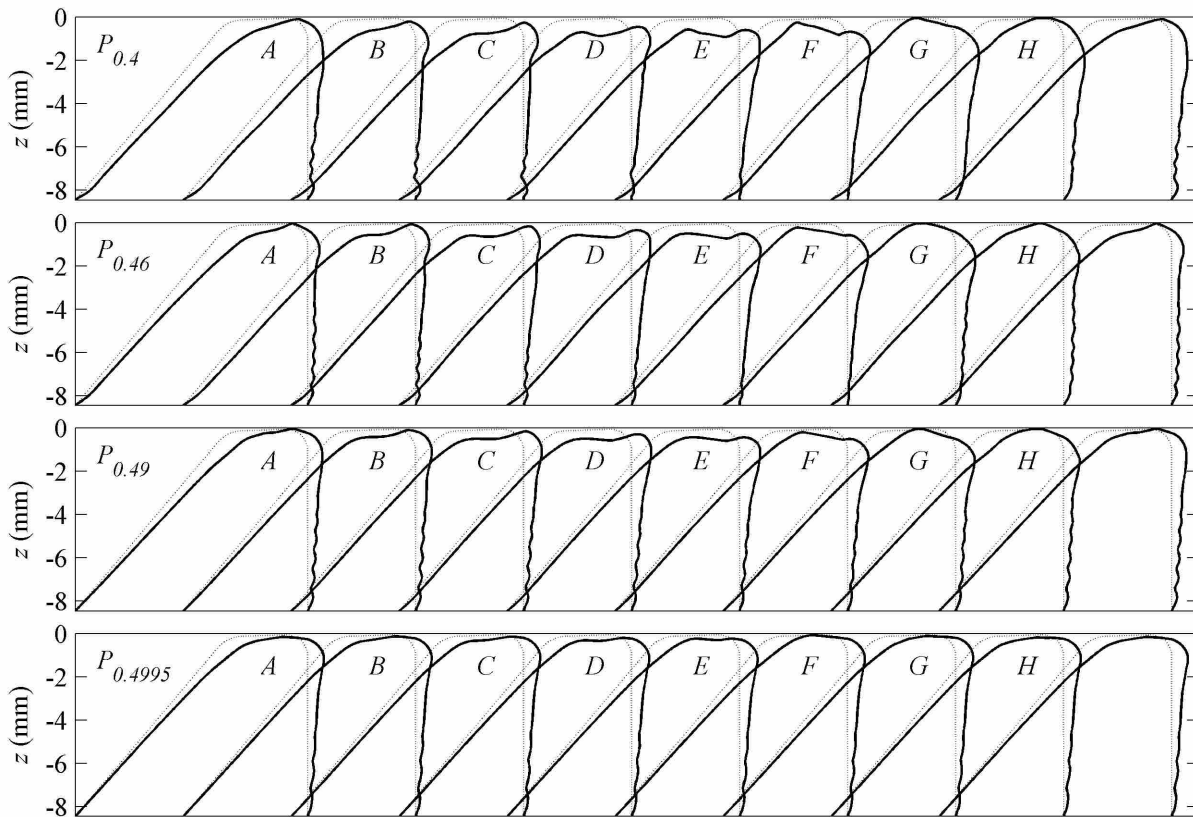
Figure 3.15: Vocal fold profiles at eight phases throughout one cycle for several Poisson's ratios. Phases *A* through *H* are marked for reference. Dotted lines represent original profile.

75

cases with ν above 0.495 the motion was so altered that the vocal fold did not contact the contact line, and therefore had no "closed" portion in the cycle.

In addition to never fully closing, the glottal width waveform for cases $P_{0.499}$ and $P_{0.4995}$ exhibited period doubling, where every other peak in glottal width data became distinct from its neighbors, leading to a new waveform where each complete cycle had two distinct peaks (see Figs. 3.12, 3.14, and 3.15). Increasing ν led to decreased amplitude of vibration until the limiting case where $G_{max} = G_{avg}$ and no vibration was seen. This limit was shown by case $P_{0.49999}$ where the vocal fold opened to a mean displacement and then remained at that position with no subsequent vibration. It is possible that collisions with the contact line helped to maintain the stable nature of the vocal fold motion for cases $P_{0.4}$ to $P_{0.495}$, resulting in a more consistent cycle-to-cycle motion than was seen in the $P_{0.499}$ and $P_{0.4995}$ cases (see Fig. 3.14).

Figure 3.15 shows the outline of the vocal fold in cases $P_{0.4}$, $P_{0.46}$, $P_{0.49}$, and $P_{0.4995}$ at eight different phases throughout the cycle. As can be seen, there is a larger amplitude of motion in both the superior and medial directions for lower Poisson's ratios. The double period nature of case $P_{0.4995}$ can be seen, in addition to distinct differences in vocal fold profiles during oscillation. Cases with higher Poisson's ratios (but below 0.4995) maintained a shape closer to that of the $P_{0.4}$ case.

The fact that the vocal folds stopped vibrating at higher Poisson's ratios is especially interesting considering that vocal fold tissue is generally considered to be incompressible, which would seem to suggest that the ideal Poisson's ratio would be 0.5. Insight into the lack of motion for $\nu \approx 0.5$ can be gained by investigation of relevant equations. Equation (3.3) is oriented to the vocal fold such that the 1-direction is along the inferior-superior axis, the 2-direction in along the

medial-lateral axis and the 3-direction is along the anterior-posterior axis. Solving the third row of Eq. (3.3) for σ_{33} results in

$$\sigma_{33} = \nu\,(\sigma_{11} + \sigma_{22}). \tag{3.5}$$

Using this result, the first and second rows can be solved in terms of σ_{11} and σ_{22} as

$$\varepsilon_{11} = \frac{(1-\nu^2)\,\sigma_{11} - \nu(1+\nu)\,\sigma_{22}}{E}, \text{ and} \tag{3.6}$$

$$\varepsilon_{22} = \frac{-\nu(1+\nu)\,\sigma_{11} + (1-\nu^2)\,\sigma_{22}}{E}. \tag{3.7}$$

As ν approaches 0.5, Eqs. (3.6) and (3.7) become

$$\varepsilon_{11} = \frac{0.75\,\sigma_{11} - 0.75\,\sigma_{22}}{E}, \text{ and} \tag{3.8}$$

$$\varepsilon_{22} = \frac{-0.75\,\sigma_{11} + 0.75\,\sigma_{22}}{E}. \tag{3.9}$$

This would suggest that for normal stresses of equal magnitude in the 1 and 2 directions, the strain will be zero in both directions. Similar results exist for Eq. (3.4) when a Poisson's ratio of 1.0 is used. Because the model is loaded mainly by pressures from the airway, which cause roughly equal normal stresses in both directions on the vocal fold surface, the strains become very small. On the other hand, if a lower value such as 0.49 is used for Poisson's ratio, Eqs. (3.6) and (3.7) become

$$\varepsilon_{11} = \frac{0.7599\,\sigma_{11} - 0.7301\,\sigma_{22}}{E}, \text{ and} \tag{3.10}$$

$$\varepsilon_{22} = \frac{-0.7301\,\sigma_{11} + 0.7599\,\sigma_{22}}{E}. \tag{3.11}$$

Under these conditions even equal normal stresses in the 1 and 2 directions will lead to deformation in both the 1 and 2 directions. In the dynamic model of the vocal folds, if there is little or no deformation, such as when $\nu = 0.5$, the model cannot vibrate. With slightly lower ν,

and therefore larger deformation the model is able to persistently vibrate. A different method of applying the plane strain assumption, such as using a transversely isotropic material with very high longitudinal Young's modulus, could potentially incorporate a Poisson's ratio corresponding to an incompressible material without limiting the model motion.

The frequency at which that the model vibrated was also greatly affected by Poisson's ratio (see Table 3.2). For the cases with ν less than 0.499, the relationship between the fundamental frequency (F_0) and ν was fairly linear with $F_0 = 275.9$ Hz for case $P_{0.4}$ and $F_0 = 225.5$ Hz for case $P_{0.495}$. However; the cases with ν of 0.499 and 0.4995 did not fit this trend. Both had a F_0 of about one third of the other cases (approximately 83 Hz). This was in part due to the period doubling. However, even taking this into consideration, the vibratory frequency of the model rapidly diminished for ν greater than 0.495. Case $P_{0.49999}$ was consistent with this observation, with $F_0 = 0$.

The variation in model motion was further evidenced by position plots of points *RI* an *RS* over one cycle (Fig. 3.16). The motion of these points was drastically altered by modifications to ν. In all cases the range of motion was reduced with increased ν and the average position was moved closer to the symmetry line. In addition, the cases where the vocal fold made contact with the contact line (cases $P_{0.4}$-$P_{0.495}$), the motion of these points was generally normal to the vocal fold surface, while the cases in which no contact was made (cases $P_{0.499}$ and $P_{0.4995}$) predicted general motion which was more tangent to the vocal fold surface.

The open quotient of each case exhibited interesting characteristics (see Table 3.2). As ν increased from 0.4 to 0.48, O_q decreased in a nearly linear manner from 0.828 to 0.660. Beyond this value of ν, the O_q increased in a somewhat linear manner to 1.0 for $\nu \geq 0.495$. The changes in O_q for the various values of ν were due to the different model vibration patterns. All of the O_q
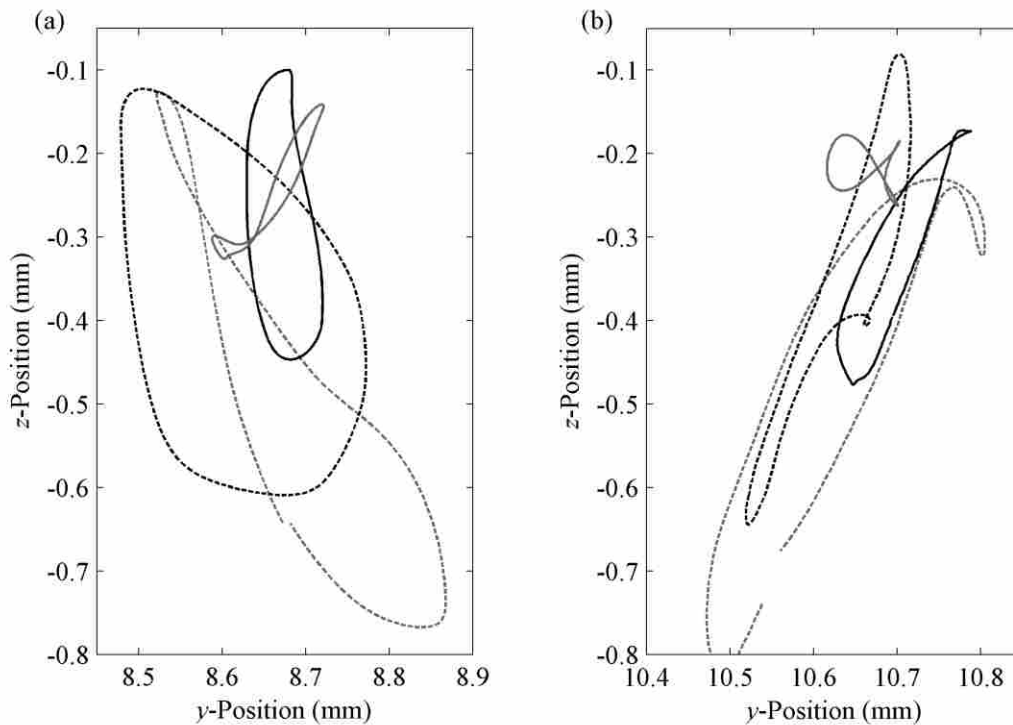
Figure 3.16: Motion of points *RI* (a) and *RS* (b) of cases $P_{0.4}$ (--), $P_{0.46}$ (---), $P_{0.495}$ (—), and $P_{0.4995}$ (—).

values observed were in the ranges of 0.51 to 1.0 given for human phonation for speakers with a fundamental frequency of 225 Hz (Baken and Orlikoff, 2000).

The wave velocity of the model was also significantly altered with changing ν. Figure 3.17 shows the V_W of the various cases vs. Poisson's ratio. For ν between 0.4 and 0.485 there was a gradual linear decrease in V_W from 1.053 to 0.894 m/s. For ν greater than 0.485 the V_W rapidly decreased to zero. It was interesting to note that this vocal fold model produced a significant mucosal wave that propagated in the range of 0.5 to 2.0 m/s, which was observed experimentally by Titze et al. (1993) for excised canine larynges, but only for Poisson's ratios $\leq$ 0.495. For these Poisson's ratios, the general motion of the model was consistent with the observed motion in human vocal folds (Doellinger and Berry, 2006; Boessenecker et al., 2007).

79
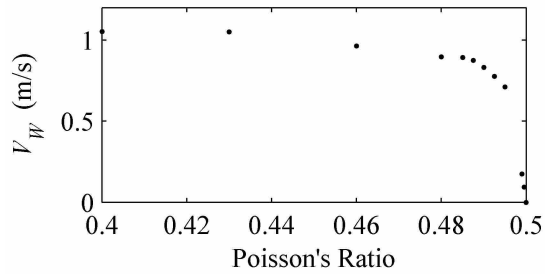
Figure 3.17: Wave velocity for various Poisson's ratios.
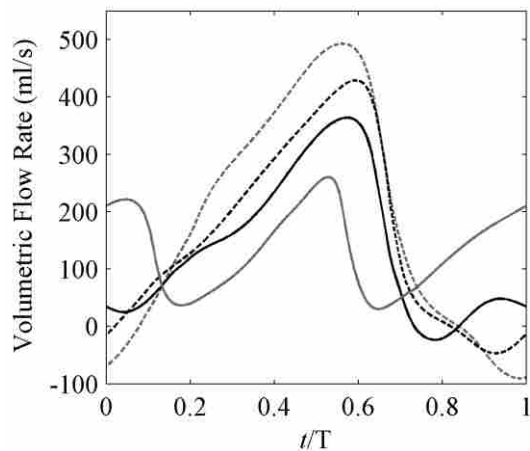
Figure 3.18: Volumetric flow rate over normalized time for several Poisson's ratio cases ($\cdots$ = P$_{0.4}$, $---$ = P$_{0.46}$, — = P$_{0.49}$, — = P$_{0.4995}$).

The flow rate waveform followed similar trends to that of glottal width (see Fig. 3.18). There was a clear decrease in amplitude with increased ν. This was a direct result of the decreased glottal area discussed above. The same period doubling was seen in cases P$_{0.499}$ and P$_{0.4995}$, with case P$_{0.49999}$ producing a constant flow rate due to the lack of vibration.

Poisson's ratio affected the glottal jet as can be seen in Fig. 3.19. The jet was much wider and varied throughout the cycle in models with lower Poisson's ratio. As Poisson's ratio increased, the glottal jet became more uniform along its length and decreased in width. This was due to the more vigorous motion exhibited by the solid when a lower Poisson's ratio was used.

80
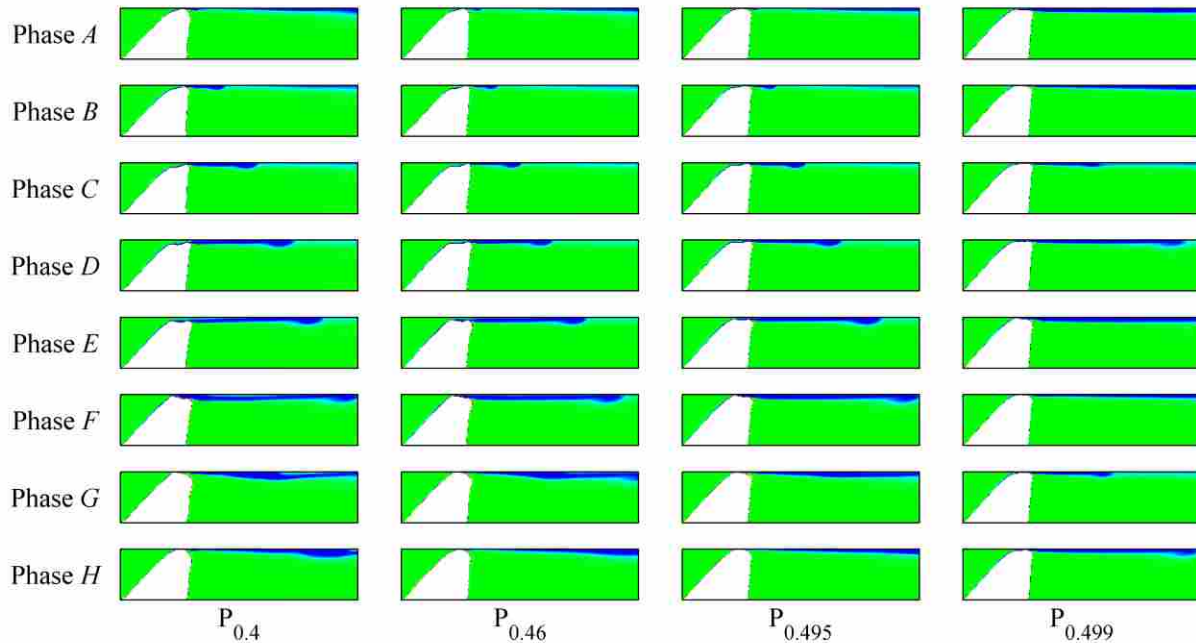
Figure 3.19: Vorticity plots showing the glottal jet at each of eight phases of one cycle for various Poisson's ratios used.

The trend continued for cases $P_{0.499}$ and $P_{0.4995}$; however, two glottal jets were formed during a single cycle due to the two near-closures of the glottis over a given cycle.

Without further investigation it is difficult to recommend a specific Poisson's ratio to use when modeling the vocal folds. It is clear that Poisson's ratios above $P_{0.495}$ are not useful for the given model and boundary conditions. Different treatment of the plane strain assumption could allow for use of Poisson's ratios closer to the incompressible theoretical. However, it is likely that the best way to treat the condition is to model the vocal fold in three dimensions using a transversely isotropic material. For two-dimensional simulations, a Poisson's ratio in the range of 0.43 to 0.495 resulted in motion and flow characteristics that were similar to those of human vocal folds.

81

3.3.4   Symmetry Condition

The assumption of symmetry was easily implemented and greatly reduced computational cost compared to that of a full model; however, the asymmetric nature of the glottal jet was not able to be represented in the simplified model. The jet asymmetry present in the full model had several notable effects on the model.

While modeling the full geometry led to some small variations in the glottal width waveforms over time, they were largely unaffected (Fig. 3.20). By investigating a single cycle of the glottal width waveform over normalized time (Fig. 3.21), some of the small differences between cases C_{50} (half model with symmetry boundary condition) and S (full model) were seen. One difference between the models was a slightly more rounded peak in glottal width in the full model than in the half model. This was due in part to the very slight out of phase motion of the left and right vocal folds in the full model. Because one fold lagged behind the other, the transition from a convergent to a divergent glottis was not as instantaneous as it was in the half model, leading to less defined peak. In addition, the waveform in Fig. 3.21 was ensemble
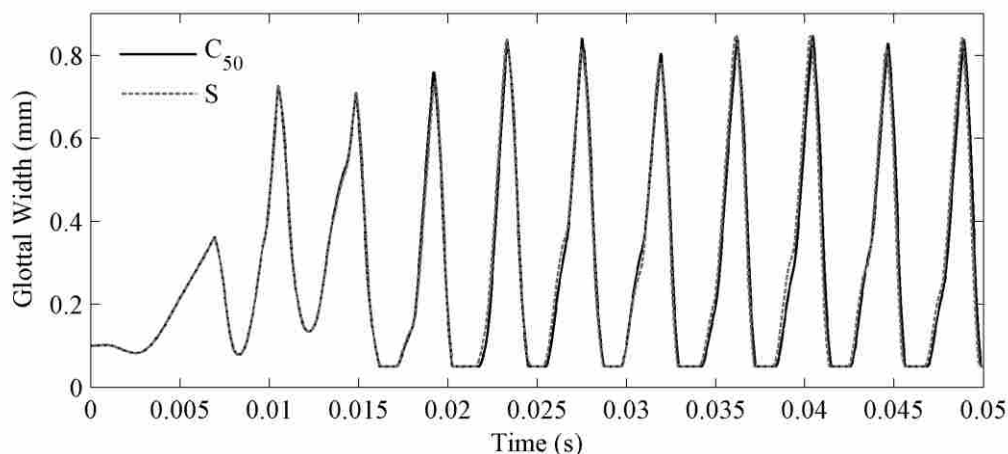
Figure 3.20: Glottal width over time for a full model (S) and a model with assumed symmetry (C_{50}).
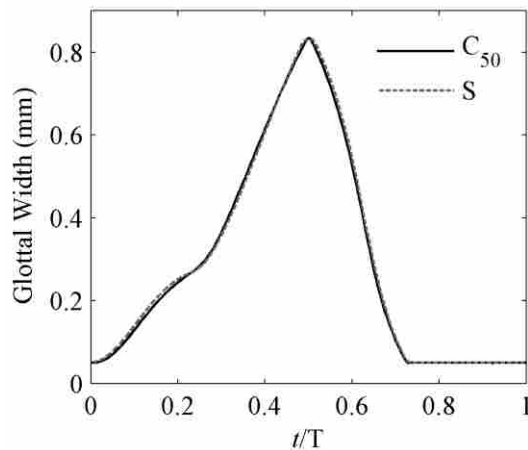
Figure 3.21: Glottal width vs. normalized time for a full model and a model with assumed symmetry.

averaged over ten cycles. This tended to further blunt the peak of the glottal width data in case S as the peak was at slightly different times from one cycle to the next. Another difference in the glottal width waveforms was seen at t/T of approximately 0.2. While the waveform was mainly linear from opening to the time of G_{max}, there was a small non-linear portion at this point in the cycle. In the full model this nonlinearity was more pronounced than it was in the half model. This was again attributed to the small phase shift between the two folds' motions in the full model.

   With these small differences in the two models, other output parameters used to describe the glottal width were negligibly affected. The fundamental frequency was increased by 0.8 Hz (0.35%) when using a full model compared to the half model. In addition, G_{max} and G_{avg} were increased by only 0.001 mm (0.12%) and 0.004 mm (1.32%), respectively. The largest effect was seen in O_q, where using a full model increased O_q by 0.024 (3.20%), but this is still relatively minor. The V_W was also increased by 0.019 m/s (2.27%). Values for these metrics can be found in Table 3.2.

Other slight variations in vocal fold motion between the two cases could be seen in the vocal fold profiles (Fig. 3.22). While the contact point for the two models was in the same location, the vocal folds in the case S were slightly further downstream than in case C_{50}. This downstream displacement was also seen in the motion of points *RI* and *RS* (see Fig. 3.23). There
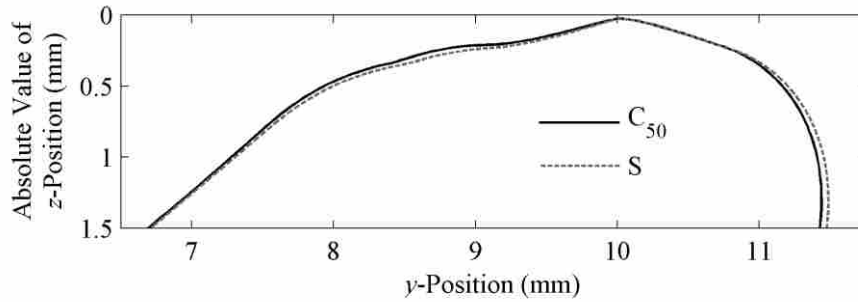
Figure 3.22: Vocal fold profiles at phase *A* for a full model (S) and a model with assumed symmetry (C_{50}).
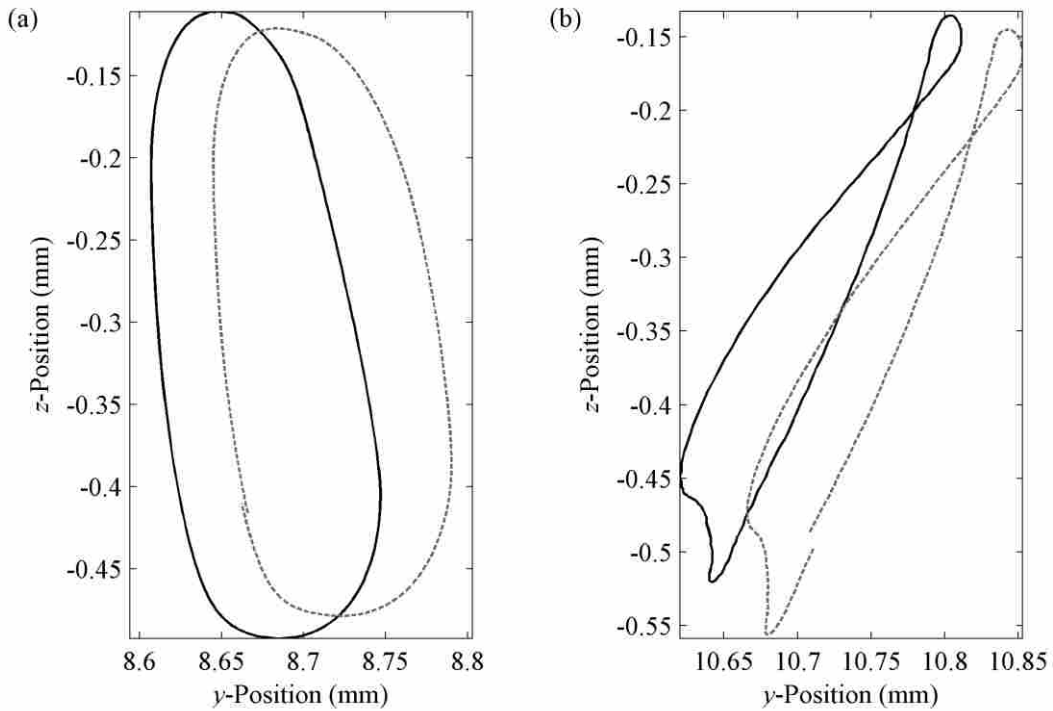
Figure 3.23: Motion of points *RI* (a) and *RS* (b) of cases S (--) and C_{50} (—).
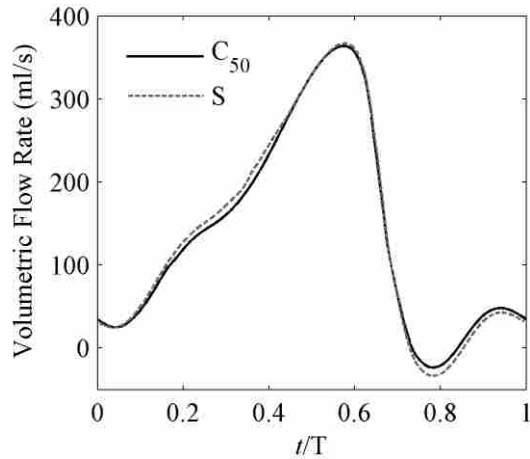
Figure 3.24: Volumetric flow rate vs. normalized time for a full model and a model with assumed symmetry.

was a clear offset in the two paths of these points of approximately 0.05 mm in the y-direction for the full model. In addition, the motion of the points in the full model was slightly smaller in amplitude for the inferior point and larger for the superior point.

The slight variations in vocal fold motion between cases C_{50} and S caused similar variations in volumetric flow rate (see Fig. 3.24). The flow rate was slightly higher (by about 5 ml/s), for the full model from the time that the glottis opened until the time of maximum glottal width. It was then lower by about the same amount during the closed portion of the cycle. These changes were reflected in increases in Q_{max} and Q_{avg} of 3.98 ml/s (1.06%) and 1.37 ml/s (1.00%), respectively.

Figure 3.25 shows the pressure profiles on the vocal fold surfaces for several phases of cases C_{50} and S. To more easily compare the two cases, the pressures in case S were averaged over 10 cycles and also over left and right vocal folds. The pressure at the location of minimum glottal width for the full model was lower by about 30 Pa during several phases of the cycle (*B*, *D*, *E*, and *H*). The opposite effect was seen in phases *A* and *F*, where the pressures were higher by about 80 Pa. Phase *G* had nearly the same pressure for both cases. The biggest difference in pressures was seen in phase *C*, where the pressure at the constriction was lower by about 125 Pa
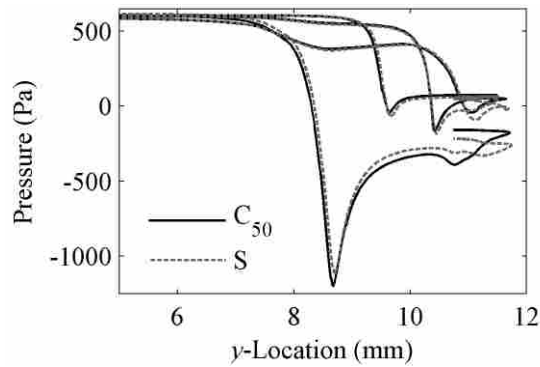
Figure 3.25: Pressure profiles for phases B, D, F, and H of a full model and a model with assumed symmetry.

in the full model. The recovery pressure was lower in case S for every phase by about 15 to 60 Pa depending on the phase.

Figure 3.26 shows vorticity plots of cases C_{50} and S for each phase of one cycle. The jet in the half model was forced to be symmetric. It therefore exited the glottis and remained straight until it exited the airway. The jet in this case slightly dissipated and spread out as it traveled downstream. On the other hand, the jet in the full model was allowed to become asymmetric. As the glottis first opened the jet exited and remained attached to the right vocal fold surface during the first two open phases (B and C). It then detached from the vocal fold surface and exited the glottis in a nearly straight path (phase D), but a large recirculation region caused it to deflect towards one wall of the supraglottal airway. It remained in this configuration until the glottis again closed at phase G. The jet was rapidly dissipated as it mixed in the recirculation region and could not be clearly seen beyond approximately one vocal fold height downstream of the glottis. Despite the significant differences between the two glottal jets, there was similarity between the models. In both models a very minimal glottal jet was present during the closed portion of the cycle (due to flow leakage) that then began to become more established at phase B. In both cases the jet continued to grow in length from phases B to F and then effectively stopped at phase G when the glottis closed.

86
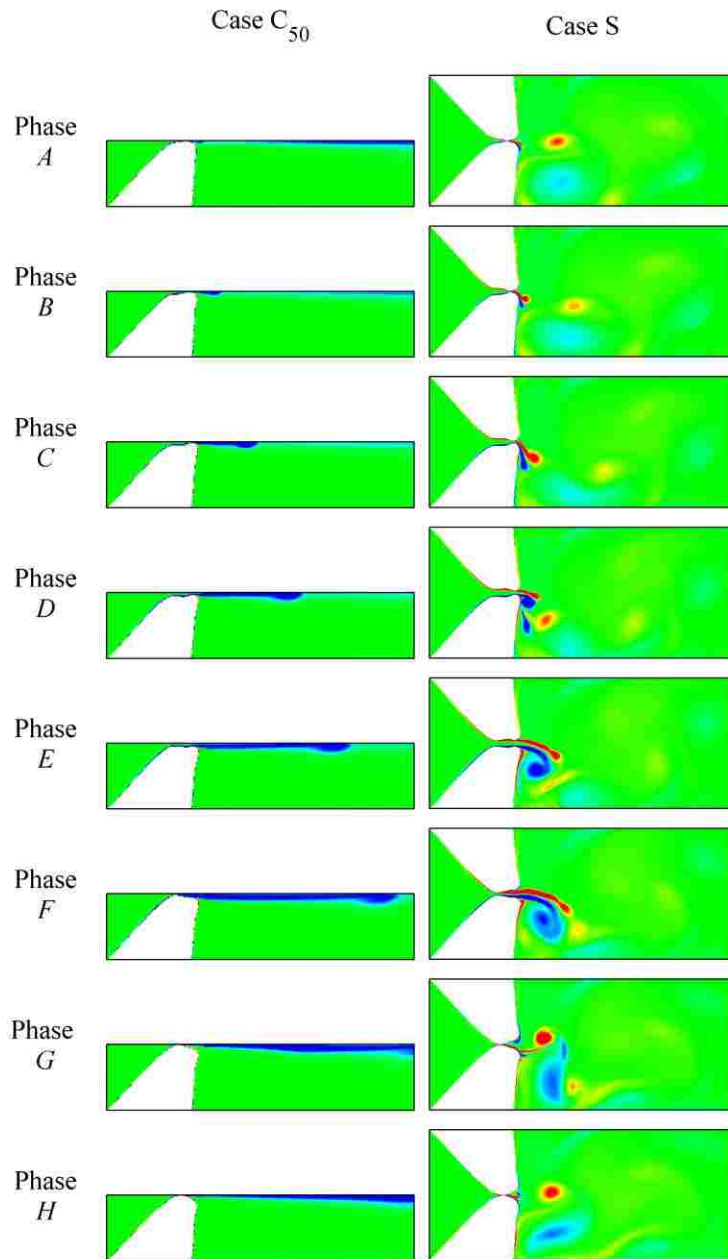
Figure 3.26: Vorticity plots for a full model (S) and a model with assumed symmetry (C_{50}).

To summarize, despite the obvious differences in the downstream asymmetry of the glottal jet, there was little effect on the rest of the model. The F_0, G_{max}, G_{avg}, O_q, V_W, Q_{max}, and Q_{avg} all increased by less than 3.4% when a full model was used. There were also small

differences in the vocal fold motion with decreased motion in *RI* and increased motion in *RS*. In addition, the vocal fold moved approximately 0.05 mm further in the *y*-direction when a full model was used. However, the general motion of the vocal fold remained the same. The pressure profiles throughout the glottis were also altered when a full model was used. The largest variation in these profiles was approximately 125 Pa at the contact location during phase *C*. Most of the pressure profiles had smaller differences of around only 20 Pa. The largest apparent effect of these differences in pressure was in the lower recovery pressure of the full model, leading to the larger downstream displacement of the vocal folds.

It is concluded that for research focusing on vocal fold motion or flow within or upstream of the glottis, for cases with symmetric geometry and material properties, a half model may be adequate. A full model is necessary if details of the asymmetries present in the glottal jet or the asymmetries of pressures within the glottis are desired. One area in which this might also be important is the study of potential asymmetry in energy transfer to the two vocal folds. Finally, acoustic sound production is highly related to the jet dynamics, and is therefore sensitive to flow rate waveforms and other jet characteristics. Thus a full model would be better than a half model for predicting radiated sound.

3.4 Conclusions

Many different assumptions have been made in defining computational vocal fold models. These assumptions have the potential to alter the usefulness and validity of the simulations; however, the exact effects of these assumptions have not previously be explored. In this chapter, the effects of various modeling choices were explored using a two-dimensional four-layer vocal fold model.

The contact line location was systematically explored and found to affect some aspects of the simulation results. The closer the vocal fold was able to approach the center line, the more completely the glottis closed and flow leakage was reduced. There was however, a negative side effect. The pressures in cases with a minimum glottal gap (G_{min}) less than 20 μm began to exhibit spurious pressure fluctuations in the vicinity of contact. The amplitude of these fluctuations increased with decreasing G_{min} and was approximately 700 Pa at the location of contact in case C_1. These spurious pressures seemed to arise from numerical instabilities when the mesh compressed beyond a certain point; however, they did not seem to significantly affect the remaining pressure fields or vocal fold motion for cases other than C_1.

Very little change was seen in the vocal fold motion, glottal widths, or flow rates with changing G_{min}. For example, G_{max}, F_0, V_W, and Q_{max} each varied by less than 1% while G_{avg} and Q_{avg} both varied by less than 7% over the range of G_{min} values studied.

Based on these results, a G_{min} of 50 μm should be sufficient to obtain results that are reasonably representative of what would be expected with a model that completely closes. However, for greater accuracy or more realistic pressures along the vocal fold surfaces, a G_{min} of 10 μm may be preferred. The choice must be made with consideration of the trade-offs between minimum desired glottal width, minimum desired flow rate, and mesh movement (which is typically easier with larger G_{min}). In this study the effect on solid model stresses during contact was not considered, and this should be studied in the future.

Varying the Poisson's ratio had a significant effect on this model's response. As Poisson's ratio was increased, the amplitude of vibration decreased from $G_{max} = 1.151$ mm in case $P_{0.4}$ to $G_{max} = 0.46$ in case $P_{0.4995}$. Vibration stopped altogether in case $P_{0.49999}$. The lack of vibration was attributed to the plain strain assumption combined with $\nu \approx 0.5$. Under these conditions, equal

normal stresses in the 1 and 2 directions led to the strain in these directions being zero. In addition, the specific motion of the given model was significantly affected by the choice of Poisson's ratio. The variation in vocal fold motion also led to variations in flow rates, frequencies, and glottal jet characteristics. Q_{max} ranged from 126.2 to 363.6 ml/s, while F_0 varied from 0.0 to 275.9 Hz. When choosing Poisson's ratio, the researcher must use a value that results in vocal fold motion that is similar to observed motion in actual larynges, which in this study, was found to be in the range of 0.43 to 0.495.

Some variations in model output were seen when comparing the response of a full model (i.e., including both vocal folds) with a half model (only one vocal fold and assumed symmetry). The largest variation was in the glottal jet response. In the half model the jet was symmetric by definition and dissipated very little as it traveled through the supraglottal region. In the full model the jet was diverted toward one supraglottal wall and rapidly dissipated in the recirculation region. The lower supraglottal pressures (around 40 Pa lower) caused by the recirculation regions in the full model led to larger downstream displacement of the vocal folds by about 0.05 mm. Despite the larger mean displacement, the medial surface of the vocal folds in the region of contact was nearly identical in the two cases. In the full model, F_0, G_{max}, G_{avg}, O_q, V_W, Q_{max}, and Q_{avg} each increased by less than 3.4% from the half model values. The half model was deemed sufficient for simulations where the vocal folds are symmetric and the asymmetries of vocal fold pressures or of the glottal jet are not of particular interest. Because of the sensitivity of the radiated sound field to fine scale flow structures, a symmetric flow model may not be appropriate for acoustic predictions. Future work should explore this issue, however.

4 CONCLUSIONS AND FUTURE WORK

Computational models of the flow-induced vibrations of the vocal folds are powerful tools that can be used in conjunction with physical experiments to better understand voice production. An improved understanding of the physics of voice production will lead to better diagnosis and treatment of patients with voice pathologies. This thesis research has been performed to contribute to this understanding. In particular, the effects of supraglottal geometry have been analyzed using a computational model of the vocal folds and laryngeal airway. In addition, three important computational modeling parameters (contact line location, Poisson's ratio, and symmetry assumptions) were systematically varied to determine the influence of their values on model response.

4.1 Effect of Supraglottal Geometry on the Flow-Induced Response of a Computational Vocal Fold Model (Chapter 2)

4.1.1 Conclusions

Several supraglottal configurations were positioned superior to a pair of symmetric, four-layer, finite element vocal fold models. Air flowing through the fluid domain interacted with the vocal folds to create sustained vibrations in the vocal folds. The vocal folds exhibited a pronounced mucosal wave that has not been seen in many previous simulations and synthetic model experiments, but that is representative of the motion of the human vocal folds during vibration.

Without false vocal folds (FVFs), the glottal jet was diverted towards one side of the supraglottal duct, generally towards the nearest wall when the supraglottal geometry was asymmetrically positioned. When FVFs were included, the jet diverted towards one of the FVF surfaces; however, the deflection was smaller in magnitude than when no FVFs were present. The jet deflection was fairly consistent from one cycle to the next when no FVFs were present or when the FVF geometry was asymmetrically placed. When the FVF geometry was symmetrically placed, the jet direction periodically alternated and at some times was not deflected at all.

The asymmetric glottal jet led to asymmetric pressure profiles within the glottis. These asymmetries were more pronounced with larger jet deflection. In addition, the pressure profiles exhibited cycle-to-cycle variations when the jet was inconsistently deflected. In spite of these asymmetries, the motion of the vocal folds themselves was nearly symmetric, exhibiting only small degrees of asymmetry that were more prevalent when cyclically-inconsistent pressure profiles were present. The asymmetric pressure profiles observed in cases in which the jet consistently deflected in the same direction did not lead to asymmetric motion. In general, the relative insignificance of the degree of asymmetry exhibited by the vocal fold models in this study suggests that characteristics (such as asymmetry) of the supraglottal jet alone may not be sufficient to significantly alter vocal fold motion.

4.1.2 Future Work

Several areas of future work related to this research are suggested. First, and perhaps most importantly, because of the inherent three-dimensional nature of the glottis and glottal jet, a study that incorporates three-dimensional vocal folds and airway, and that also uses a vocal fold model that exhibits a pronounced mucosal wave, is necessary. Because a two-dimensional model

does not include energy dissipation in the third dimension, the effects of the glottal jet may be artificially amplified in a two-dimensional simulation. Second, it is possible that the low driving pressure of this model contributed to the consistent jet deflection. Therefore, the effect of higher driving pressures should be studied to determine their effect on cycle-to-cycle variations in this model. Third, using a turbulent model for the airway could lead to different effects on the glottal jet motion, and as a result, on the vocal fold motion and pressure profiles. Fourth, the stresses arising in the vocal folds in relation to the asymmetry in the pressure profiles should be studied in depth. Finally, in this study, due to computational cost, coarse movement of the supraglottal geometry was used. Additional insight could perhaps be gained by using a vocal fold model with prescribed motion, thereby reducing computational cost and allowing for finer variations in the supraglottal geometry size and position.

4.2 Effect of Modeling Choices on the Flow-Induced Response of a Computational Vocal Fold Model (Chapter 3)

4.2.1 Conclusions

A two-dimensional computational model of the vocal folds was used to analyze the effects of several modeling choices on vocal fold motion and fluid flow characteristics. First, the position of the contact line was systematically varied. Second, different Poisson's ratio values of the solid model materials were studied. Third, a full model containing two vocal folds was compared to a half model in which only one vocal fold was included and a symmetry boundary condition was enforced.

There exists a trade-off between modeling full glottal closure and running simulations using a setup that will allow for robust mesh movement. While the fluid mesh motion was more well-behaved for larger minimum glottal widths (G_{min}), more air "leaked" through the glottis. To

determine how contact line location altered this balance, G_{min} was systematically varied from 1 to 50 μm by altering the location of the contact line. As G_{min} approached zero, the values of important parameters were relatively unaffected by contact line location. The resulting flow rate, glottal width, frequency, wave velocity, and open quotients had a maximum variation of less than 7%. Pressure profiles along the vocal fold surface were not significantly altered during the open phase, except for the case in which G_{min} was 1 μm. During the closed phase, the pressures for cases with G_{min} less than 20 μm exhibited spurious pressure fluctuations which became more severe with smaller values of G_{min}. It is suggested that for studies in which pressure profiles or minimum glottal flow are not of particular interest, a G_{min} of 50 μm may be sufficient. If increased accuracy is desired, G_{min} can be lowered to 10 μm without introducing significant pressure fluctuations.

While vocal fold tissue is typically assumed to be incompressible, most computational models have been defined using a Poisson's ratio (ν) lower than the incompressible limit. There have been a wide variety of Poisson's ratios used, yet no previous systematic evaluation of its effect on a vocal fold model has previously been performed. In this thesis research the Poisson's ratio in the solid model was varied from 0.4 to 0.49999, where 0.5 corresponds to incompressibility. The model motion was strongly influenced by variations in ν, with larger amplitudes resulting with lower ν values. For $\nu > 0.495$, the vocal folds did not close completely, and for $\nu = 0.49999$ the model did not vibrate. It was shown that for the assumptions of plane strain with an isotropic material, equal normal stresses in the plane will lead to zero normal strain when $\nu = 0.5$. In addition, it was found that with these same assumptions, the model motion approximated that of human vocal folds for ν between 0.43 and 0.495.

For computational efficiency, often only one half of the larynx is modeled and a symmetry boundary condition is used. However, asymmetry in the glottal jet has been observed, both in this thesis research and in previous studies, in models (real and computational) with both vocal folds. In this study, the results of a full model, consisting of two vocal folds, and a half model, consisting of one vocal fold and a symmetry boundary condition, were compared. The profiles of the medial surfaces of the vocal folds of both models were nearly indistinguishable in the vicinity of contact with the contact line. However, the mean displacement of the folds in the full model was approximately 0.05 mm further downstream as evidenced by the profiles of the superior portion of the vocal folds. In the full model, the frequency, glottal width, flow rate and wave velocity all increased by less than 3.4% when compared to the half model. The largest variation between the models was in the glottal jet characteristics. The full model predicted a large deflection and rapid dissipation of the jet that were not seen in the half model. It was determined that for studies not dependent on glottal jet characteristics (such as acoustic sound production), or for studies that do not include inherent asymmetry in geometry or material properties, the half model is sufficient.

4.2.2 Future Work

Several additional areas of future research are advised. One possibility is to attempt to eliminate the spurious pressures which were seen for small G_{min}. This could perhaps be accomplished by increasing the control volume density along the length of glottis. This would improve the aspect ratio of the control volumes when highly compressed. Additional insights about the effects of contact line location could be gained through a study analyzing the stresses within the vocal fold. Another area of future research would be to systematically determine the relative magnitude of longitudinal Young's modulus that would be needed in a three-

95

dimensional, transversely isotropic model to cause planar motion without the need of the plane strain assumption. The effect of Poisson's ratio could also be studied on different model types to determine if similar effects to those observed in this model are seen in other models. The effect of the symmetry assumption on radiated acoustic sound could also be studied.

REFERENCES

Alipour, F., Berry, D. A., and Titze, I. R. (**2000**). "A finite-element model of vocal-fold vibration," J. Acoust. Soc. Am. **108**, 3003-3012.

Alipour, F. and Scherer, R. C. (**2004**). "Flow separation in a computational oscillating vocal fold model," J. Acoust. Soc. Am. **116**, 1710-1719.

Alipour, F. and Scherer, R. C. (**2000**). "Vocal fold bulging effects on phonation using a biophysical computer model," Journal of Voice **14**, 470.

Baken, R. J., and Orlikoff, R. F. (**2000**). *Clinical Measurement of Speech and Voice*, second edition, Singular Publishing Group, San Diego CA, **pp. 361-368, 408-411**.

Becker, S., Kniesburges, S., Müller, S., Delgado, A., Link, G., Kaltenbacher, M., and Döllinger, M. (**2009**). "Flow-structure-acoustic interaction in a human voice model," J. Acoust. Soc. Am. **125**, 1351-1361.

Berry, D. A. and Titze, I. R. (**1996**). "Normal modes in a continuum model of vocal fold tissues," J. Acoust. Soc. Am. **100**, 3345-3354.

Bertram, C. D. (**2009**). "A numerical investigation of waves propagating in the spinal cord and subarachnoid space in the presence of a syrinx," J. Fluids Struct. **25**, 1189.

Boessenecker, A., Berry, D. A., Lohscheller, J., Eysholdt, U., and Doellinger, M. (**2007**). "Mucosal wave properties of a human vocal fold," Acta Acustica United with Acustica **93**, 815-823.

Cook, D. D. and Mongeau, L. (**2007**). "Sensitivity of a continuum vocal fold model to geometric parameters, constraints, and boundary conditions," J. Acoust. Soc. Am. **121**, 2247-2253.

Cook, D. D., Nauman, E., and Mongeau, L. (**2008**). "Reducing the number of vocal fold mechanical tissue properties: Evaluation of the incompressibility and planar displacement assumptions," J. Acoust. Soc. Am. **124**, 3888-3896.

Decker, G. Z. and Thomson, S. L. (**2007**). "Computational simulations of vocal fold vibration: Bernoulli versus Navier-Stokes," Journal of Voice **21**, 273.

Doellinger, M. and Berry, D. A. (**2006**). "Visualization and quantification of the medial surface dynamics of an excised human vocal fold during phonation," Journal of Voice **20**, 401.

Drechsel, J. S. and Thomson, S. L. (**2008**). "Influence of supraglottal structures on the glottal jet exiting a two-layer synthetic, self-oscillating vocal fold model," J. Acoust. Soc. Am. **123**, 4434-4445.

Erath, B. and Plesniak, M. (**2010**). "An investigation of asymmetric flow features in a scaled-up driven model of the human vocal folds," Exp. Fluids **49**, 131-146.

Erath, B. and Plesniak, M. (**2006a**). "An investigation of bimodal jet trajectory in flow through scaled models of the human vocal tract," Exp. Fluids **40**, 683-696.

Erath, B. and Plesniak, M. (**2006b**). "An investigation of jet trajectory in flow through scaled vocal fold models with asymmetric glottal passages," Exp. Fluids **41**, 735-748.

Finnegan, E. M. and Alipour, F. (**2009**). "Phonatory effects of supraglottic structures in excised canine larynges," Journal of Voice **23**, 51.

Gunter, H. E., Howe, R. D., Zeitels, S. M., Kobler, J. B., and Hillman, R. E. (**2005**). "Measurement of vocal fold collision forces during phonation: Methods and preliminary data," J. Speech Lang. Hear. Res. **48**, 567-576.

Ishizaka, K. and Flanagan, J. L. (**1972**). "Synthesis of voiced sounds from a two-mass model of the vocal cords," Bell Syst. Tech. J. **51**, 1233-1267.

Jiang, J. J., Zhang, Y., and Stern, J. (**2001**). "Modeling of chaotic vibrations in symmetric vocal folds," **110**, 2120-2128.

Lempriere, B. M. (**1968**). "Poisson's ratio in orthotropic materials," Am. Inst. of Aero. and Astro. **6**, 2226-2227.

Luo, H., Mittal, R., and Bielamowicz, S. A. (**2009**). "Analysis of flow-structure interaction in the larynx during phonation using an immersed-boundary method," J. Acoust. Soc. Am. **126**, 816-824.

Luo, H., Mittal, R., Zheng, X., Bielamowicz, S. A., Walsh, R. J., and Hahn, J. K. (**2008**). "An immersed-boundary method for flow-structure interaction in biological systems with application to phonation," Journal of Computational Physics **227**, 9303.

National Institute on Deafness and Other Communication Disorders (NIDCD) (**2010**). http://www.nidcd.nih.gov/health/statistics/vsl/Pages/stats.aspx, Oct. 6 2011

Neubauer, J., Zhang, Z., Miraghaie, R., and Berry, D. A. (**2007**). "Coherent structures of the near field flow in a self-oscillating physical model of the vocal folds," J. Acoust. Soc. Am. **121**, 1102-1118.

Pickup, B. A. and Thomson, S. L. (**2011**). "Identification of geometric parameters influencing the flow-induced vibration of a two-layer self-oscillating computational vocal fold model," J. Acoust. Soc. Am. **129**, 2121-2132.

Rosa, M. d. O., Pereira, J. C., Grellet, M., and Alwan, A. (**2003**). "A contribution to simulating a three-dimensional larynx model using the finite element method," J. Acoust. Soc. Am. **114**, 2893-2905.

Scherer, R. C., Shinwari, D., Witt, K. J. D., Zhang, C., Kucinschi, B. R., and Afjeh, A. A. (**2001**). "Intraglottal pressure profiles for a symmetric and oblique glottis with a divergence angle of 10 degrees," J. Acoust. Soc. Am. **109**, 1616-1630.

Schuberth, S., Hoppe, U., Döllinger, M., Lohscheller, J., and Eysholdt, U. (**2002**). "High-precision measurement of the vocal fold length and vibratory amplitudes," Laryngoscope **112**, 1043-1049.

Smith, S. L. (**2011**). "Influence of subglottic geometry on computational and synthetic vocal fold model vibration," Master's Thesis, Brigham Young University, Provo, UT.

Story, B. H. and Titze, I. R. (**1995**). "Voice simulation with a body-cover model of the vocal folds," J. Acoust. Soc. Am. **97**, 1249-1260.

Suh, J. and Frankel, S. H. (**2008**). "Comparing turbulence models for flow through a rigid glottal model," J. Acoust. Soc. Am. **123**, 1237-1240.

Tao, C. and Jiang, J. J. (**2007**). "Mechanical stress during phonation in a self-oscillating finite-element vocal fold model," J. Biomech. **40**, 2191.

Tao, C. and Jiang, J. J. (**2006**). "Anterior-posterior biphonation in a finite element model of vocal fold vibration," J. Acoust. Soc. Am. **120**, 1570-1577.

Tao, C., Zhang, Y., Hottinger, D. G., and Jiang, J. J. (**2007**). "Asymmetric airflow and vibration induced by the coanda effect in a symmetric model of the vocal folds," J. Acoust. Soc. Am. **122**, 2270-2278.

Thomson, S. L., Mongeau, L., and Frankel, S. H. (**2005**). "Aerodynamic transfer of energy to the vocal folds," J. Acoust. Soc. Am. **118**, 1689-1700.

Titze, I. R. (**1974**). "The human vocal cords: A mathematical model, part II," Phonetica **29**, 1-21.

Titze, I. R. (**1973**). "The human vocal cords: A mathematical model, part I," Phonetica **28**, 129-170.

Titze, I. R. and Story, B. H. (**2002**). "Rules for controlling low-dimensional vocal fold models with muscle activation," J. Acoust. Soc. Am. **112**, 1064-1076.

Titze, I. R., Jiang, J. J., and Hsiao, T. Y. (**1993**). "Measurement of mucosal wave propagation and vertical phase difference in vocal fold vibration," Ann. Otol. Rhinol. Laryngol. **102**, 58-63.

Triep, M., Brücker, C., and Schröder, W. (**2005**). "High-speed PIV measurements of the flow downstream of a dynamic mechanical model of the human vocal folds," Exp. Fluids **39**, 232-245.

Valencia, A. and Baeza, F. (**2009**). "Numerical simulation of fluid-structure interaction in stenotic arteries considering two layer nonlinear anisotropic structural model," Int. Commun. Heat Mass Transfer **36**, 137.

Xue, Q., Mittal, R., Zheng, X., and Bielamowicz, S. (**2010**). "A computational study of the effect of vocal-fold asymmetry on phonation," J. Acoust. Soc. Am. **128**, 818-827.

Zhang, Z. (**2009**). "Characteristics of phonation onset in a two-layer vocal fold model," J. Acoust. Soc. Am. **125**, 1091-1102.

Zhao, W., Zhang, C., Frankel, S. H., and Mongeau, L. (**2002**). "Computational aeroacoustics of phonation, part I: Computational methods and sound generation mechanisms," J. Acoust. Soc. Am. **112**, 2134-2146.

Zheng, X., Mittal, R., and Bielamowicz, S. (**2011a**). "A computational study of asymmetric glottal jet deflection during phonation," J. Acoust. Soc. Am. **129**, 2133-2143.

Zheng, X., Mittal, R., Xue, Q., and Bielamowicz, S. (**2011b**). "Direct-numerical simulation of the glottal jet and vocal-fold dynamics in a three-dimensional laryngeal model," J. Acoust. Soc. Am. **130**, 404-415.

Zheng, X., Xue, Q., Mittal, R., and Beilamowicz, S. (**2010**). "A coupled sharp-interface immersed boundary-finite-element method for flow-structure interaction with application to human phonation," J. Biomech. Eng. **132**, 111003.

Zheng, X., Bielamowicz, S., Luo, H., and Mittal, R. (**2009**). "A computational study of the effect of false vocal folds on glottal flow and vocal fold vibration during phonation," Ann. Biomed. Eng. **37**, 625-642.